X-660-74-16

MEASUREMENT OF COSMIC RAY POSITRON AND NEGATRON SPECTRA BETWEEN 50 AND 800 MeV

JOSEPH K. DAUGHERTY

JANUARY 1974

GODDARD SPACE FLIGHT CENTER
GREENBELT, MARYLAND

MEASUREMENT OF COSMIC RAY POSITRON AND NEGATRON SPECTRA BETWEEN 50 AND 800 MeV*

by
Joseph Kenneth Daugherty

Dissertation submitted to the Faculty of the Graduate School
of the University of Maryland in partial fulfillment
of the requirements for the degree of
Doctor of Philosophy
1973

*Supported in part by NASA Grant NGL 21-002-033

ABSTRACT

Title of Thesis: Measurement of Cosmic Ray Positron and Negatron Spectra Between 50 and 800 MeV

Joseph K. Daugherty, Doctor of Philosophy, 1973

Thesis directed by: Frank B. McDonald

Professor of Physics

A balloon-borne magnetic spectrometer has been used to measure the spectra of cosmic ray positrons and negatrons at energies between 50 and 800 MeV. The data reported here were obtained during two flights from Fort Churchill, Manitoba, in July 1972.

The detector used for these measurements employs a permanent magnet with a field integral of 25 kilogauss-cm between two digital readout spark chambers. A scintillator telescope with a geometric factor of 19 cm^2 sr is operated in coincidence with a gas Cerenkov velocity threshold detector to generate the spark chamber trigger pulses. In addition, a sandwich of lead plates and two plastic scintillators has been placed beneath the lower spark chamber as a means of distinguishing electrons from heavier particles with velocities above the Cerenkov counter threshold.

Measurements of the individual positron and negatron intensities are of great importance in understanding the origins of cosmic ray electrons in the galaxy. In particular, the determination of the positive fraction $\frac{N_{e^+}}{N_{e^+} + N_{e^-}}$ in the total electron component provides a critical test of the hypothesis that the energetic electrons reaching the earth were produced in collisions of nucleonic cosmic rays (accelerated in

primary galactic sources) with the interstellar gas. At the same time, comparisons of the separate positron and negatron spectra observed near the earth with their expected intensities in interstellar space can be used to investigate the complex (and variable) interaction of galactic cosmic rays with the expanding solar wind.

The present measurements, which have established finite values or upper limits for the positron and negatron spectra between 50 and 800 MeV, have confirmed earlier evidence for the existence of a dominant component of negatrons from primary sources in the galaxy. The present results have further been shown to be consistent with the hypothesis that the positron component is in fact mainly attributable to collisions between cosmic ray nuclei and the interstellar gas. Finally, the estimate of the absolute intensities have confirmed the indications from neutron monitors that in 1972 the interplanetary cosmic ray intensities were already recovering toward their high levels observed in 1965 (at solar minimum).

ACKNOWLEDGEMENTS

I am deeply grateful to Dr. Carl E. Fichtel and Dr. Robert C. Hartman, who suggested this project and provided essential guidance and advice in all phases of the work. I am also greatly indebted to Dr. Frank B. McDonald for valuable advice and suggestions concerning this research and its broader scientific goals. Sincere thanks are also due to Dr. Peter Schmidt for valuable insight and prolific advice regarding many phases of this work. I have benefited greatly from discussions with Dr. L. A. Fisk, Dr. R. Ramaty and Dr. S. A. Stephens. For essential technical support during the assembly of the detector and all of its flights, I am especially grateful to Mr. David Andrews. Messrs. Stuart Allison, V. P. Cogan, W. M. Daniels, Charles Ehrmann, Harry Harbourt, Robert W. Ross, Robert L. Smith and W. Pusey Jr., have also provided essential engineering and technical assistance during various phases of the project. For their help and cooperation during calibrations at the National Bureau of Standards, I am grateful to Dr. S. Penner, Mr. A. Filipovitch, and Mr. W. Page. I thank Messrs. D. McQuinn, David Kehs, Kevin Harris and Edward M. Greville for critical programming assistance during the data analysis. For valuable assistance and generous cooperation in the preparation of the drawings, I would like to thank Messrs. Adam Thompson, Frank Schaffer and Harry Trexel. I am particularly indebted to Ms. R. Ramberg and Ms. Naomi Howe for their patience and diligence in the preparation of this manuscript. Finally, I am most grateful to my close friend and companion, Robin, whose understanding and encouragement have made this work possible.

TABLE OF CONTENTS

LIST OF TABLES

LIST OF FIGURES

CHAPTER I

INTRODUCTION

A. Historical Background

The question of the origin of energetic primary cosmic ray electrons has attracted continuing interest since radio astronomers first reported evidence for the existence of these particles within interstellar space. Early observations of the diffuse nonthermal radio emission from extensive regions of the galaxy suggested the presence of energetic electrons spiraling in the weak interstellar magnetic field (Kiepenheuer, 1950; Ginzburg, 1951). It was almost immediately recognized that these galactic electrons might be produced by physical processes quite different from the acceleration mechanisms responsible for nucleonic cosmic rays. Hayakawa (1952) first suggested that the radiating electron flux could be attributed to the continual production of positrons and negatrons in hadronic collisions between cosmic ray nuclei and the interstellar gas. At that time it seemed plausible that such a purely secondary production mechanism might explain both the characteristics of the nonthermal radio emission and the relatively low abundance of electrons in the cosmic rays reaching the vicinity of the earth.

It was also recognized that direct measurements of cosmic ray electrons could provide important tests of the secondary origin hypothesis. In particular, Ginzburg (1958) and Hayakawa et al. (1958) pointed out that the relative abundances of positrons and negatrons in the total

electron component would provide strong evidence concerning the importance of secondary production, since the significant fraction of positrons in the secondary source spectrum could be predicted with some confidence to energies exceeding 10 GeV. The positron intensities should in fact dominate the (secondary) negatron intensities over a wide energy range which should be reflected in the observed spectrum at energies greater than about 50 MeV. While below this region a negatron excess should result from electromagnetic collisions of cosmic rays with atomic electrons in the interstellar gas (Abraham, Brunstein, and Cline, 1966), a dominant negatron flux at greater energies would provide convincing evidence for the existence of primary electron sources in the galaxy.

Unfortunately, direct measurements of cosmic ray electrons were not immediately available. By the early fifties, balloon-borne instruments (Hulsizer and Rossi, 1948; Critchfield et al., 1952) had only been able to set upper limits on the total electron intensity beyond the atmosphere. The maximum balloon altitudes then attainable and the available instrumental techniques effectively precluded observations of primary electrons above the dominant backgrounds of cosmic ray nuclei (mainly protons) and atmospheric secondary electrons resulting from interactions between cosmic ray nuclei and air atoms. These difficulties were soon apparent, since the upper limits obtained by Critchfield et al. (1952) demonstrated that electrons comprised less than one per cent of all primary cosmic rays reaching the earth.

The earliest balloon observations of finite cosmic ray electron intensities were obtained by Earl (1961) and by Meyer and Vogt (1961). In the following years, continuing improvements in experimental techniques have enabled many investigators to observe the total electron

spectrum over a range extending up to several hundred GeV (see for example Meyer, 1971). However, most of these accumulated measurements, and of course all the radio observations, have employed techniques which cannot distinguish positrons from negatrons in the total electron flux. Such observations can be compared only with the theoretically predicted shape of the total electron spectrum from secondary (or primary) galactic sources. Unfortunately, comparisons with the total electron spectrum are difficult because of uncertainties in several physical parameters which enter into the calculations of galactic electron production and equilibrium spectra. (The dependence of the galactic secondary electron intensities on the properties of hadronic collisions at high energies as well as the precise conditions in interstellar space will be discussed at length in Chapters II and III.) These difficulties can be largely overcome by resolving individually the negatron and positron spectra.

During the past decade, however, only a small number of balloon-borne magnetic spectrometers have been used to distinguish positrons from negatrons in the cosmic ray electron spectrum at energies ranging from about 10 MeV to 10 GeV. The earliest series of measurements (De Shong et al., 1964; Hartman et al., 1965; Hartman, 1967; Fanselow et al., 1969) employed a detector in which optical spark chambers with thin aluminum plates traced the deflections of charged particles traversing the gap region of a permanent magnet. A lower spark chamber with tantalum plates provided a total of 4.5 radiation lengths of material in which the development of characteristic electron-initiated showers could be observed. Later spectrometers (Fichtel et al., 1968; Kniffen et al., 1970; Beuermann et al., 1969, 1970) employed wire-grid spark chambers

with ferrite core or magnetostrictive readout systems to reduce the average scattering of electrons above and below the magnet gap region. In most of the detectors of this type a gas Cerenkov counter was operated in coincidence with a scintillator array to generate the spark chamber trigger pulses. The Cerenkov counter served the dual purpose of preventing triggers by the large flux of cosmic ray protons below 10-30 GeV and imposing a directional requirement on incident particles.

Several investigators have pursued an alternative technique, based on the difference in the geomagnetic threshold rigidities of positrons and negatrons in the east-west directions at balloon altitudes. In these experiments, the directions of electron-initiated cascades in spark chambers or emulsion stacks have been examined in attempts to infer the electron charge ratio up to about 40 GeV (Agrinier et al., 1965; Bland et al., 1966; Daniel and Stephens, 1966; Stephens, 1969). However, the accuracy of this method is severely limited by the small number of identifiable primary electron events in each experiment.

A summary of results from several of these balloon measurements of the positive fraction of primary cosmic ray electrons has been presented in Figure 1.1. At present the only available satellite observations of positron intensities (Cline and Hones, 1968) have been restricted to energies near 1 MeV.

Figure 1.1 indicates that an apparent negatron excess does exist above a few hundred MeV in the cosmic ray electron flux reaching the earth. However, the statistical accuracy of these results is limited by the fact that all balloon measurements below about 1 GeV involve significant corrections for the background of residual atmospheric secondary

electrons at float altitudes, as well as a possible contamination by primary cosmic ray protons or heavier nuclei. The atmospheric background even at residual depths of 2 g cm^{-2} is sufficiently intense that below several hundred MeV the possibility of measuring the primary flux of positrons is considerable decreased, especially during periods of significant cosmic ray modulation by the solar wind. As a result there has been some question about the validity of the results summarized in Figure 1.1 (Beedle et al., 1970). The controversy actually stems from discrepancies between several measurements of the total electron flux, which may in principle be distinguished from measurements of the charge ratio. Nevertheless, the questions posed about the earlier results have prompted further attempts to measure the separate positron and negatron spectra below 1 GeV as well as at higher energies extending to about 50 GeV (Buffington et al., 1973).

B. The Experiment

The recent balloon measurements whose results are presented here provide additional data on the cosmic ray positron and negatron spectra between 50 MeV and 800 MeV. The detector used for these measurements was designed and assembled at the laboratory for High Energy Astrophysics, NASA/Goddard Space Flight Center. The instrument was successfully launched twice from Fort Churchill, Manitoba, Canada, in July, 1972 during periods in which neutron monitors were recording cosmic ray levels normally observed near solar minimum (see Figure 1.2).

The detector is an improved version of the magnetic spectrometers which provided the earlier published results. A schematic diagram of the instrument is shown in Figure 1.3. Two digitized (magnetic core

readout) spark chambers are used to observe particle trajectories above and below the gap region of a permanent magnet with pole faces of dimensions 15 x 15 cm^2 and a gap spacing of 8 cm. The central field strength is approximately 1 kilogauss, and the total field integral is nearly 25 kilogauss-cm. A fast telescope system employing four plastic scintillators and a gas Cerenkov threshold counter triggers the high-voltage pulsing and readout of the spark chambers. The geometric factor (19 cm^2 sr) is determined by the configuration of scintillators, while as in earlier detectors the Cerenkov counter imposes both a directional and a minimum velocity requirement on incident particles. The choice of carbon dioxide at 1 atm as the radiating medium for the flights reported here was made to prevent instrument triggers by protons below about 30 GeV.

In the present detector an additional means of distinguishing electrons from heavier particles is provided by a vertical stack of sandwiched lead-alloy plates and two plastic scintillators located beneath the lower spark chamber. This package (which contains three radiation lengths of lead above the lower scintillator) serves as a counter array in which the shower development caused by electron bremsstrahlung can be measured. Signals from the shower counter phototubes are sent to pulse height analyzers in the detector electronics package and transmitted to the ground along with spark chamber data and housekeeping information. The PHA outputs are stored with corresponding spark event records for use in post-flight data analysis. The additional event selection criteria provided by the shower counters are essential for the adequate rejection of energetic protons and other heavy particles which may produce single-particle tracks in the spark chambers.

A more complete description of the instrument will be presented in Chapter V. The analysis of the data from the two successful flights in 1972 is described in Chapter VI, while the discussion and interpretation of the results are reserved for Chapter VII. The results to be considered include a confirmation of earlier measurements of the positive fraction reported by Hartman (1967), Fanselow et al. (1969) and Beuermann et al. (1970). In addition, new estimates have been obtained for the positive fraction of atmospheric secondary electrons at balloon float altitudes. Finally, the total electron (and negatron) intensities over the range 50-800 MV in 1972 have been estimated, and finite values or upper limits have been established for the corresponding positron intensities.

Chapters II to IV of the present work are intended to provide an introduction to the astrophysical background implicit in the discussion of the final results. The available calculations of galactic secondary electron production and the propagation of energetic electrons in the interstellar medium are considered in Chapters II and III, while Chapter IV describes the influence of the solar wind on interstellar electrons penetrating the solar system.

Although the results of the present experiment confirm earlier evidence for the existence of primary electron sources in the galaxy, a discussion of the nature of these sources will not be attempted here. The importance of this subject is presently overshadowed by the inadequate observational basis for choosing between a variety of plausible mechanisms which may accelerate electrons in pulsars, supernova explosions, the galactic nucleus, or even regions of interstellar space. The resolution of this question must await further observations of the cosmic ray

CHAPTER II

GALACTIC SECONDARY ELECTRONS

The present chapter reviews several of the presently available calculations of galactic secondary electron production spectra. However, it must be noted at the outset that attempts to compare the results of these calculations with positron and negatron intensities observed near the earth have faced several persistent obstacles. In particular, the calculations must rely on semiempirical models or extrapolations of accelerator data (or data based on muon production in the atmosphere) to describe charged pion production in hadronic interactions. Most authors have also resorted to simplified kinematics in describing the subsequent $\pi^{\pm} \rightarrow \mu^{\pm} \rightarrow e^{\pm}$ decays which yield one secondary electron for each created pion.

The uncertain galactic parameters entering these calculations pose even more serious difficulties. The rate of secondary electron production in any region of the galaxy depends on the local interstellar gas density and its precise composition as well as the ambient cosmic ray intensities. Unfortunately, only crude average values of these quantities are available at present.

As the following chapters will demonstrate, the relation between the production spectra of secondary (or primary) electrons and their intensity observed near the earth also remains quite uncertain. The interstellar propagation of electrons (and nucleonic cosmic rays), which tend to be confined within the disordered galactic magnetic field, is still not fully understood. Hence the extent of the galactic regions

confining the electrons, and the rate of leakage from these regions, are matters of controversy. In addition, attempts to describe the transport of electrons from their sources to the vicinity of the earth can only crudely estimate the significant energy losses due to the presence of interstellar matter, the galactic magnetic field, and the background radiation fields of starlight and universal microwave photons.

The local distortion of interstellar cosmic ray intensities by the solar wind creates equally serious problems in comparing the predicted and observed electron spectra below several GeV. While the variable solar modulation of the galactic nucleonic intensities has only slight effects in secondary production calculations (which depend largely on the nucleonic flux at high energies) direct measurements of the electronic component near the earth cannot be readily compared to the expected interstellar flux levels. This fact, however, lends particular significance to measurements of the positive fraction $\frac{N_e^+}{N_e^+ + N_e^-}$ of galactic electrons. If this quantity does not vary significantly with energy over a scale comparable to their energy losses, its value should remain essentially unchanged as the particles penetrate the solar cavity. Hence direct measurements of the positive function may provide the least ambiguous test of the secondary origin hypothesis.

In principle, comparisons of the magnetic bremsstrahlung (synchrotron radiation) expected from estimated secondary intensities with radio observations (Webber, 1968) also avoid the questions of solar modulation. However, in this case the uncertainties in galactic magnetic field strengths have a significant effect on estimates of the expected radio emission.

In spite of the somewhat murky situation, the procedure usually followed has been that of employing a set of consistent and currently plausible galactic parameters to draw tentative conclusions about the adequacy of the secondary source model. Such comparisons with the two measured quantities (charge ratio and synchrotron emission) which best avoid the problems of solar modulation both point to the existence of a primary electron flux which is comparable to and probably greater than the secondary intensities from about 300 MeV to over 10 GeV. In the case of the radio measurements this conclusion is based on the difficulty in matching both the observed intensity and spectral shape using only the secondary production model (see for example Ramaty and Lingenfelter, 1966). The charge ratio measurements seem to be on even firmer ground. Over energies ranging from about 50 MeV to at least 10 GeV, the calculations predict a positive excess while Figure 1.1 indicates that there is in fact a definite negative excess above a few hundred MeV.

The present chapter reviews several recent calculations of secondary electron production in order to arrive at the estimated source spectra. Chapter III treats the problems of energy loss, leakage, and propagation through the galaxy, all of which must be accounted for in calculating the equilibrium energy spectra. The effects of solar modulation on galactic electrons are discussed in Chapter IV.

A. Cosmic Ray Collisions with Interstellar Matter

The most abundant source of galactic secondary electrons above about 50 MeV arises from the collisions of cosmic ray (CR) protons with interstellar hydrogen. The early calculations by Hayakawa and Okuda (1962), Jones (1963), Pollack and Fazio (1965) and Ginzburg and Syrovatskii (1964) are restricted to this source alone. Ramaty and Lingenfelter (1966) and Perola et al. (1967) have also considered the less frequent collisions between CR protons and interstellar helium, and conversely between CR α-particles and hydrogen. These shall be referred to below as pp , pα , and αp collisions, respectively. All other possibilities of cosmic ray hadronic interactions with interstellar nuclei are far too rare to be important in secondary electron production. It is worth noting, however, that toward the low energy region (below about 50 MeV), simple ionization of the interstellar gas by CR particles becomes the dominant electron source mechanism (Abraham, Brunstein, and Cline, 1966). At still lower energies ($\leqslant$ 2 MeV), positron decay of light nuclei should provide a significant positron source. These low energy galactic electrons will not be considered further in the present work, which is restricted to the portion of the spectrum above 50 MeV.

There are thus only two types of nuclear collisions to be considered, for which Ramaty and Lingenfelter (1966) have listed the principal direct reaction products shown in Table 2.1. Here a and b are, of course, nonnegative integers which may be varied arbitrarily and independently to give all the possible reaction products.

TABLE 2.1

PRINCIPAL REACTION PRODUCTS IN INTERSTELLAR COLLISIONS

$$p + p \rightarrow p + p + a(\pi^+ + \pi^-) + b\pi^o$$
$$\rightarrow p + n + \pi^+ + a(\pi^+ + \pi^-) + b\pi^o$$
$$\rightarrow 2n + 2\pi^+ + a(\pi^+ + \pi^-) + b\pi^o$$

$$p + He^4 \rightarrow p + He^4 + a(\pi^+ + \pi^-) + b\pi^o$$
$$\rightarrow p + He^3 + n + a(\pi^+ + \pi^-) + b\pi^o$$
$$\rightarrow 2p + H^2 + n + a(\pi^+ + \pi^-) + b\pi^o$$
$$\rightarrow 4p + n + \pi^- + a(\pi^+ + \pi^-) + b\pi^o$$
$$\rightarrow 3p + 2n + a(\pi^+ + \pi^-) + b\pi^o$$
$$\rightarrow 2p + 3n + \pi^+ + a(\pi^+ + \pi^-) + b\pi^o$$
$$\rightarrow p + 4n + 2\pi^+ + a(\pi^+ + \pi^-) + b\pi^o$$

The charged pions and neutrons generated in these interactions rapidly produce electrons via the weak decay processes

$$\pi^+ \rightarrow \mu^+ + \bar{\nu}_\mu \quad (\mu^+ \rightarrow e^+ + \nu_e + \bar{\nu}_\mu) \qquad 2.1a$$

$$\pi^- \rightarrow \mu^- + \nu_\mu \quad (\mu^- \rightarrow e^- + \bar{\nu}_e + \nu_\mu) \qquad 2.1b$$

$$n \rightarrow p + e^- + \bar{\nu}_e \qquad 2.1c$$

Although the neutron has a relatively long lifetime (930 s) compared with those of the pion (10^{-8} s) and muon (10^{-6} s), all three particles are highly unstable on the time scale of their propagation through the galaxy. Hence, the principal source mechanism (pp collisions) must

generate equal numbers of secondary positrons and negatrons. Their individual energy spectra, however, are quite different. This is due primarily to the fact that most of the negatrons from neutron decay are restricted to the lower energy region dominated by galactic knock-on electrons. In fact, the electron source spectrum due to neutron decays need not be considered further here.

The possibility of kaon or hyperon production in the collision processes listed above has so far been ignored. As Ramaty and Lingenfelter (1966) point out, the kaon production cross section is only 10-20% of that for pions, and a much smaller fraction of the total energy is imparted to these heavier mesons. Similar statements are assumed to hold true for all the more exotic hadronic reaction products.

B. Pion Production Spectrum

Estimates of pion production rates in the collision processes listed above have been made in several ways which vary in their empirical content. Comparisons can best be made by first enumerating the quantities which enter into the calculation and combining them to obtain a general expression for the pion production spectrum. With the overall framework in view, it becomes fairly straightforward to isolate the differences in the calculations made to date.

The most general approach to the problem begins with the distribution functions for the relevant species of particles comprising the cosmic rays and the interstellar gas. Thus the number of CR protons within the galactic volume element d^3x whose velocities are all within d^3v_p (in the galactic rest frame) is given by $f_p(\underline{x}, \underline{v}_p)\, d^3x\, d^3v_p$. (If only magnetic fields may act on these particles, their energies are of course determined by their velocities.) The distribution function for the hydrogen component of the interstellar gas may be denoted by $f_H(\underline{x}, \underline{v}_H)\, d^3x\, d^3v_H$ The subscript H is intended in principle to include the low-energy free protons (ionized hydrogen) present in the galactic medium as well as protons bound in atomic and molecular hydrogen. Similarly, the distribution functions for CR α-particles and galactic helium may be written as $f_\alpha(\underline{x}, \underline{v}_\alpha)$ and $f_{He}(\underline{x}, \underline{v}_{He})$ respectively.

It simplifies matters at the outset, however, to replace the distribution functions for the interstellar gas constituents by their spatial densities, which are obtained by integrating over velocities:

$$n(\underline{x}) = \int d^3v\, f(\underline{x}, \underline{v})$$

The velocity distributions are sharply peaked around $\underline{V} = \underline{0}$, since the vast bulk of the interstellar medium possesses fairly low kinetic temperatures (10^2 - 10^4 ° K). Hence, nuclear cross sections derived or obtained under accelerator conditions (high energy beam, target at rest) can be applied directly to the galactic environment.

A further simplification results from the apparently safe assumption that at any point $\underline{x}$ in the galaxy the cosmic ray flux is essentially isotropic. Then it is sufficient to employ CR distribution functions whose arguments are position and particle energy (or equivalently, the Lorentz factor $\gamma = \frac{E}{m}$). In the following development the starting point will be the spectral intensities $\mathcal{J}_p(\underline{x}, \gamma_p)$ and $\mathcal{J}_\alpha(\underline{x}, \gamma_\alpha)$, whose units may be chosen to be $cm^{-2}\ s^{-1} sr^{-1}\ \gamma^{-1}$. Corresponding CR densities are obtained by multiplying the intensities by $\frac{4\pi}{c}$, since the CR particles of importance in secondary production all have near-light velocities.

At this stage it is necessary to introduce the inclusive charged pion production cross section, $\frac{d^3\sigma^{\pm}}{d^3V_\pi}$. Here $d^3\sigma^{\pm}$ gives the number of events producing a pion whose velocity is centered on d^3V_π in the rest frame of the target particles, divided by the incident flux and the number of targets. The term inclusive indicates that anything else, including other pions, may be created in the same process. However, the element d^3V_π is assumed to be small enough so that each event injects at most one pion into d^3V_π Thus the number of pions within d^3V_π is given directly by the number of events.

Again it is possible to simplify the treatment by noting that the isotropic flux or cosmic rays implies an isotropic distribution of created

pions in the galactic rest frame. Hence it is worthwhile to integrate $\frac{d^3\sigma^{\pm}}{d^3 V_\pi}$ over angles to get $\frac{d\sigma^{\pm}}{d\gamma_\pi} d\gamma_\pi$, the number of pions produced with energies between γ_π and $\gamma_\pi + d\gamma_\pi$, divided again by the incident flux and number of targets. Then the total number of charged pions in the range $d\gamma_\pi$ generated cm^{-3} sec^{-1} by CR particles having energies in the range $d\gamma$ may be immediately written as

$$4\pi J(\underline{x}, \gamma)\, n(\underline{x})\, \frac{d\sigma^{\pm}}{d\gamma_\pi}(\gamma, \gamma_\pi)\, d\gamma_\pi\, d\gamma$$

Integrating over $d\gamma$ yields the pion production spectrum in $(cm^{-3} sec^{-1} \gamma_\pi^{-1})$

$$q_\pi^{\pm}(\gamma_\pi)\, d\gamma_\pi = d\gamma_\pi \int d\gamma\, 4\pi J(\underline{x}, \gamma) n(\underline{x}) \frac{d\sigma^{\pm}}{d\gamma_\pi}(\gamma, \gamma_\pi) \qquad 2.2$$

The quantity $\frac{d\sigma^{\pm}}{d\gamma_\pi}$ may be expressed in terms or center-of-momentum (CM) distribution functions over pion energies and angles. Let $f^{\pm}(\gamma_\pi^*)$ give the distribution over CM pion Lorentz factors and $g^{\pm}(\Omega^*)$, that over CM emission angles. None of the pion production models to be considered involves an azimuthal dependence in the CM frame (neither beam nor target is polarized), so $g^{\pm}(\Omega^*)$ depends only on cos θ . Also let $m^{\pm}(\gamma)$ be the multiplicity of created charged pions as a function of incident particle energy, and σ_o, the total inelastic collision cross section. σ_o is known to have a nearly constant value of about 27 mb over the energies of interest in secondary production. Thus the multiplicities may be derived from the cross sections using the relation

$$m^{\pm}(\gamma) = \frac{\sigma^{\pm}}{\sigma_o} = \frac{\int d\gamma_\pi \frac{d\sigma^{\pm}}{d\gamma_\pi}}{\sigma_o} \qquad 2.3$$

With these quantities defined, it is possible to relate the number of created pions corresponding to the interval $d\gamma\, d\gamma_\pi^*\, d(\cos\theta^*)$ to the number within $d\gamma\, d\gamma_\pi^*\, d\gamma_\pi$:

$$4\pi j(\underline{x},\gamma)\, n(\underline{x})\,(m^\pm(\gamma)\sigma_0)\, f^\pm(\gamma_\pi^*)\, g^\pm(\cos\theta^*)\, d\gamma\, d\gamma_\pi^*\, d(\cos\theta^*) \qquad 2.4$$

$$= 4\pi j(\underline{x},\gamma)\, n(\underline{x})\,(m^\pm(\gamma)\sigma_0)\, f^\pm(\gamma_\pi^*)\, g^\pm(\cos\theta^*)\, J\left(\frac{\gamma, \gamma_\pi^*, \cos\theta^*}{\gamma, \gamma_\pi^*, \gamma_\pi}\right) d\gamma\, d\gamma_\pi^*\, d\gamma_\pi$$

$$= 4\pi j(\underline{x},\gamma)\, n(\underline{x})\,(m^\pm(\gamma)\sigma_0)\, f^\pm(\gamma_\pi^*)\, g^\pm(\cos\theta^*)\, \frac{d\gamma\, d\gamma_\pi^*\, d\gamma_\pi}{\sqrt{\gamma_\pi^{*2}-1}\sqrt{\frac{\gamma-1}{2}}}$$

Here the Jacobian has been evaluated using the expression

$$\gamma_\pi = \gamma_\pi^*\sqrt{\frac{\gamma+1}{2}} + \sqrt{(\gamma_\pi^{*2}-1)\left(\frac{\gamma-1}{2}\right)}\cos\theta^* \qquad 2.5$$

Integration over $d\gamma_\pi^*$ leads to the equality

$$4\pi j(\underline{x},\gamma)\, n(\underline{x})\, \frac{d\sigma^\pm}{d\gamma_\pi}\, d\gamma_\pi\, d\gamma \qquad 2.6$$

$$= 4\pi j(\underline{x},\gamma)\, n(\underline{x})\, \frac{m^\pm(\gamma)\sigma_0}{\sqrt{\frac{\gamma-1}{2}}} \int_1^\infty \frac{d\gamma_\pi^*}{\sqrt{\gamma_\pi^{*2}-1}} f^\pm(\gamma_\pi^*)\, g^\pm(\cos\theta^*)\, d\gamma_\pi\, d\gamma$$

Thus $$\frac{d\sigma^\pm}{d\gamma_\pi}(\gamma,\gamma_\pi) = \frac{m^\pm(\gamma)\sigma_0}{\sqrt{\frac{\gamma-1}{2}}} \int_1^\infty \frac{d\gamma_\pi^*}{\sqrt{\gamma_\pi^{*2}-1}} f^\pm(\gamma_\pi^*)\, g^\pm\left[\cos\theta^*(\gamma,\gamma_\pi,\gamma_\pi^*)\right]$$

2.7

The pion production spectrum is, of course, directly expressible in terms of CM quantities:

$$q_\pi^\pm(\gamma_\pi)\, d\gamma_\pi = d\gamma_\pi\, 4\pi n(\underline{x}) \int_1^\infty d\gamma_\pi^*\, \frac{f^\pm(\gamma_\pi^*)}{\sqrt{\gamma_\pi^{*2}-1}} \int_{\gamma^-}^{\gamma^+} d\gamma\, j(\underline{x},\gamma)\, \frac{m^\pm(\gamma)\sigma_0}{\sqrt{\frac{\gamma-1}{2}}}\, g^\pm\left[\cos\theta^*(\gamma,\gamma_\pi,\gamma_\pi^*)\right]$$

2.8

The limits of integration, $\gamma^{\pm}$, are found by solving the equation

$$\gamma_\pi = \gamma_\pi^* \sqrt{\frac{\gamma+1}{2}} \pm \sqrt{(\gamma_\pi^{*2}-1)\left(\frac{\gamma-1}{2}\right)} \qquad 2.9$$

for γ as a function of γ_π and γ_π^*.

Within this framework there are several possible methods of evaluating $q_\pi^{\pm}(\gamma_\pi)$. One approach is simply to compile and extrapolate experimental data from accelerators or cosmic ray interactions in the atmosphere and insert the empirical values for $\frac{d\sigma^{\pm}}{d\gamma_\pi}$ in equation 2.2. A second method is one of using models which predict the CM quantities $f^{\pm}(\gamma_\pi^*)$ and $g^{\pm}(\cos\theta^*)$, as well as σ_o and $m^{\pm}(\gamma)$. Due to the current status of strong coupling theories, however, in practice many aspects of the models themselves are totally empirical.

The early calculation by Hayakawa and Okuda (1962) uses the second approach. Considering only pp collisions, they introduce approximate functions for $f^{\pm}(\gamma_\pi^*)$, $g^{\pm}(\cos\theta^*)$, the product $m^{\pm}(\gamma)\sigma_o$, and spatially uniform densities and intensities based on the data available to them. Their resulting source spectra are intended to include contributions from proton energies ranging between 1 GeV and 100 GeV, but their choice of the proton spectral index 2.15 and somewhat obsolete data on pp collisions have been improved upon by later authors.

The treatment by Jones (1963) depends on a more detailed model of inelastic collisions. In particular, he assumes the existence of excited nucleon states called isobars in addition to the more venerable fireballs (excited meson clouds) which move slowly in the CM frame. In this frame the more energetic isobars are assumed to move forward or backward along the collision direction and to decay with the isotropic emission (in their rest frame) of one or more high energy pions. The isobar model

still assumes that the majority of the pions produced in energetic collisions are still evaporated from fireballs, but most of the energy is imparted to the smaller number resulting from isobar decay.

Jones (1963) first evaluates the source spectra of isobars and fireballs using details of the isobar models proposed by Sternheimer and Lindenbaum (1961) and by Peters (1962). He then arrives at a pion source spectrum by adding contributions from decays of the various intermediate states, using the expression

$$q_\pi(\gamma_\pi)\,d\gamma_\pi = d\gamma_\pi \sum_i \int_{\gamma_\pi^*}^{\infty} \frac{f_i(\gamma_\pi^*)\,d\gamma_\pi^*}{2\sqrt{\gamma_\pi^{*2}-1}} \int_{\gamma_c^-}^{\gamma_c^+} d\gamma_c \; \frac{q_i(\gamma_c)}{\sqrt{\gamma_c^2-1}} \qquad 2.10$$

Here γ_c is the Lorentz factor (in the galactic rest frame) of the decaying state i, which has the source spectrum $q_i(\gamma_c)$. The limits of integration are

$$\gamma_c^{\pm} = \gamma_\pi \gamma_\pi^* \pm \sqrt{(\gamma_\pi^2-1)(\gamma_\pi^{*2}-1)} \qquad 2.11$$

Unlike Hayakawa and Okuda (1962), Jones (1963) does not attempt to calculate separate positron and negatron spectra. One of the limitations of his model is that it does not predict the multiplicity for each charged pion. His results, which also depend on an assumed proton spectral index of 2.5, can thus only be compared with radio observations or total intensity measurements at high energies.

Pollack and Fazio (1965) start with data on the CM distributions $f^{\pm}(\gamma_\pi^*)$ and $g^{\pm}(\cos\theta^*)$ and construct a histogram version of the distribution function $h^{\pm}(\gamma_e, \gamma_p)$ directly relating produced electron energies γ_e to the incident proton energies γ_p. Since in their approach each electron receives on the average an energy $\gamma_e = 0.25\,\gamma_\pi$, their pion

spectrum is implicitly contained in their electron source spectrum

$$q_e^{\pm}(\gamma_e)d\gamma_e = 4\pi d\gamma_e \int d\gamma_p\, h^{\pm}(\gamma_e,\gamma_p) j_p(\gamma_p) \sigma_o m^{\pm}(\gamma_p) \left[\frac{\int_{disk} d^3x\, n(\underline{x})}{V_{halo}} \right] \qquad 2.12$$

The factor in brackets results from their assumption that secondary production occurs uniformly throughout the galactic disk, but that the electrons are confined only within a larger halo. The question of the existence of the halo will be examined in Chapter III.

In contrast to the previous treatments, Ginzburg and Syrovatskii (1964) use a completely empirical pion spectrum inferred from data on the atmospheric secondary production of muons. They construct a graph of the spectral intensities $f_\pi^{\pm}(\gamma_\pi)$ of charged pions generated by the CR proton flux traveling through one absorption mean free path λ. This method relies directly on the assumption that the energetic proton spectrum at the top of the atmosphere is equal to the galactic flux. Their calculation also involves the approximation $f_\pi(\gamma_\pi) \simeq f_\mu(\gamma_\mu)$, which is discussed in Section C. The intensities $f_\pi^{\pm}(\gamma_\pi)$ are related to the pion production spectra by the expression

$$q_\pi^{\pm}(\gamma_\pi)d\gamma_\pi = \frac{4\pi\rho_H}{\lambda} f_\pi^{\pm}(\gamma_\pi)d\gamma_\pi \qquad 2.13$$

where ρ_H is the mean density (in gm cm^{-3}) of interstellar hydrogen.

Ramaty and Lingenfelter (1966) note that the resultant electron spectra given by Ginzburg and Syrovatskii (1964) are somewhat lower than those found in their own later calculation. The discrepancy is due in part to the lower value of the hydrogen density chosen by Ginzburg and Syrovatskii (1964), and also to possible errors in their atmospheric data for pion energies below 500 MeV.

The calculations by Ramaty and Lingenfelter (1966) and Perola et al. (1967) are based on pion (and neutron) production cross sections measured in accelerator experiments prior to 1966. At that time the cross sections for pp collisions were well established from about 300 MeV to 10 GeV. A few measurements had extended the range to about the range to about 25 GeV. Ramaty and Lingenfelter (1966) also incorporate cosmic ray measurements at 2800 GeV and some general extrapolations to reach 1000 GeV. The data available on pion and neutron production in $p\alpha$ and αp collisions, though not so well established, allow them to cover the same energy range (of kinetic energy per nucleon) in both cases.

Ramaty and Lingenfelter (1966) further use the observed dependence of the mean pion kinetic energy on incident energy to make a delta function approximation for the pion energy distribution. Hence their source spectra have the form

$$\begin{aligned} q_\pi^\pm(\gamma_\pi) &= 4\pi \int_1^\infty d\gamma_p \, J_p(\gamma_p) \, n_H \sigma_{pp}^\pm(\gamma_p) \, \delta[\gamma_\pi - g_{pp\pi}(\gamma_p)] \\ &+ 4\pi \int_1^\infty d\gamma_p \, J_p(\gamma_p) \, n_{He} \sigma_{p\alpha}^\pm(\gamma_p) \delta[\gamma_\pi - g_{p\alpha\pi}(\gamma_p)] \\ &+ 4\pi \int_1^\infty d\gamma_\alpha \, J_\alpha(\gamma_\alpha) n_H \sigma_{\alpha p}^\pm(\gamma_\alpha) \delta[\gamma_\pi - g_{\alpha p\pi}(\gamma_\alpha)] \end{aligned} \qquad 2.14$$

Here $g_{pp\pi}$, $g_{p\alpha\pi}$, and $g_{\alpha p\pi}$ are the mean values of γ_π for pions created in pp, $p\alpha$, and αp interactions. The delta function approximation permits an immediate integration of the source spectra given in equation 2.15

$$\begin{aligned} q_\pi^\pm(\gamma_\pi) = {} & 4\pi J_p[g_{pp\pi}^{-1}(\gamma_\pi)] \, n_H \, \sigma_{pp}^\pm[g_{pp\pi}^{-1}(\gamma_\pi)] \Big/ \frac{dg_{pp\pi}}{d\gamma_p}[g_{pp\pi}^{-1}(\gamma_\pi)] \\ & + 4\pi J_p[g_{p\alpha\pi}^{-1}(\gamma_\pi)] \, n_{He} \sigma_{p\alpha}^\pm[g_{p\alpha\pi}^{-1}(\gamma_\pi)] \Big/ \frac{dg_{p\alpha\pi}}{d\gamma_p}[g_{p\alpha\pi}^{-1}(\gamma_\pi)] \\ & + 4\pi J_\alpha[g_{\alpha p\pi}^{-1}(\gamma_\pi)] \, n_H \, \sigma_{\alpha p}^\pm[g_{\alpha p\pi}^{-1}(\gamma_\pi)] \Big/ \frac{dg_{\alpha p\pi}}{d\gamma_\alpha}[g_{\alpha p\pi}^{-1}(\gamma_\pi)] \end{aligned} \qquad 2.15$$

Their input spectrum of CR protons has the usual form

$$J_p(\gamma_p) = K_p \gamma_p^{-\Gamma}$$

for which they choose $K_p = 1.0\ cm^{-2} s^{-1} sr^{-1} \gamma_p^{-1}$ and $\Gamma = 2.5 \pm 0.2$. Their value of the spectral index Γ, like those quoted by previous authors, is somewhat lower than the currently accepted value of $2.7 \pm .05$. For CR α-particles they use the intensity

$$J_\alpha(\gamma_\alpha) = .067 J_p(\gamma_p)$$

Two possible values for the mean galactic hydrogen density are assumed, namely .015 and .03 cm^{-3}. For each case the helium density is set by the assumption $n_{He} = 0.1 n_H$. These choices for n_H and n_{He} are both based on the assumption of a galactic halo as the region confining the cosmic ray flux.

Improved versions of this pion source spectrum calculation have been obtained by Ramaty and Lingenfelter (1968) and more recently by Ramaty (1973). At high energies the latter treatment follows a recent pion production calculation by Choate and Wayland (1972), based on a two-temperature statistical model of high-energy interactions in which the CM longitudinal and transverse momentum distributions of pions evaporated from fireballs are essentially decoupled.

The results obtained by Ramaty (1973) are shown in Figure 2.1. Here two forms of the CR proton spectrum have been assumed in order to evaluate the effect of uncertainties in the solar modulation of cosmic rays (see Chapter IV). The solid line corresponds to a proton spectrum identical to that observed at the earth near solar minimum, while the dashed line has been demodulated to an assumed interstellar shape (Ramaty, 1973).

The extrapolation of these pion source spectra to collision energies above 100 GeV must at present rely on theoretical models or general assumptions of limiting behavior at high energies. A recent calculation of this type by Dooher (1972) incorporates the hypothesis of scaling in high-energy nucleonic collisions. This term refers to the prediction made by Feynman (1969) and others (Amati et al., 1962; Wilson, 1963) that the inclusive cross sections $\frac{d\sigma^{\pm}}{d\gamma_\pi}$ smoothly approach a limiting form at high energies. More precisely, if $p_{\parallel}^*$ and $p_{\perp}^*$ are the CM longitudinal and transverse momenta of pions created in collisions between nucleons of four-momenta p_1 and p_2, scaling asserts that the invariant differential cross section smoothly approaches the limiting form

$$2 m_\pi \gamma_\pi^* \frac{d^3\sigma^{\pm}}{dp_{\parallel}^* d^2 p_{\perp}^*} \xrightarrow[s\to\infty]{} F^{\pm}(x, p_{\perp}^*) \qquad 2.16$$

where $s = (p_1 + p_2)^2$

and $x = \frac{2 p_{\parallel}^*}{\sqrt{s}}$.

The invariant s is the square of the total CM energy, and x is called the Feynman scaling parameter. The limiting cross section defined above does not depend on the absolute magnitudes of the CM energy or the longitudinal pion momentum individually, but only on the ratio x.

With the assumption that transverse pion momenta remain small (less than 1 GeV/c), a transformation to the laboratory frame shows that the inclusive cross sections should tend toward the high-energy limit

$$\frac{d\sigma^{\pm}}{d\gamma_\pi} \longrightarrow \frac{m_\pi g^{\pm}\left[\frac{m_\pi}{M}\left(\frac{\gamma_\pi}{\gamma+1}\right)\right]}{\left[m_\pi^2 \gamma_\pi^2 + 2 m_+^2 (\gamma+1)\right]^{1/2}} \qquad (2.17)$$

where M is the nucleon mass and $m_+^2 = \langle p_{\perp}^{*2} \rangle + m_\pi^2$.

Here the function $g^{\pm}(x) = \pi \int F^{\pm}(x, p_{\perp}^{*}) dp_{\perp}^{*2}$ must be determined empirically (see for example Bali et al., 1970).

Recent data from the ISR and NAL accelerators confirm that the equation 2.16 is valid for pion production at energies ranging from below 20 GeV to at least 2000 GeV. Furthermore, atmospheric muon data appear to confirm that the scaling hypothesis holds to energies as high as 40 TeV (Ashley et al., 1973). Hence a calculation of the type made by Dooher (1972) should give a reasonable estimate of the electron production spectrum from a few GeV to at least 1000 GeV. However, at lower energies the recent calculation by Ramaty (1973) probably gives more reliable estimates.

C. Muon Production Spectrum

All the authors mentioned in the previous section make the same approximation in deriving the muon spectrum resulting from charged pion decays. Since there are only two ejected particles, the energy of the muon in the CM frame is fixed. In fact

$$\gamma_\mu^{CM} = \frac{m_\pi^2 + m_\mu^2}{2 m_\pi m_\mu} = 1.04 \qquad 2.18$$

This low value implies that for large γ_π, $\gamma_\mu \simeq \gamma_\pi$. Then it is immediately possible to set

$$q_\mu(\gamma_\mu) \simeq q_\pi(\gamma_\pi) \qquad 2.19$$

The assumption of large γ_π is not used in the exact treatment of electron production from pions by Scanlon and Milford (1965). Their work retains only the assumption of an isotropic angular distribution of ejected muons in the pion CM frame. However, these authors derive only the electron spectra resulting from monoenergetic (and isotropic) pion fluxes. They make no attempt to insert a pion production spectrum into their calculation. Ramaty and Lingenfelter (1966) have compared their own results at several pion energies with the exact treatment by Scanlon and Milford (1965) and find no serious differences for $\gamma_\pi \gtrsim 1.5$.

D. Electron Production Spectrum

The calculation of electron production from the muon spectrum must deal with the three-body decay of a spin-1/2 particle. In the muon rest frame the emitted electron can have energies as high as 52 MeV, so the approximation made in the last section cannot be made. Furthermore, the electron distribution $f(\gamma_e^*, \Omega_e^*)$ is anisotropic with respect to the muon spin direction in the CM frame. Its generally accepted form is

$$f(\gamma_e^*, \Omega_e^*) \propto \gamma_e^{*2} d\gamma_e^* d(\cos\theta_e^*)\left[3 - 2\frac{\gamma_e^*}{\gamma_{e\,MAX}^*}\right](1 - \alpha\cos\theta_e^*) \qquad 2.20$$

where $\gamma_{e\,MAX}^* \simeq \frac{m_\mu}{2m_e}$ and $\alpha = \left(\frac{2\gamma_e^*}{\gamma_{e\,MAX}^*} - 1\right)\Big/\left(3 - \frac{2\gamma_e^*}{\gamma_{e\,MAX}^*}\right)$

Integration over the CM solid angles $d\Omega_e^*$ yields the electron energy distribution (normalized to unity)

$$P(\gamma_e^*) = 2\gamma_e^{*2}\left(3 - \frac{2\gamma_e^*}{\gamma_{e\,MAX}^*}\right)\Big/\gamma_{e\,MAX}^{*3} \qquad 2.21$$

The above expression corresponds to the choice of Michel parameter $\rho = \frac{3}{4}$, which in turn implies a negative helicity for the $\bar{\nu}_\mu$ (Michel, 1949).

Most of the calculations already mentioned ignore the moderate anisotropy. The distribution function $f(\gamma_e^*, \Omega_e^*)$ is simply replaced by

$$\tilde{f}(\gamma_e^*, \Omega_e^*) = \frac{1}{4\pi} P(\gamma_e^*) \qquad 2.22$$

The exact treatment for monoenergetic pions by Scanlon and Milford (1965) uses the correct distribution. However, further comparisons by Ramaty and Lingenfelter (1966) still reveal no serious discrepancies in all

final results as long as $\gamma_\pi > 1.5$.

The approximate angular distribution leads immediately to the source spectra

$$q_e^{\pm}(\gamma_e)\,d\gamma_e = d\gamma_e \int_1^{\gamma_{e\,MAX}^*} \frac{d\gamma_e^*\, P(\gamma_e^*)}{2\sqrt{\gamma_e^{*2}-1}} \int_{\gamma_\pi^-}^{\gamma_\pi^+} \frac{d\gamma_\pi\, q_\pi^{\pm}(\gamma_\pi)}{\sqrt{\gamma_\pi^2-1}} \qquad 2.23$$

where $\gamma_\pi^{\pm} = \gamma_e^*\gamma_e \pm \sqrt{\gamma_e^{*2}-1}\sqrt{\gamma_e^2-1}$.

Ramaty and Lingenfelter (1966) further replace the true CM energy distribution $P(\gamma_e^*)$ by a delta function centered on the average ejection energy

$$\bar{\gamma}_e^* = \int_1^{\gamma_{e\,MAX}^*} d\gamma_e^*\, P(\gamma_e^*)\,\gamma_e^* \simeq \frac{7}{10}\,\gamma_{e\,MAX}^* \qquad 2.24$$

Hence their expression for the source spectra reduces to

$$q_e^{\pm}(\gamma_e)\,d\gamma_e = d\gamma_e \frac{1}{2\sqrt{\bar{\gamma}_e^{*2}-1}} \int_{\gamma_\pi^-}^{\gamma_\pi^+} d\gamma_\pi \frac{q_\pi^{\pm}(\gamma_\pi)}{\sqrt{\gamma_\pi^2-1}} \qquad 2.25$$

In the revised calculation by Ramaty (1973), the form for $P(\gamma_e^*)$ in equation 2.21 is used in a numerical integration of equation 2.23. The resulting positron and negatron source spectra are given in Figure 2.2. The solid and dashed curves correspond to the choices for the pion production spectrum (see Figure 2.1). Also shown are the results for positrons obtained by Perola et al. (1967).

CHAPTER III

EQUILIBRIUM SPECTRUM OF GALACTIC ELECTRONS

Electrons possess the largest charge-to-mass ratio of all the known fundamental particles. This property renders them the most vulnerable to the energy loss mechanisms which affect cosmic ray propagation through galactic space. These energy losses result from the presence of diffuse (and partially ionized) matter, background radiation in the forms of starlight and universal blackbody photons, and the weak interstellar magnetic field.

The magnetic field is also responsible for the confinement of both electrons and nucleonic cosmic rays to a region roughly comparable to (or perhaps much smaller than) the size of the galaxy. However, many details of the trapping mechanism are still not fully understood. The theories relating magnetic field irregularities and plasma wave interactions to cosmic ray scattering and diffusion processes rely on questionable galactic models and are still open to controversy. Their present status is so unsettled that it remains possible even to question the current preference for disk models to represent the effective storage region, although the halo model supported by radio astronomers until the middle sixties has in recent years encountered strong opposition.

In fact, it has not yet been strictly established that the observed electron spectrum actually satisfies quasi-steady state conditions within any fixed confinement volume. The usual justification for the assumed

existence of equilibrium spectra for galactic cosmic rays consists in studies of nuclear reaction products in meterorites. The possibility exists that roughly constant flux levels for nucleonic cosmic rays (to which these studies are really confined) do not imply a similar behavior in the electron component. If the bulk of the electron flux has been produced by different acceleration processes or within distinct galactic sources, this question may require careful attention.

In spite of this uncertainty, it has been almost a standard procedure to assume that steady state conditions do hold for the galactic electron flux. Several theoretical attempts to deduce an equilibrium spectrum (which will be discussed in Section C) have also treated electron confinement in terms of a single parameter, namely the leakage lifetime τ_e . This quantity is defined as the mean confinement time of electrons within the galaxy, and is assumed to be determined by their rate of diffusion or convection into the intergalactic medium. The most straightforward tests of theoretical equilibrium spectra based on the leakage lifetime approximation can be made at high energies (above about 10 GeV), for which the electron energy loss rate assumes the form $\frac{d\gamma_e}{dt} = -b\gamma_e^2$. If the source spectrum obeys a power law of the form $q_e(\gamma_e) = K\gamma_e^{-\Gamma}$ and τ_e is assumed to be an energy-independent quantity, then its value is associated with a critical energy $\gamma_c = (b\tau_e)^{-1}$ above which the equilibrium spectrum should asymptotically steepen by one power. However, the search for such an increase in Γ has so far provided only upper limits for τ_e . Recent measurements and theoretical criticism of this treatment have in fact prompted suggestions that τ_e must be regarded as an energy-dependent quantity or simply rejected as an inappropriate parameter for describing the confinement process.

Each of these questions will be considered at greater length in the following sections of this chapter. Section A discusses the energy loss mechanisms affecting electron propagation, while Section B reviews some physical aspects of scattering mechanisms and the confinement process. Finally, transport equations for galactic electron propagation and some properties of their solutions are described in Section C.

A. Energy Loss Mechanisms

The presence of diffuse galactic matter results in cosmic ray energy losses through ionization, or more generally, collisions with bound or free electrons in the medium. For electrons below a few hundred MeV, collision losses dominate all the other mechanisms of interest. The energy loss rates (expressed for convenience in terms of the Lorentz factor γ_e) due to collisions in neutral and fully ionized media may be written respectively as (Hayakawa, 1969)

$$-\left(\frac{d\gamma_e}{dt}\right)_I = 2\pi Z \frac{N}{A} c r_e^2 \frac{1}{\beta}\left[\ln\left(\frac{\gamma_e^3 \beta^2 (mc^2)^2}{2I^2}\right) + \frac{9}{8} - \beta^2\right] \qquad \text{(neutral)} \quad 3.1a$$

$$-\left(\frac{d\gamma_e}{dt}\right)_I = 2\pi n_e c r_e^2 \frac{1}{\beta}\left[\ln\left(\frac{\gamma_e \beta^2 (mc^2)^2}{(\hbar\omega_p)^2}\right) + 0.43\right] \qquad \text{(ionized)} \quad 3.1b$$

where Z, A, and N denote as usual the atomic number, mass number and Avogadro's constant. Standard symbols are also used for the fine structure constant $\alpha \equiv \frac{e^2}{\hbar c}$, the classical electron radius $r_e \equiv \frac{e^2}{mc^2}$, and the electron velocity $v = \beta c$. The quantity I in equation 3.1a is the average ionization potential, while n_e and ω_p in equation 3.1b denote the electron density and the plasma frequency of the ionized medium. The energy dependence of the collision loss rate is in either case much weaker than that associated with the other mechanisms discussed in this section.

The passage of electrons through interstellar matter also results in energy loss through bremsstrahlung (radiative collisions). However, Gould and Burbidge (1965) have shown that bremsstrahlung is dominated by other losses at nearly all energies. This process may in fact be completely neglected except over a fairly narrow region of energies near

1 GeV. In a neutral medium the bremsstrahlung energy loss rate has the asymptotic forms (Hayakawa, 1969)

$$-\left(\frac{d\gamma_e}{dt}\right)_B = 4Z(Z+1)\frac{N}{A}\alpha v r_e^2\left[\ln(2\gamma_e)-\frac{1}{3}\right]\gamma_e ,$$

$$1 \ll \gamma_e \ll 137Z^{-\frac{1}{3}} \quad \text{(no screening)} \qquad 3.2a$$

$$-\left(\frac{d\gamma_e}{dt}\right)_B = 4Z(Z+1)\frac{N}{A}\alpha v r_e^2\left[\ln(191Z^{-\frac{1}{3}})+\frac{1}{18}\right]\gamma_e ,$$

$$\gamma_e \gg 137Z^{-\frac{1}{3}} \quad \text{(complete screening)} \qquad 3.2b$$

If the medium is completely ionized, equation 3.2a is appropriate even for highly energetic electrons.

The bremsstrahlung loss rate is essentially proportional to γ_e for galactic electrons at high energies. However, for galactic propagation the expressions in 3.2a and 3.2b do not provide a completely satisfactory description of what is essentially a discontinuous process. Since individual radiative collisions often involve large energy changes, a more appropriate parameter for describing bremsstrahlung losses is the mean time between such encounters. This point is discussed briefly in Section C.

The energy densities in the background fields of universal blackbody photons and galactic starlight are sufficiently great to impose significant energy losses on electrons above several GeV through (inverse) Compton collisions. For each radiation field the corresponding loss rate depends on the ratio of γ_e to the quantity $\frac{mc^2}{\bar{\varepsilon}}$, where $\bar{\varepsilon}$ is the average energy of the background photons. The two limiting cases have the forms

$$-\left(\frac{d\gamma_e}{dt}\right)_C = \frac{4}{3}\frac{1}{mc}\sigma_{Th}\gamma_e^2 W_{ph} , \qquad \gamma_e \ll \frac{mc^2}{\bar{\varepsilon}} \qquad 3.3a$$

$$-\left(\frac{d\gamma_e}{dt}\right)_c = \frac{3}{8}\frac{1}{mc}\sigma_{Th}W_{ph}\left(\frac{mc^2}{\bar{\varepsilon}}\right)^2\left[\ln\left(\frac{2\gamma_e}{mc^2}\right)+\frac{1}{2}\right], \quad \gamma_e \gg \frac{mc^2}{\bar{\varepsilon}} \qquad 3.3b$$

Where σ_{Th} is the Thomson cross section and W_{ph} is the photon energy density (Hayakawa, 1969).

Energetic electrons also lose energy through synchrotron radiation (magnetic bremsstrahlung) associated with their spiraling motion along the interstellar magnetic field lines. As in the case of Compton scattering at moderately high energies, the synchrotron loss rate depends on γ_e^2. Its explicit form is given by (Hayakawa, 1969)

$$-\left(\frac{d\gamma_e}{dt}\right)_s = \frac{16\pi}{3}\frac{\gamma_e^2}{mc}\frac{H_\perp^2}{8\pi} \qquad 3.4a$$

where $H_\perp$ is the field component perpendicular to the instantaneous electron velocity. With the assumption that the galactic field strength is essentially uniform in magnitude but randomized in direction over scale lengths small compared to the confinement volume, it is possible to write the average energy loss rate in the simpler form

$$-\left(\frac{d\gamma_e}{dt}\right)_s = \frac{4}{9}\frac{\gamma_e^2}{mc}H^2 \qquad 3.4b$$

A comparison of the energy loss processes discussed above for electrons in the galaxy depends on the set of parameters chosen to describe the interstellar medium. Figure 3.1 (taken from Ramaty, 1973) lists some currently plausible values for the average matter density, photon energy densities in the background radiation fields, and the galactic magnetic field strength. These numbers were used to produce the curves shown in the same figure, which compare the loss rates due to collisions (I) bremsstrahlung (B), Compton scattering from starlight (C) and blackbody photons (C'), and synchrotron radiation (S).

Figure 3.1 shows that equation 3.3a may be used to describe Compton scattering from blackbody radiation at essentially all energies of interest, although for starlight photons the same approximation breaks down above about 100 GeV. For this set of galactic parameters, synchrotron radiation is evidently the dominant loss mechanism at high energies. Collisions with the blackbody photons rank second in importance. Hence in the first approximation, the total loss rate for electrons above about 10 GeV is proportional to γ_e^2 .

B. Propagation of Galactic Electrons

Much of the currently available information on the properties of the galactic magnetic field has recently been summarized in a review article by Parker (1971). The average field strength is now generally estimated to be on the order of 3 or 4 microgauss throughout the greater part of the disk. This value has been inferred from measurements of the polarization of starlight observed through interstellar dust (Hiltner, 1956; Purcell and Spitzer, 1971), Faraday rotation of the radio emission from polarized extragalactic sources (Davis and Merge, 1968), and Zeeman broadening of the 21-cm line from low-temperature hydrogen clouds (Verschuur, 1971). In most regions the main component tends to lie along the azimuthal direction. To some extent, the field lines (presumably frozen into the conductive interstellar medium) appear to follow the structure of the gaseous spiral arms. The lack of strong cosmic ray anisotropies at extremely high energies suggests that the field does not extend outward from the galactic rim but on the whole remains confined within the disk (Parker, 1971).

The propagation of cosmic rays along the field lines in inhibited by magnetic irregularities whose scale lengths have been roughly estimated at about 100 pc (see for example Jokipii and Lerche, 1969). Wentzel (1968) has argued that resonant interactions with hydromagnetic waves propagating along the field lines also act to damp out cosmic ray streaming velocities much greater than the Alfven velocity of the medium (about 100 km sec^{-1}). Since for most particles the radius of gyration is much smaller than the distance between field irregularities, however, the diffusion of particles across the field lines is still expected to proceed much more slowly than parallel diffusion. In fact, neither

process seems able to account for the known upper limits of about 10^6 yr for the mean cosmic ray residence time within the galaxy.

Parker (1966) has suggested a more efficient transport mechanism involving particle convection normal to the plane of the disk. In his model, regions of weakened magnetic fields, lying between the numerous dense clouds of cold gas, are inflated by cosmic ray pressure into expanding loops which escape outward from the plane of the disk. Hence both electrons and nucleonic cosmic rays, initially trapped in these expanding loops, essentially evaporate into what has generally been called the galactic halo region.

At one time a roughly spherical halo, whose radius should be comparable to that of the disk, was widely considered to be the effective confinement volume for cosmic rays. However, recent radio measurements have failed to support the earlier assumption that this region possesses average magnetic field strengths capable of trapping either electrons or nucleonic cosmic rays. While Daniel and Stephens (1970) argue that the present radio data should not be regarded as conclusive, direct observations of the galactic electron spectrum also appear to rule out the choice of the halo as the confinement volume. The search for an increase in the electron spectral index Γ has set an upper limit of about 3×10^6 yr for the halo residence lifetime. However, reasonable trapping field strengths predict diffusion times which range well above 3×10^7 yr. Hence the halo is evidently a very leaky object even if it is capable of partially confining the large numbers of cosmic rays which may emerge from the disk.

C. Electron Transport Equations

The equations describing electron propagation through the galaxy may be expressed in terms of the differential number density $u_e(\gamma_e, \underline{x})$. The product $u_e(\gamma_e, \underline{x})\, d\gamma_e\, d^3x$ gives the number of electrons at time t within the interval $d\gamma_e$ and the volume element d^3x, centered on the values γ_e and $\underline{x}$. The almost complete isotropy of the galactic electron flux insures that the transport equations for u_e are equivalent to those governing the differential intensity $J_e(\gamma_e, \underline{x})$, since $J_e = \frac{v u_e}{4\pi}$.

The treatment of electron propagation is similar in some respects to the transport theory of nucleonic cosmic rays. Both species of particles are assumed to participate in a random-walk process of scattering and diffusion through the irregular galactic magnetic field. Clusters of individual scattering centers (magnetic irregularities), whose net effect on the cosmic rays can be described by a diffusion tensor $D_{ij}(\underline{x})$, may also possess nonzero drift velocities with respect to the galactic rest frame. Within such regions the cosmic rays may also be subject to convection as well as diffusion.

The unique aspect of the electron component is its susceptibility to the energy loss mechanisms discussed in Section A. The equations describing the behavior of u_e must account for motion in energy space as well as the diffusive-convective transport of the particles through coordinate space. On the other hand, these energy changes may be regarded as essentially continuous processes. That is, for the most important loss mechanisms the individual particle collisions or photon emissions are not catastrophic. Instead the incremental changes in electron energies are small enough to allow the use of continuous loss rates as given in Section A. The only nearly catastrophic process is bremsstrahlung, which has been shown to be unimportant at most energies.

The general equation describing the physical conditions outlined above may be written in the form (Berkey and Shen, 1969)

$$\frac{\partial u_e}{\partial t} + \frac{\partial}{\partial \gamma_e}\left\{\left[\frac{d\gamma_e}{dt} u_e\right] - \frac{1}{2}\frac{\partial}{\partial \gamma_e}\left[\frac{d}{dt}\left(\langle \Delta \gamma_e^2 \rangle\right) u_e\right]\right\} \qquad \text{n} \quad 3.5$$

$$+ \nabla \cdot \left(-D \cdot \nabla u_e + \underline{V}_d u_e\right) = q_e(\gamma_e, \underline{X})$$

The quantity $q_e(\gamma_e, \underline{X})$ on the right hand side is the electron source (injection) spectrum. Note that $q_e \, d\gamma_e \, d^3x$ represents the number of electrons within $d\gamma_e$ and d^3x per unit time. (The contributions to q_e from galactic secondary production in the interstellar space were discussed in Chapter II.) The usual assumption of steady-state conditions is accomplished by setting $\frac{\partial u_e}{\partial t} = 0$. In general, both D_{ij} and $\underline{V}_d$ are functions of position. D_{ij} may also depend on γ_e (or more precisely, the particle rigidity).

The second term in the braces describes statistical energy fluctuations experienced by the particles in diffusing through energy space. This sort of expression is characteristic of Fokker-Planck equations (Chandrasekhar, 1943). Most treatments of galactic electron propagation, however, assume that such effects may be neglected in comparison with the term containing the energy loss rate $\frac{d\gamma_e}{dt}$. It is also worth pointing out that $\frac{d\gamma_e}{dt}$ is usually assumed to be determined solely by loss mechanisms and not by quasi-continuous interstellar acceleration processes of the type proposed by Fermi (1949).

Hence equation 3.5 can already be reduced to the form

$$\frac{\partial}{\partial \gamma_e}\left[\frac{d\gamma_e}{dt} u_e\right] + \nabla \cdot \left(-D \cdot \nabla u_e + \underline{V}_d u_e\right) = q_e(\gamma_e, \underline{X}) \qquad 3.6$$

The controversies mentioned in the introduction generally arise in the handling of the diffusive-convective term. Most treatments in the literature prior to 1968 (see references quoted in Jokipii and Meyer, 1968) employ the leakage lifetime approximation, which amounts to the replacement of this entire term by the quantity $\frac{u_e}{\tau_e}$. Here τ_e is to be regarded as the mean residence time for the trapped electrons gradually escaping from the galaxy. Most of the early authors following this approach argued that τ_e may be considered essentially independent of energy over a very wide range in the electron spectrum, typically about 10^8-10^{14} eV. They also usually assumed a uniform distribution of sources throughout the galactic disk, so that the transport equation took the simple form

$$\frac{\partial}{\partial r_e}\left[\frac{dr_e}{dt}u_e\right] + \frac{u_e}{\tau_e} = q_e(r_e) \qquad 3.7$$

This procedure rests on an analogy between the residence time and the collision loss lifetimes usually included in the transport equations for nucleonic particles. (A similar lifetime parameter would be appropriate for the description of electron bremsstrahlung losses, but the mean free path of about 60 g cm^{-2} for such collisions greatly exceeds the known average distance of 3-4 g cm^{-2} traversed by cosmic rays.) Thus particle losses by diffusive or convective leakage are considered physically equivalent to catastropic collision losses. Serious objections to this assumption have been made by Jokipii and Meyer (1968) and more recently by Berkey and Shen (1969) and by Jones (1970). Their key argument is that particle collisions can be characterized by a uniform probability of occurrence j per unit time, while the probability of leakage depends both on the particle energies and their distances from the boundary of the storage region.

The validity of the leakage lifetime approximation may be tested to some extent by the search for an increase in the spectral index characterizing the observed electron flux. For a source spectrum obeying a power law, $q_e = K\gamma_e^{-\Gamma}$, the solution of equation 3.7 has the limiting forms

$$u_e(\gamma_e) = \tau_e K \gamma_e^{-\Gamma}, \quad \gamma_e \ll (b\tau_e)^{-1} \qquad 3.8a$$

$$u_e(\gamma_e) = \frac{K}{b(\Gamma-1)} \gamma_e^{-(\Gamma+1)}, \quad \gamma_e \gg (b\tau_e)^{-1} \qquad 3.8b$$

if $\frac{d\gamma_e}{dt}$ is assumed to have the form $-b\gamma_e^2$. (In the same context Ramaty and Lingenfelter (1968) have considered the more general case $-\frac{d\gamma_e}{dt} = I + b\gamma_e^2$ to include the effects of ionization at lower energies.) Hence the theory predicts an increase by one power in the equilibroum spectral index at energies greatly exceeding the critical value $\gamma_c = (b\tau_e)^{-1}$. Several authors have described this behavior as a break in the electron spectrum, although the term is misleading in the sense that the transition may span more than one decade in energy (Jones, 1970).

Current observational results have not revealed any well-defined increase in the spectral index at energies ranging up to about 300 GeV (see for example the contributions in the Thirteenth International Cosmic Ray Conference, Vol. 1, pp 346-371). Although the data are not yet conclusive, it seems likely that at least some modification of the leakage lifetime approach must be considered.

Perhaps the least drastic approach consists in allowing an energy dependence for τ_e . Silverberg and Ramaty (1973) have recently shown that the total increment $\Delta\Gamma$ in the spectral index is less than unity if τ_e is assumed to be a decreasing function of energy. This assump-

tion appears to bring the solutions of equation 3.7 into qualitative agreement with the data, although the chosen dependence for τ_e is somewhat arbitrary at present.

Unfortunately the prediction of spectral increases does not provide a completely unambiguous test of models described by equation 3.7. Since the change in the spectral index is due to the energy loss processes, it is not surprising that recent treatments which abandon the leakage lifetime approach also predict increases in Γ with energy. Jokipii and Meyer (1968) have considered an isotropic diffusion model in which equation 3.6 is simplified to the form

$$\frac{\partial}{\partial \gamma_e}\left[\frac{d\gamma_e}{dt} u_e\right] - D_0 \nabla^2 u_e = q_e(\gamma_e, \underline{x}) \qquad 3.9$$

The electron sources are assumed to be uniformly distributed throughout a disk of radius R_D and thickness $2L$, while the diffusive region is of infinite extent (corresponding to an infinite leakage lifetime). In this model the equilibrium spectrum is marked by two increases in Γ by one-half power each, occurring at energies $\gamma_c^{(1)} = \frac{4D_0}{bL^2}$ and $\gamma_c^{(2)} = \frac{R_D^2}{L^2}\gamma_c^{(1)}$. A paper by Dogel and Syrovatskii (1969) presents essentially the same results for a similar model in which the source region is changed from a cylindrical section to a flattened ellipsoid and the infinite diffusing region is replaced by a spherical halo of radius $R_H \sim R_D$. Their results bear out the suggestion by Berkey and Shen (1969) and by Jones (1970) that the structure of the source region is of much greater importance than the extent of the confinement volume.

Berkey and Shen (1969) further confirm the above results for the isotropic diffusion approximation. Their paper discusses the possible effects of the boundaries of the diffusing region on the spectral changes. They

also consider a convection-diffusion model in which the magnetic field lines are allowed to expand outward in directions normal to the galactic plane. The scattering centers are thus assigned normal drift velocities $V_d(z)$, a condition which roughly coincides with the inflation of magnetic field loops in the galactic model suggested by Parker (1966). The diffusion coefficient is assumed uniform and nonzero only in directions parallel to the field lines. Hence the transport equation in this model has the form

$$-\frac{\partial}{\partial \gamma_e}\left[b\gamma_e^2 u_e\right] + \frac{\partial}{\partial z}\left(V_d(z)\,u_e\right) - D_{11}\left(\frac{\partial^2 u_e}{\partial x^2} + \frac{\partial^2 u_e}{\partial y^2}\right) = q_e(\gamma_e, \underline{x}) \qquad 3.10$$

This treatment essentially permits a return to the leakage lifetime approximation, since convective motion into the halo region may be characterized by a time τ_c much shorter than that for diffusive motion over distances comparable to the galactic radius. Thus the model predicts a unit increase in Γ centered on the energy $(b\tau_c)^{-1}$.

However, Berkey and Shen (1969) point out inadequacies in models of this type which assume a uniform distribution of sources in the galactic disk in accounting for all the observed features of the electron flux (spectral shape, positron fraction, background radiation). They suggest that a more realistic calculation must provide for a higher concentration of electron sources near the galactic center region. However, one of their arguments, based on the distribution of diffuse galactic gamma radiation and its interpretation in terms of Compton scattering of electrons from an infrared background (of energy density 13 eV cm^{-3}) must now be discredited. A higher concentration of sources at the galactic center has also been proposed by Longair and Sunyaev (1969). These authors have attempted to explain the gamma ray emission from the center region as the

result of Compton scattering of infrared photons by energetic electrons, both of which are produced in intense, compact central sources.

CHAPTER IV

SOLAR MODULATION OF GALACTIC ELECTRONS

In addition to sporadic bursts of energetic solar cosmic rays, the sun ejects a continuous flow of ionized hydrogen which is generally referred to as the solar wind. The term was originally suggested by Parker (1958) to emphasize the fluid behavior of this corpuscular radiation, which is due to a hydrodynamic expansion of the outer coronal regions. The approximately radial streaming velocity $\underline{V}(\underline{x})$ of the solar wind is about 400 km sec^{-1} near the earth during solar quiet periods, although $\underline{V}$ can briefly exceed 1000 km sec^{-1} during the flare events in which solar cosmic rays may be ejected with energies above several MeV per nucleon.

Under normal conditions the average energies of solar wind particles lie within the kilovolt range, and the particle density (which decreases with the square of the heliocentric distance r) does not exceed about 20 cm^{-3} near the earth. Hence collisions of particles in the wind with each other or with galactic cosmic rays are infrequent. Because of the high conductivity of the gas, however, the magnetic field lines extending from the corona remain frozen into the solar wind as it expands outward past the orbit of the earth. Spatial irregularities or kinks in the field lines, carried along at about the velocity $\underline{V}$, strongly scatter galactic cosmic rays entering the solar system. As a result, galactic particles over a broad range of rigidities extending up to several GV are coupled to the expanding wind and convected out of a heliocentric

region which may extend more than 50 astronomical units (AU) beyond the orbit of the earth.

The efficiency with which galactic cosmic rays are swept from the inner solar system is known to vary considerably over periods that generally coincide with the eleven-year sunspot cycle. It seems likely that the effective size of the modulating region (which is often referred to as the solar cavity) may vary over the same time scale. This changing behavior of the solar wind and its effects on cosmic ray protons, heavier nuclei, and electrons have become the objects of intensive research during the past decade.

A comprehensive discussion of the rapidly accumulating observations and the development of the theory of solar modulation lies well beyond the scope of this chapter. The following sections are intended only to outline the theoretical framework available for estimating the effects of solar modulation on galactic electrons between about 50 MeV and 10 GeV. The discussion will also indicate the severe limitations of the present theory, which are for the most part due to an insufficient knowledge of spatial and temporal variations in the interplanetary magnetic field. In fact, detailed agreement with observations has generally required the use of ad hoc assumptions concerning these poorly known quantities.

A better understanding of the solar wind parameters may result from the recent accumulation of data over several portions of the solar cycle. Repeated measurements by several investigators (see for example Schmidt, 1972; Burger and Swanenburg, 1972; Webber et al., 1973; Fulks et al., 1973) have already revealed interesting features in the varying (total) electron intensities below 1-10 GeV between 1965 (at solar minimum) and

1972. Unfortunately, data describing the temporal behavior of the separate negatron and positron spectra is extremely meager (Cummings et al., 1973a).

It is reasonable to expect that continuing observations of this portion of the electron spectrum, obtained from balloons or satellites, can indeed provide important constraints for the theory of solar modulation. From this point of view, measurements of the electronic charge ratio at these energies may be of particular importance. Since the galactic positron component may result entirely from interstellar nucleonic collisions, the interstellar positron spectrum can be predicted using the known spectra of energetic protons and helium nuclei (above the regimes where these spectra are themselves distorted by solar modulation). Such estimates of galactic secondary negatron and positron spectra obtained by several authors were discussed in Chapter II. Comparisons of the predicted positron spectrum with observations may provide information on the mean energy losses suffered at different times by galactic cosmic rays in the expanding solar wind, the degree of residual modulation at solar minimum, and other questions of current interest.

In terms of the present experiment, it is especially important to note that estimates of interplanetary energy losses by electrons can be obtained directly from measurements of their charge ratio at different energies (Cummings et al., 1973a). This possibility is in fact quite significant, since an accurate determination of the positive fraction is considerably easier (from balloon-borne experiments in particular) then measurements of the absolute positron and negatron spectra.

A. The Diffusion-Convection Model

The solar modulation of galactic cosmic rays was first interpreted within the context of the diffusion-convection model suggested by Parker (1965). In this picture the magnetic irregularities superimposed on the interplanetary field lines move outward at the solar wind velocity $\underline{V}(\underline{x},t)$. In their local rest frames the irregularities are assumed to act as nearly isotropic, elastic scattering centers for cosmic rays gyrating in the average field. Because of the expansion of the wind, the particles tend to be convected out of the solar cavity. However, quasi-steady state conditions hold for the cosmic ray densities within interplanetary space if the rate of outward convection is balanced by the rate of inward particle diffusion through the scattering centers. The equation describing this condition is obtained by setting each term in the particle continuity equation equal to zero:

$$\frac{\partial}{\partial t} u(\underline{x},T,t) \simeq \nabla \cdot [\underline{\underline{\kappa}}(\underline{x},\rho,t) \nabla u - \underline{V}(\underline{x},t) u] \simeq 0 \qquad 4.1$$

Here $u(\underline{x},T,t)$ is the differential particle density describing a given cosmic ray species, expressed for later convenience in terms of the kinetic energy T instead of the Lorentz factor γ as in the previous chapters. The quantity $\rho \equiv \frac{pc}{Ze}$ (where p is the momentum) is the particle rigidity. The current in equation 4.1 consists of the inwardly diffusing flux, determined by an effective diffusion tensor $\kappa_{ij}(\underline{x},\rho,t)$, and the convective flux $\underline{V}(\underline{x},t)u(\underline{x},T,t)$.

With the assumptions of purely isotropic scattering ($\kappa_{ij} = \kappa \delta_{ij}$) and heliocentric radial symmetry, the solution of equation 4.1 may be written as

$$u(r,T,t) \simeq u(\infty,T)\exp\left[-\int_{r}^{r_b(t)} dr\ \frac{V(r,t)}{K(r,\rho,t)}\right] \qquad 4.2$$

The quantity $u(\infty,T)$ may be considered the differential particle density in the interstellar medium, while $r_b(t)$ is the postulated boundary of the modulating region. The argument of the exponential is often referred to as the modulation potential $\eta(t)$. In this approximation the product $\frac{\tilde{r}\,\tilde{V}}{\tilde{K}}$ (where the tilde denotes characteristic values over regions of interest) provides a rough estimate of the degree of solar modulation at time t. In principle the time dependence of the modulation, including the eleven-year cyclic variation, may be due to changes in any combination of the quantities V, K, and r_b.

B. Adiabatic Energy Losses

The non-zero divergence of the streaming velocity $\underline{V}(\underline{x},t)$ associated with the expansion of the solar wind has an additional physical implication which does not appear in equation 4.1. Parker (1965) noted that cosmic rays subject to convection and diffusion must also experience adiabatic energy losses, since the magnetic field in which they propagate expands with the radially diverging solar wind. The rate of change of the particle momentum is given by the expression

$$\frac{1}{p}\frac{dp}{dt} = -\frac{1}{3}\nabla\cdot\underline{V} \qquad 4.3$$

In terms of the kinetic energy, this relation becomes

$$\frac{1}{T}\frac{dT}{dt} = -\frac{1}{3}\alpha(T)\nabla\cdot\underline{V}, \quad \alpha(T) \equiv \frac{T+2mc^2}{T+mc^2} \qquad 4.4$$

To include the effect of these energy losses, equation 4.1 must be replaced by a more general Fokker-Planck equation of the form

$$\frac{\partial u}{\partial t} \simeq 0 \simeq \nabla\cdot\left[\underline{\underline{\kappa}}\nabla u - \underline{V}u\right] + \frac{1}{3}\left[(\nabla\cdot\underline{V})\frac{\partial}{\partial T}\left(\alpha(T)\,T\,u\right)\right] \qquad 4.5$$

The expression for the particle current density $\underline{S}(\underline{x},T,t)$ is then given by

$$\underline{S} = \underline{V}u - \underline{\underline{\kappa}}\nabla u - \frac{1}{3}\underline{V}\frac{\partial}{\partial T}\left(\alpha(T)\,T\,u\right) \qquad 4.6$$

Derivations of equations 4.5 and 4.6 have been presented by Gleeson and Axford (1967), and by Jokipii and Parker (1970). In the latter treatment, equation 4.5 is first derived as a Fokker-Planck equation for the differential particle density in the local rest frame of the solar wind. Then it is shown that the form of equation 4.5 remains approximately invariant under the transformation to a heliocentric rest frame. The earlier

derivation by Gleeson and Axford (1967) is valid under the assumptions of spherical symmetry and isotropic diffusion. Their starting point is a Boltzmann equation with a collision term describing isotropic scattering in the frame moving with the solar wind.

To obtain physically interesting solutions of equation 4.5 it is necessary to have reasonable values for the two solar wind parameters $V(\underline{x},t)$ and $K_{ij}(\underline{x},\rho,t)$. The velocity $\underline{V}$ appears to cause no serious problems, since present theories of the interaction between the solar wind and the interstellar medium (Parker, 1963) predict that $\underline{V}$ remains approximately constant to a radial distance of perhaps 50 AU. This expectation is partially borne out by recent observations from the Pioneer 10 interplanetary probe, which reveal at most only a slight decrease in the solar wind speed between the orbits of the earth and Jupiter. Hence in the context of other uncertainties, $\underline{V}$ may be safely replaced in equation 4.5 by its average value near the earth.

The diffusion tensor K_{ij} is a more complex quantity involving strongly time-dependent properties of the solar wind as well as the rigidities of the scattered particles. Several forms for K_{ij} have been suggested in the literature to describe qualitative features of modulated spectra, but the scarcity of observations over most of the solar cavity has prevented any general agreement concerning the dependence of K_{ij} on physical parameters. A number of investigators have attempted to relate the behavior of K_{ij} directly to the fluctuations of the interplanetary magnetic field and particle rigidities (see for example Jokipii, 1966; Hasselmann and Wibberenz, 1968; Klimas and Sandri, 1973; Jones et al., 1973). However, the assumptions and conclusions of these authors are still subject to controversies which lie beyond the scope of this discussion.

C. Solutions of the Spherically Symmetric Transport Equation

The task of solving equation 4.5 is in general quite formidable. An almost standard simplification of the problem is that of assuming a spherically symmetric solar wind. In this approximation, equation 4.5 a assumes the form

$$\frac{\partial u}{\partial t} = 0 = \frac{1}{r^2}\frac{\partial}{\partial r}\left(r^2 K_{rr}\frac{\partial u}{\partial r}\right) + \frac{2V(r)}{3r}\frac{\partial}{\partial T}(\alpha T u) - \frac{1}{r}\frac{\partial}{\partial r}(r^2 V u) \qquad 4.7$$

The diffusion coefficient is now given as $K_{rr} = K_{\parallel}\cos^2\psi + K_{\perp}\sin^2\psi$, where ψ is the angle between the average magnetic field and the heliocentric radius vector. Thus the distortion of the interplanetary field lines into an Archimedean spiral pattern by the rotation of the sun may still be considered in evaluating K_{rr}. However, it is possible to neglect even this departure from radial symmetry if $K_{\parallel} >> K_{\perp}$. Hence an isotropic diffusion coefficient $K(r,\rho,t)$ often is substituted for K_{rr}.

Even with mathematically convenient forms for the diffusion coefficient, the analytic solutions satisfying appropriate boundary conditions are usually more complex than the simple diffusion-convection solution 4.2. However, in the limit of weak modulation a derivation valid to first order in $\frac{\tilde{r}\tilde{V}}{K}$ yields the simple result

$$u(r,T,t) \simeq u(\infty,T)\left[1 - C(\infty,T,t)\eta(t)\right] \qquad 4.8$$

where $C(r,T,t) = 1 - \frac{1}{3u}\frac{\partial}{\partial T}(\alpha T u)$ and $\eta = \int_r^{r_b(t)} dr\, \frac{V(r,t)}{K(r,\rho,t)}$

The quantity C is known as the Compton-Getting coefficient, since it is identical to the transformation coefficient relating the values of the

differential current density S between reference frames in uniform relative motion (Compton and Getting, 1935).

The weak modulation condition $\frac{\tilde{r}\tilde{V}}{\tilde{R}} << 1$ is generally violated for rigidities below 1 GeV. However, another analytic method developed by Gleeson and Axford (1968) appears to be valid under a somewhat less restrictive statement of weak modulation conditions. The fundamental assumption in their approach, which is known as the force-field approximation, is that the radial current density S (given by equation 4.6) may be neglected at high rigidities. This condition leads to the result that the intensity $\mathcal{J}(r,E,t)$ at a radial distance r and total energy E may be found from the relation

$$\frac{\mathcal{J}(r,E,t)}{E^2-(mc^2)^2} = \frac{\mathcal{J}(\infty,E+\Phi)}{(E+\Phi)^2-(mc^2)^2} \qquad 4.9$$

where Φ is a quantity depending in general on E, r, and t.

Fisk et al. (1973a) have shown that a useful condition for the validity of the force-field approximation may be expressed as

$$\left| \frac{\tilde{C}}{2}(\tilde{C}-1)\frac{\tilde{V}\tilde{r}}{\tilde{R}} \right| << 1 \qquad 4.10$$

where C is the Compton-Getting coefficient and the tilde again implies the use of characteristic values. Schmidt (1972) has investigated the usefulness of the force field model in describing the modulation of galactic electrons between 20 MeV and 15 GeV.

In the general case, it is necessary to emply numerical solutions to equation 4.7. The final chapter of the present work makes use of methods developed by Fisk (1971) to compare the modulation of assumed interstellar

(total) electron and positron spectra with the intensities measured in this experiment between 50 and 800 MeV. For a discussion of the assumptions made about the form of the diffusion coefficient and other parameters in equation 4.7, see Section A of Chapter VII.

CHAPTER V

THE DETECTOR

A brief description of the magnetic spectrometer used in the present experiment (shown schematically in Figure 1.3) was provided in Chapter I. The following sections describe each of the detector elements and point out in greater detail the features most critical to the performance of an experiment of this type. The fast telescope electronics, the gas Cerenkov counter, and the shower counters receive particular attention. The available calibration data on the Cerenkov counter detection efficiency and the shower counter pulse height distributions for incident electron beams have been included in the appropriate sections. Brief descriptions of the spark chambers and the magnetic core readout system are also included, and a recent technique for reducing the readout (dead) time following event trigger pulses is discussed.

A. Telescope Geometry

All of the four telescope scintillators are rectangular sheets of Pilot M plastic hydrocarbon material. The two coincidence scintillators, S1 and S2, are mounted on the outside surfaces of the upper and lower bulkheads which separate them and their respective phototubes from the spark chamber volume. Both S1 and S2 are solid sheets, 25.4 cm square and .475 cm thick. In order to reduce the amount of material encountered by incident particles, the thickness of the aluminum alloy bulkhead has been reduced to .051 cm over the area of contact with these scintillators.

The two anticoincidence scintillators, A1 and A2, are situated just above and below the magnet gap. Both of these counters are rectangular sheets, 27.9 cm x 25.4 cm x .475 cm, having rectangular holes of dimensions 15.2 cm x 8.0 cm in their centers. The hole size has been chosen small enough so that high-rigidity particle trajectories satisfying the scintillator coincidence criterion $S1 \cdot \overline{A1} \cdot \overline{A2} \cdot S2$ cannot graze the magnet pole faces.

All of the telescope scintillators are viewed by RCA 8575 phototubes, which have 12 stages and a 5-cm photocathode diameter. S1 and S2 are provided with one tube apiece, while A1 and A2 are each viewed through plastic light pipes by a pair of tubes mounted on the outside surface of the nearer bulkhead. One Velonex PP-8 high voltage supply is mounted on each bulkhead to operate the two sets of three tubes.

The center-to-center vertical distance between S1(2) and A1(2) is 34.1 cm. The magnet gap region separating the centers of A1 and A2 has a depth of 15.9 cm. These numbers and the scintillator dimensions have been used in a Monte Carlo calculation which simulates an isotropic distribution of particles at given rigidities impinging on the telescope counter system. In the high-rigidity limit the estimated value of the geometric factor, based on a sample of 2×10^4 incident particles, is 18.8 ± 0.6 cm^2 sr. This value is appropriate for particles above 50 MV (corresponding to an average angular deflection of about 8.6 degrees).

B. Gas Cerenkov Counter

1. Function

The first detector telescope element encountered by acceptable incident particles is the gas Cerenkov counter (C). The positions of the Cerenkov counter mirrors and phototubes within the gas pressure vessel are shown in Figure 1.3. The upper portion of the pressure vessel was fashioned from a spun aluminum dome having an inside radius of 38.1 cm and a wall thickness of .229 cm. The gas volume extends down to the upper spark chamber bulkhead, where the two tilted plane mirrors reflect Cerenkov light into a pair of 23-cm diameter Amperex 60DVP phototubes. Each tube is provided with a separate Velonex PP-8 power supply and a fast preamp mounted near the tube socket.

The mirrors are made of aluminized .076-cm thick plexiglas, and are supported only along their edges by the mounting frame. Their normal directions are inclined at an angle of 30 degrees to the vertical axis.

As a telescope element the Cerenkov counter performs two distinct functions. Placing it in coincidence with the scintillators S1 and S2 insures that only downward moving particles can trigger the spark chamber system. However, it also has the critical role of preventing triggers by the large flux of protons below the threshold energy for emitting Cerenkov radiation. The dependence of the threshold Lorentz factor on the quantity $\eta = n - 1$ (where n is the index of refraction of the medium) is given by the condition $\gamma_c \simeq (\sqrt{2\eta})^{-1}$. The value of η at STP for several gases commonly used in Cerenkov counters and the corresponding threshold Lorentz factors are shown in Table 5.1. The choice of carbon dioxide

for the initial flights of the detector insured that only those protons with energies above 31.3 GeV could cause a true coincidence trigger pulse. The corresponding threshold energy for the detection of electrons is 17 MeV.

TABLE 5.1

CERENKOV COUNTER GASES

Medium	η	Threshold Lorentz Factor γ_c
Carbon Dioxide	.00045	33.3
Freon-12 (CCl_2F_2)	.00113	21.0
Sulfur Hexafluoride	.00080	25.0
Air	.00029	41.5

The selection of carbon dioxide was based on its apparently satisfactory efficiency as a Cerenkov radiator (discussed in Appendix A), its high value of γ_c, its availability, and its convenience in handling. Of the gases with higher values of η, sulfur hexafluoride has been found to cause serious degradation in spark gas mixtures, even when present in extremely small quantities (Thompson, 1973). The problem is due to an unusually high rate of electron attachment in sulfur hexafluoride molecules, which rapidly absorb particle ionization trails. No such tendencies are exhibited by Freon-12, whose comparable value of γ_c and greater light-producing efficiency have prompted the use of this gas instead of carbon dioxide in later flights.

2. Detection Efficiency

The Monte Carlo program used to estimate the geometric factor of the instrument also incorporates subroutines which evaluate the per-

formance of the Cerenkov counter for a given medium. The program simulates the production of photons in the gas by each incoming particle, their reflection (or absorption) at the mirror surfaces, and the eventual production of photoelectrons in the tube photocathodes. The calculation provides spatial distributions of photons incident on the tube faces and histograms of the numbers of cathode photoelectrons generated by incident particles at a given Lorentz factor.

In addition to its usefulness in optimizing the placement of the phototubes in the telescope geometry, the calculation serves as the basis for an analysis of the Cerenkov counter detection efficiency for electrons at various energies. An outline of this analysis is given in Appendix A.

Direct measurements of the detection efficiency have been made at energies between 20 MeV and 140 MeV by exposing the detector to a negatron beam from a 180 MeV electron synchrotron at the National Bureau of Standards, Washington, D. C. For these calibration runs an external beam counter (B) replaced the detector telescope scintillator S1, as shown in Figure 5.1. B was a small rectangular plastic scintillator (about 3 x 4 cm^2) viewed by a single phototube and placed in the beam path about 10 cm in front of the detector. The distance between the window of the beam pipe and counter B was about 40 cm. Both the spark chambers and the shower counters were active throughout each beam exposure period. The trigger pulses were generated by the five-fold coincidence condition $C \cdot B \cdot \overline{A1} \cdot \overline{A2} \cdot S2$.

A lead-glass Cerenkov counter was used to set an upper limit of 30 percent on the FWHM of the intrinsic distribution of beam energies between 50 MeV and 140 MeV. However, it is likely that the true value

is as low as 10 percent. In either case, the effect of the finite beam energy dispersion on the analysis of the detection efficiency has been shown to be negligible. (The effect on estimates of the rigidity resolution of the detector is discussed in Section D.2 of Chapter VI.)

The axis of the instrument was inclined at an angle of about 10 degrees to the horizontal beam direction, so that any time only one Cerenkov counter phototube (C1 or C2) was exposed to the reflected Cerenkov light. Reversing the tilt to expose each tube in turn to a beam of 94-MeV electrons revealed no significant differences in the measured detection efficiencies. All subsequent runs were made with only C2 receiving light.

For the initial beam exposures, the pressure vessel was filled with carbon dioxide at 1 atm. Later runs were made with air and Freon-12, also at 1 atm. The Freon was introduced by removing the hemispherical cap from the upper (C2) phototube housing and flowing the gas through the loosened base of the pressure vessel for about 30 minutes. The amount of air contamination is difficult to estimate directly with reliability, but a comparison of the predicted and measured detection efficiencies (see Figure 5.3 and Appendix A) indicates that the effective index of refraction of the gas was only about 1.00048. This value would imply that the Freon partial pressure was only 0.2 atm., which is somewhat lower than the fraction expected.

For a monoenergetic electron beam the Cerenkov counter detection efficiency is given by the ratio of the number of five-fold coincidence triggers to the four-fold scintillator coincidence counts ($B \cdot \overline{A1} \cdot \overline{A2} \cdot S2$). The values obtained at energies up to 140 MeV for carbon dioxide and air have been plotted in Figure 5.2, while Figure 5.3 shows the corre-

sponding points for the mixture of Freon-12 and air. It is evident that the energy dependence of the measured efficiency for carbon dioxide differs significantly from the other two gases. The predicted efficiency curves for carbon dioxide and air, based on the analysis described in Appendix A, suggest that one or more systematic errors were responsible for the low apparent efficiencies with carbon dioxide (which preceded the runs with air and Freon-12). Since the values for air are in reasonable agreement with the predicted curve for an assumed C2 discriminator threshold of 4-5 cathode photoelectrons, the possibility of contamination by an anomalous low-energy tail in the beam distribution does not seem likely. An adjustment in the detector alignment, which was made after the carbon dioxide runs and prior to the other exposures, may at least partially account for the discrepancy.

An independent test of the predicted and measured efficiencies has been provided by an accidental leak in the Cerenkov counter pressure vessel during the first successful flight of the instrument (see Chapter VI). Since the dependence of the efficiency on electron energies determines its behavior with changes in the gas density, both the estimated and the measured efficiency curves may be used in deriving the atmospheric depth dependence of the electron intensities (to be discussed in Section F of Chapter VI). Examples of the intensity growth curves for the two flights of the detector which reached float altitudes have been shown for comparison in Figure 5.4. Although low temperatures resulted in a loss of float data from the second flight, in both cases the detector was working normally at atmospheric depths greater than about 10-15 g cm^{-2}. Above these limits the growth curves agree within about 20 percent (which is consistent with the statistical uncertainties)

if the predicted efficiencies are adopted, while use of the measured values introduces a discrepancy of nearly a factor of two.

Since no further calibration data is presently obtainable, the efficiency curve assumed for the flight data analysis is that given by the predicted values for carbon dioxide (based on the same assumptions which best fit the observed values for air).

C. Coincidence Logic Electronics

The analysis of the Cerenkov counter performance demonstrates that the two Cerenkov phototube discriminators must be operated at a relatively low threshold. This requirement, which implies correspondingly high rates from the C1 and C2 discriminator outputs, has been the primary motivation in using a fast telescope coincidence system.

A block diagram of the telescope system electronics is shown in Figure 5.5. The two C-tube anode signals are each sent through fast preamplifiers before being added in a summing discriminator. The signal from the scintillator tubes is sufficient to allow omission of the preamplifier.

All the discriminators and coincidence circuits in the system have negative output levels of approximately 400 MV. The rise and fall times of the logic pulses are on the order of 2 ns. The discriminators which accept the single tube (anode) signals from C1, C2, S1, and S2 have output pulse widths of about 25 ns. Both discriminators receiving the summed outputs from the two pairs of anticoincidence tubes have wider output pulses of about 50 ns. The thresholds for all the counters have been individually adjusted to an amplitude of about one-third the minimum ionizing peak for single particles.

All the coincidence logic circuitry has been installed in five modules mounted in a standard NIM bin, which is located in the pressure vessel beneath the lower spark chamber. Two modules each contain three discriminators, one circuit being left unused. The output of the main coincidence module is sent to one of eight shaper driver circuits, contained in a single module, which converts the negative telescope logic signals into positive five-volt levels. The particular shaper

driver receiving the main coincidence signal generates the spark chamber trigger and START SCAN pulse for the readout electronics. It also provides a rate output for the telemetry housekeeping.

The fifth module in the telescope package contains two additional coincidence circuits. The first has two YES and two NO inputs and monitors the scintillator coincidence rate $S1 \cdot \overline{A1} \cdot \overline{A2} \cdot S2$. The second has only two YES inputs and is used to observe the $C \cdot S1$ rate. These two auxiliary coincidence signals and the five discriminator outputs are sent to the seven remaining shaper driver circuits, which provide rate outputs for the telemetry package.

D. Spark Chamber System

1. Configuration

The basic functional unit in the spark chamber system is the grid module. Each module is a glass-bonded mica frame supporting two orthogonal grids of .01-cm diameter beryllium-copper wires. There are 200 parallel wires spaced 1.27 mm apart in each grid plane, so that the overlapping area of the two grids is 25.4 cm x 25.4 cm. The spacing between the grids, which lie on opposite sides of the module frame, is 4.17 mm. One side of each grid is clamped beneath a mica strip bonded to the frame. On the opposite side of the frame each wire is threaded through one of the 200 ferrite cores mounted along the core shelf or array. The ends of the wires are then soldered to a buss at the outer edge of the array. The layout of the core shelf is shown in Figure 5.6. Each core is also threaded by one of 8 parallel sense wires running along the array, as well as one of 25 current drive wires which loop through groups of 8 cores. The functions of the sense lines and drive wires in reading out the core memory are discussed in section D.3.

In the present spark chamber system stacks of modules are operated in a helium-neon gas environment at one atmosphere. When a negative high voltage pulse is applied to the grid buss on one array of each module, any localized spark breakdown between the grids initiates a current flow in the nearest grid wires which sets cores in each of the two arrays. The core locations give the x and y coordinates of the spark event. If the high voltage pulse is applied within about 500 ns after a charged particle traverses the grids, its residual ionization trail can produce a series of localized spark breakdowns in the module stacks. The corresponding set core locations record the particle trajectory through the chamber.

The exact gas mixture used in the present detector contains 98.5% commercially available helium-neon gas (containing 10 parts helium and 90 parts neon), 1.0% argon, and 0.5% alcohol, all by partial pressures. The ratios were arrived at during development of previous spark chamber detectors at NASA/Goddard Space Flight Center and have by now become somewhat standardized. A discussion of the early spark module development which includes a study of spark gas mixtures, has been given by Kniffen (1969).

In the present detector 16 identical grid modules have been stacked to form two distant spark chambers, lying above and below the magnet housing respectively. The combined memory of the upper and lower chambers consists of 6400 cores. As shown in Figure 1.3 each spark chamber is subdivided into stacks, or tiers, of four decks each. The spacing between two modules in a tier is 1.6 cm. The heights of the modules closest to the z = 0 plane (at the center of the magnet) in each tier are $\pm$9.5 cm and $\pm$35.3 cm.

2. High Voltage Pulsers

Each spark chamber is equipped with one high voltage pulser unit which delivers negative 2.5 kv pulses to the eight modules comprising both tiers. The circuits used are essentially identical to earlier versions described by Kniffen (1969). The trigger input from the telescope electronics activates an avalanche transistor circuit which in turn fires two pairs of EG&G KN-2 Krytron pulsers. A single Krytron drives two modules, each pair being mounted on a circuit board near its corresponding tier.

The total delay time between event trigger and spark formation is about 300 ns. Of this value, 50 ns is spent in the Krytron pulser and another 50 ns in spark formation from the initial ionization trails.

The pulser units are, of course, hermetically sealed from the spark gas in the chambers. The high voltage and return outputs, as well as the input power and trigger leads, are routed through glass feedthrough connectors. During operation the units may be filled with nitrogen for greater protection against internal discharges, but this precaution has so far proved unnecessary for the present detector.

Series resistors of 27 ohms have been inserted between the negative high voltage outputs and the high voltage buss on each module. They serve to limit the peak spark current, and their values might be individually changed to adjust the peak voltage on any grid. Increasing this resistance is a possible method of reducing spurious edge sparking on some grids. The ground side of the pulser output is tied directly to the buss on the orthogonal array of the same module. However, the high voltage ground is isolated from circuit (battery) ground by 1000 ohms.

The pulser unit itself is completely isolated from chassis ground by plastic spacers. These precautions are necessary to prevent the high voltage pulses from introducing noise into other electronic systems in the detector (including the shower counter pulse height analyzers).

3. Core Memory Readout

Figure 5.7 indicates the module interconnections necessary for readout of the core memory. The sets of eight sense lines running along the core shelves are all linked to form an unbroken path connecting the arrays of every module in one chamber. Furthermore, one end of each drive wire on every array is tied to one of 25 vertical buss wires connecting different grids in the stacks. As shown in Figure 5.6, the opposite ends of the drive wires lead through isolation diodes to a ground buss on each core shelf.

The 25 vertical busses tied to each array deliver the current pulses which reset cores after a spark event. These pulses are generated by 25 independent circuits in a package mounted near each spark chamber. In addition, the ground buss for the drive wires on each array is connected to one of 16 current sinks (grounding circuits) contained in the same package. During a readout cycle all the possible pairs of current pulsers and grounding circuits are gated in sequential order to reset groups of eight cores at a time throughout the two chambers. Every core whose state is actually reversed induces a current pulse through the particular sense wire which threads it. A set of eight sense amplifiers in the same package sends the data from each group of reset cores to an eight-bit shift register. (After each current pulse the sense line data is read out serially by the core memory readout system, contained in the lower electronics package.) The simultaneous identification of a given current pulser line, grounding buss, and sense line uniquely determines the location of a single core within the spark chamber configuration.

The process of resetting all the cores and identifying those cores set by a spark event is controlled by the scan electronics package. This system is contained in a NIM module and mounted in the same bin provided for the five telescope system modules. It has the twofold function of enabling the combinations of current pulsers and grounding circuits to reset cores and of accepting data on set core locations for telemetry readout.

When triggered by a START SCAN pulse from the telescope electronics, the readout package first inhibits the telescope trigger system for the duration of the readout sequence. It then gates in sequential order the pairs of current pulsers and grounding circuits which reset groups of eight cores at a time along the x- and y-arrays of all the spark chamber decks. The spark location data generated by each current pulse are stored in an eight-bit shift register and then shifted serially into the scan electronics package. When set cores are encountered the scan system pauses to insert the core locations into the telemetry stream.

In the present readout system the raw data may be compressed into a form giving the number of adjacent cores set (in an allowed range from one to four) and the address of the last adjacent set core in a particular spark location. In this mode the system must typically pause only once for each spark, hence the total readout time is significantly decreased. The scanning electronics resumes the search for the next spark location during the sequential extraction of previous data by the telemetry system. When the next location is encountered the readout then pauses only until the telemetry is ready to accept the new data. After all cores in both chambers have been interrogated, both the scan

electronics and the two chamber shift registers are reset and the telescope inhibit level is lowered to allow the next event trigger.

In principle, the scanning rate for each spark event determines the dead time of the detector. The internal clock which drives the scan system through the readout cycle has a frequency of about 200 kHz. In the original version of the scan system, the rate at which cores were interrogated was one-eighth of this value, which is about twice as high as the telemetry bit rate of 12 kHz. This rate fixed the average readout time per spark event at about 160 ms for the data-compressing mode. In a newer version of the scan electronics the interrogation rate has been increased to that of the basic clock frequency. With the present ability of the system to compress the spark location data and to proceed to the next set core location during telemetry readout, the telemetry bit rate is left as the main intrinsic limitation on the readout duty cycle.

In the present detector, however, the readout INHIBIT level to the telescope system is fixed by a monostable circuit rather than the readout time. This feature was included to insure that the shower counter PHA information is always properly associated with corresponding spark event data in the telemetry format. The duration of the monostable level is about 200 ms, which is slightly longer than that of a major frame (see section H). For the flights described in Chapter VI, the resultant increase in dead time was not unreasonably high. (During atmospheric ascents the fractional dead time never exceeds 50 percent, and is typically 15 percent at float altitudes.)

4. Optical and Magnetic Shielding

In tests of four-module stacks for the present detector it was found that edge sparking produced by the fringe fields at a corner of one module could cause similar breakdowns in adjacent modules. Apparently photoionization by extreme ultraviolet photons generated in the initial discharge tended to produce sparks in nearby grid planes. To combat this effect adjacent modules have been optically shielded from each other by sheets of .006-mm mylar, aluminized on the surfaces facing away from the grid planes, and covering both sides of each module frame. The sheets are bonded to mica strips which separate them from the nearest grid wires by 3.5 mm. Sagging of the sheets has proved to be negligible.

The modules in the two tiers closest to the magnet also required substantial magnetic shielding. In preliminary tests an ambient field strength near 75 gauss was found to saturate the ferrite cores sufficiently to hinder their reversal. The fringe fields measured at some module positions are as high as 600 gauss. For this reason it was necessary to use shielding material that does not saturate at much lower field strengths. The material chosen was Ad-mu 00, obtained from Ad-Vance Magnetics Corporation. The shields were fashioned from 25.4 cm. x 12.2 cm. x .11 cm. plates of this alloy. Each plate was folded along its length to fit over one core array and then spot-welded to three other pieces to form a stack enclosing one side of each tier. The tiers nearest the two spark chamber bulkheads were satisfactorily operated without any shielding in this version of the detector.

E. The Magnet

The pole faces of the permanent magnet flown in this version of the detector are 15 cm. square, and the gap distance is 8 cm. The bulk of the magnet is made from sections of Alnico V alloy, while the pole faces are mild steel. The total weight of the assembled magnet is 40 kg.

The central field slightly exceeds one kilogauss. However, in estimating particle deflections it is more informative to specify the integral of the normal field along the central axis of the magnet. Let the center of the magnet be taken as the origin of a (right-handed) Cartesian coordinate system in which the z-axis is vertical and the central field lies along the positive x-direction. (The spark chamber labeling scheme follows this convention.) Then the field integral I is defined by the expression $\int dz B_x(0,0,z)$.

The evaluation of the field integral (as well as the calculation of particle rigidities described in Chapter VI) requires an explicit three-dimensional map of the field vector. For this purpose a gaussmeter equipped with a three-axis probe was used to map out the field components within 1-cm^3 cells over one complete octant (+ x, + y, + z). A large (and possibly variable) offset in the z-axis readings has limited the useful measurements to the components in the x and y directions, although accelerator calibrations at 50-140 MV indicate that the z-component does not measurably contribute to the deflection of particles triggering the telescope. The field map was extended outside the telescope geometry in the x and y directions and up to z ≈ 20 cm., at which point the field strength is less than 10 percent of its central value. Several checks were made within other octants to insure that no significant asymmetries in the magnet configuration had to be taken into

account. With the field values obtained in this manner, the field integral I has been found to have a value of 24.9 kg-cm.

F. Shower Counters

1. Configuration

The shower counter stack is contained in the lower pressure vessel just beneath the telescope counter S2. It consists of a sandwich of four lead alloy plates and two Pilot M plastic scintillators, arranged as shown in Figure 1.3. The RDP16 lead alloy contains 98.9% lead, 1% tin, and 0.07% calcium, and is manufactured by St. Joe Minerals Corporation. These plates have essentially the same radiation length in centimeters as ordinary lead but considerably greater structural strength. They have been used in an effort to minimize sagging of the plates in the stack.

The rectangular scintillators each have an area of 30.5 cm x 29.2 cm and are .635 cm thick. Two lead plates of equal area and a thickness of about one radiation length (0.51 cm) and enclose the pair of scintillators in the stack. Approximately two radiation lengths have also been placed between the two counters. The lowest thickness of lead has been included to avoid transition effects in the bottom scintillator.

The primary role of the shower counter is that of providing an additional check on the type of particle triggering each spark chamber event. At rigidities below 800 MV a proton traversing the lead plates is unlikely to produce a cascade shower comparable to that produced by an electron because of the low probability for nucleonic interactions at the corresponding kinetic energies. In addition, below about 500 MV the range of a proton or any heavier nucleus is considerably shorter than those of the components of electron cascade showers.

Each of the two counters in the stack is viewed through a plastic light pipe by a single RCA 4524 phototube, which has 10 stages and a

7.6 cm. diameter. One Velonex PP-8 high voltage supply is provided to operate both tubes.

2. Pulse Height Analyzers

The dynode output of each phototube is inverted by a charge-sensitive preamplifier (CSPA) mounted near the tube shield and then sent to one of two independent pulse height analyzers. The latter are contained in a package mounted just below the telescope NIM bin. A block diagram of an individual PHA system may be found in Figure 5.8. Its main components are described below.

A two-slope amplifier, which accepts the negative output pulses from the CSPA, sends a portion of the input signal through an initial high-gain amplifier and then into a limiting amplifier. The output of the limiting amplifier is added to the remaining portion of the input signal and sent into a summing amplifier. Input signals which are too low to cause limiting result in a high-gain linear output. When limiting is reached, however, the output signal becomes much less sensitive to increases in the CSPA output. The behavior of the two-slope amplifier for the entire range of normal input signal levels is shown by the calibration curves in Figure 5.9.

The positive output of the two-slope amplifier is routed through a 2-microsecond delay line to a linear gate, which is opened by a trigger input from the telescope system. (The trigger signal is identical to the START SCAN pulse which initiates the spark chamber readout.) From the linear gate the amplifier output is sent into a height-to-time converter (HTC) which in turn fires a gated clock. The HTC output pulse duration, and hence the time interval during which the clock is activated, is directly proportional to the input pulse height. The clock output is a train of positive 5-volt rectangular pulses having approximately 1-microsecond widths and a 2-microsecond period. The

pulse train from each clock is then counted by one of the two scalers allotted to the shower counter in the PCM telemetry package.

Special precautions have proved necessary in grounding the circuits used in the shower counter electronics system. Since the chassis ground is a source of considerable noise during the spark chamber firing period, it first seemed particularly important to isolate the CSPA circuit ground from the chassis. However, much greater noise reduction was eventually achieved by grounding both the CSPA and PHA circuit commons to the detector chassis. (The enclosures for both systems were also grounded directly to the chassis.) With the present arrangement all noise pulses fall well below the signal produced by a single minimum ionizing electron or proton. The majority of electrons above 50 MeV produce considerably higher outputs in at least the first counter of the stack.

The accelerator calibrations described in Section B have provided pulse height distributions from both shower counters for electrons between 50 and 140 MeV. These distributions display minimum-ionizing peaks identical to those appearing in the flight data distributions shown in Figure 6.8 (see also the discussion in Section H of Chapter VI). The calibration data has also been used to compare the percentages of 50-140 MeV electrons rejected by imposing pulse height selection criteria on particle events in the calibration and flight data respectively. These comparisons and their significance will also be discussed in Section H of Chapter VI.

G. Telemetry System and Data Format

The spark chamber data, calorimeter PHA outputs, and housekeeping information are encoded and telemetered by a Monitor PCM system at a bit rate of 12 kHz. The telemetry format is shown in Figure 5.10. Each solid block represents one 16-bit data word. In this scheme the data for each spark location has a length of one word.

A complete row of eight words constitutes a minor frame. The complete sequence of 16 minor frames completes one major frame. Every minor frame begins with a frame synchronization word whose last four bits are cycled to provide the minor frame number. The second word is divided into two eight-bit syllables, containing commutated analog and digital housekeeping data respectively. The last six words in every minor frame are reserved for spark chamber information.

A list of the analog and digital data comprising the housekeeping information is given in Table 5.2. The analog-to-digital converters and scalers required to accept the various input signals are provided in the main system and auxiliary modules obtained from Monitor Systems. All the counters are reset after every readout, with the exception of the telescope rates $S1 \cdot \overline{A1} \cdot \overline{A2} \cdot S2$ and $C \cdot S1 \cdot \overline{A1} \cdot \overline{A2} \cdot S2$. The Cerenkov (C) rate counter is prescaled by a factor of 16. The scalers for those inputs labeled QUASILOG in Table 5.2 employ a digital compression scheme to give a quasilogarithmic output.

TABLE 5.2

HOUSEKEEPING PARAMETERS

Analog	Digital
1. Low Alt. Press.	1. 5-Fold Coin Rate ($C \cdot S1 \cdot \overline{A1} \cdot \overline{A2} \cdot S2$)
2. High Alt. Press.	2. 4-Fold Coin Rate ($S1 \cdot \overline{A1} \cdot \overline{A2} \cdot S2$)
3. Spk. Ch. Press.	3. $C \cdot S1$ Coin-Rate *
4. C-Counter Press.	4. S2 Rate *
5. Electronics Temp.	5. S1 Rate *
6. Primary Current	6. C Rate (X16 Prescale) *
7. Heater Current	7. A1 Rate *
8. Outside Temp.	8. A2 Rate *
9. C-Counter Temp.	9. Major Frame Counter
10. Electronics Press.	10. Dead Time Counter
11. U. Spk. Ch. Temp.	11. D1 Pulse Height
12. L. Spk. Ch. Temp.	12. D2 Pulse Height

* Quasilog

CHAPTER VI

ANALYSIS OF FLIGHT DATA

The first three balloon flights of the instrument described in Chapter V were launched from Fort Churchill, Manitoba, in July, 1972. The selection of a launch site at intermediate or high geomagnetic latitudes was dictated by the requirement of a low geomagnetic cutoff rigidity allowing the penetration of interplanetary electrons in the energy range of interest to balloon float altitudes. While the cutoff rigidity at the geographic latitude of Fort Churchill (59°N) is subject to a significant diurnal variation, during nighttime periods the average cutoff rigidity drops below 20 MV (Hovestadt and Meyer, 1970; Israel and Vogt, 1969). This value is roughly equal to the threshold rigidity imposed by the gas Cerenkov counter for electrons incident on the detector. In contrast the average daytime cutoff is significantly higher, typically exceeding 100 MV (Israel and Vogt, 1969; Hovestadt and Meyer, 1970).

The diurnal variation in the cutoff rigidity occurs at intermediate geomagnetic latitudes (between polar and equatorial zones whose boundaries are both time and rigidity dependent) and is associated with the distortion of the geomagnetic field by the solar wind (magnetospheric tail effect). The field lines emerging from the intermediate and equatorial zones on the sunward side of the earth are compressed by the streaming solar plasma, while the lines on the opposite side are inflated and convected outward into interplanetary space. As noted by Jokipii et al.

(1967), in both the polar and intermediate zones the inflated lines are effectively open and hence unable to store fluxes of low-rigidity particles (return albedo cosmic rays) between conjugate points in the geomagnetic field. The lack of contamination by return albedo particles during nighttime periods at the latitude of Fort Churchill is an important factor in observations of interplanetary electron intensities below about 300 MeV, a regime in which atmospheric secondary electrons alone make the observations extremely difficult.

A. Flight Descriptions

The flights of this detector were carried out as part of the continuing Skyhook high-altitude research program conducted by the Office of Naval Research. The launches, tracking, and recoveries of the instrument package were performed by the Flight Operations crew from Raven Industries, Sioux Falls, South Dakota. A brief description of the three flights (the first of which was accidentally terminated during the atmospheric ascent) has been summarized in Table 6.1. More detailed information is available in Interim Report Number R-0473002 (1973), prepared by Raven Industries for the Office of Naval Research.

TABLE 6.1

BALLOON FLIGHT DATA

Flight No.	72L1	72L2	72L3
Date	3 July 1972	7 July 1972	20 July 1972
Launch Time	03:59 UT	00:56 UT	00:51 UT
Float Time	-	04:30-16:30 UT	05:00-18:30 UT
Altitude	-	1.9 g cm^{-2}	2.5 g cm^{-2}
Balloon	Winzen Stratofilm 18.5×10^6 cu. ft. .6 Mil,2.6 Mil Caps	Winzen Stratofilm 30.5×10^6 cu. ft. .6 Mil,2.7 Mil Caps	Winzen Stratofilm 18.5×10^6 cu. ft. .6 Mil,2.6 Mil Caps

All of the flights were scheduled for launching after 18:00 local (CDT) time in order to avoid exposure of the instrument to the daytime flux of return albedo electrons during any part of the ascent through the atmosphere. Although it would clearly be desirable to maximize the nighttime float duration, a return albedo contamination would affect measurements of the depth dependence of atmospheric secondary electron intensities.

As discussed in Section F below, these measurements play a critical role in estimating the residual atmospheric secondary contribution at float altitudes.

In the first flight (designated 72L1 in Table 6.1) the instrument reached a height of about 11 km (230 g cm^{-2}) before the accidental termination. The data accumulated during the ascent to this altitude has not been included in the analysis described in the following sections, since only depths less than about 100 g cm^{-2} are of great significance for the depth dependence measurements (see Section F).

The second flight (72L2) was made with a 30.5 million cubic foot balloon and reached a float depth of 2.0 g cm^{-2}, remaining at nearly constant altitude for a period of about 11 hours. The instrument performed well throughout the flight, although a leak in the gas Cerenkov counter pressure vessel (which appeared about an hour after launch and persisted through most of the ascent phase before sealing itself off) reduced the carbon dioxide pressure to about 0.5 atm for the entire duration of the float period.

The Cerenkov counter was filled to a pressure of 2 atm in leak tests made prior to the third flight (72L3). No significant loss of pressure occurred when the Marmon clamps mating the Cerenkov counter and spark chamber pressure vessels (and the smaller Marmon clamps around the phototube housing caps) were tightened to about their maximum recommended limit. In spite of the satisfactory results of these ground tests a small leak did appear briefly after the launch of 72L3, but in this instance less than 0.1 atm was lost. The 18.5 million cubic foot balloon carried the instrument to a float depth of 2.5 g cm^{-2}. During the final phases of the ascent, however, abnormally low temperatures in the detector electronics

package caused a reduction and eventual loss of the output rate from the $C \cdot S1 \cdot \overline{A1} \cdot \overline{A2} \cdot S2$ coincidence circuit (which provides the spark chamber trigger pulses). Both the ascent data below about 10 g cm^{-2} and the nighttime float data were severely affected by the drop in the triggering efficiency. An increase in temperature brought the coincidence circuit output rate back to its normal value by 10:00 local time, and daytime float data was accumulated for about 3.5 hours.

The three flights have provided a total of over nine hours of nighttime float data (from 72L2) and useful ascent data from both 72L2 and 72L3. The two sets of ascent data have been of particular value in the evaluation of the Cerenkov counter detection efficiency (discussed in Section B of Chapter V).

B. Automatic Processing Procedure

1. Data Tape Processing

The analog telemetry data tapes from flights 72L2 and 72L3 were first converted to digital form for subsequent automatic processing. During the digital conversion process the approximate (CDT) flight time was recorded in parallel with the data stream from each tape, since an interference problem with the time code generators at the ground receiving stations had prevented the inclusion if a real time channel on the analog tapes.

The digital tapes were used to produce two independent sequences of reformatted tapes containing the instrument housekeeping information and the spark chamber event records (with the shower counter PHA outputs) respectively. The housekeeping data has been summarized on printouts and time charts recording 2- or 3-minute averages of all the analog and digital parameters listed in Table 5.2. The event record tapes contain the spark chamber core location data used in rigidity calculations, which will be discussed in Section D below.

2. Automatic Track Identification

An automatic track identification routine was employed in the generation of the original event record tapes. A complete description of this program has been presented by Greville (1973). For each spark event the program first attempts to identify single-particle tracks in the core location data, and then generates error codes classifying the event as acceptable (in which case those core locations associated with the identified track are tagged), deletable, or questionable (requiring a display of the spark chamber data for visual inspection or editing). In the case of questionable events, cores associated with partially identifiable track segments

are tagged automatically so that they may be indicated for convenience on a visual display.

In the present analysis, a conservative approach has been taken in imposing the track acceptance and rejection criteria for this program. Automatically accepted events must have exactly one identifiable track segment in each tier, and the slopes found in each pair of tiers (above or below the magnet gap) must match with specified accuracy. A minimum of three core locations is required to identify a track segment in each tier, unless two locations in one tier are found sufficiently close to the projected segment from the other tier in each pair. In addition, there must be no anomalous deflections within the gap region in the projection parallel to the magnetic field.

Events with more than one identifiable track segment in any tier or too many set core locations not associated with any track are tagged questionable, as are all events with significant deflections outside the magnet gap region. Only those events with no set cores in at least one tier or too few points for satisfactory track identification in any tier are automatically deleted.

It should be noted, however, that all the event record information read from the raw data tapes is retained on the automatically generated event record tapes (and all revised versions of the event record tapes which incorporate visual editing data). Both the track identification tags on individual core locations and the event classification labels are subject to editing or removal without the loss of either the core location data itself or any complete event records (including those events labeled deletable). Thus any version of the event record tapes may be used in producing subsequent versions with modified track identification

tags and event classification labels. By this procedure the visual editing data obtained by the methods discussed in the next section have been used to produce completely edited event record tapes from the original (automatically edited) versions.

The event record tapes for flights 72L2 and 72L3 contain 29,661 and 26,809 events respectively. The automatic track identification routine has proved capable of accepting or deleting about 60 per cent of the ascent data from each flight and a somewhat smaller portion of the float data. An examination of a sample of 600 consecutive events from the ascent portion of 72L2 revealed only three accepted events which should have been edited to remove tagged cores (no more than one in any single event) which deviated by two to five core spacings from the apparent track segment. Since automatically accepted events must provide at least five tagged core locations in each pair of tiers for line-fitting calculations, no attempt has been made to remove such cores in the automatically accepted events by visual inspection (except in selected classes of events to be described in the following section). As a further precaution, however, the rigidity estimation technique discussed in Section D includes checks to remove such stray tagged cores from each track segment.

A similar inspection of the automatically deleted events (over 95 per cent of which were rejected because at least one tier was devoid of any set core locations) showed no events which might have been acceptable after hand editing. Hence the remaining deleted events have not been inspected.

C. Visual Editing of Spark Chamber Data

1. Procedure

Those events on the original spark event record tapes which could neither be completely processed (accepted) nor deleted by the automatic track identification routine have been visually inspected and edited or deleted with the use of an IBM 1130/2250 Computer Graphics Display. This system permits human scanners to generate editing information for each event, which is accumulated on a memory disk during each scanning session and later transferred to editing data cards or tapes. The stored editing information is then used to produce revised copies of the spark event record tapes.

The 2250 CRT event display format, showing the four projected views of the upper and lower spark chambers, is shown in Figure 6.1. (The term view is here conveniently defined as the x- or y-projection of the pair of tiers in either spark chamber.) The outlines of the central magnet and the four telescope scintillators appear on the 2250 screen as indicated in the same figure, and are scaled with the four spark chamber views to the correct relative dimensions. Also shown in Figure 6.1 are the track identification tags on individual core locations and the automatically drawn fit lines for a typical partially processed event.

In the 10 per cent of the visually inspected events, tracks had already been automatically identified in all four spark chamber views but were subsequently tagged questionable (too many deleted core locations, more than one possible track segment in some tiers, significant deflection through the magnet gap in the x-z views). Many events of this type have been inspected and accepted without modification, since the automatic acceptance criteria are rather stringent and are not intended to

allow the automatic processing of all good events. On the other hand, more than 60 per cent of the inspected events have necessarily been deleted, since cosmic ray interactions occurring within or near the detector produce many spurious triggers resulting in events with multiple tracks or spark patterns bearing little resemblance to track segments. (Such events are prevalent at float depths, where the flux of incident particles is more nearly isotropic.)

For each of the remaining questionable events, the individual core locations associated with a single-particle track segment have been tagged with a light pen by the scanner. The display system has been programmed so that editing of this type may be performed on all the classes of events processed automatically on the event record tapes, including any events previously tagged as accepted or deleted. The light pen editing of each event may include the removal of automatically tagged core locations as well as the inclusion of previously untagged cores in a given track segment.

2. Editing Criteria

Because of the small amount of detector material above and within the spark chambers, electrons between 50 MeV and 1 GeV only infrequently exhibit large deflections or multiparticle tracks identifiable with knock-on ionizing or radiative collisions. Hence the acceptance criteria followed in hand editing the questionable events have been fairly straightforward. Tracks whose rigidities could not be estimated because of obvious deflections (greater than about five degrees) between either pair of tiers, or within the tiers adjacent to the magnet gap, have necessarily been deleted. However, these lost events constituted less than 4 per cent of the total number of questionable events. A somewhat larger

percentage has been rejected because of anomalous deflections in the x-z projection of the magnet gap. In almost all of these cases the particles had apparently been scattered by a pole face of the magnet, and would not otherwise have satisfied the detector telescope requirements. (The rigidity analysis routine described in Section D is capable of rejecting those events whose estimated trajectories intersect the magnet material in the y-z view.)

Small-angle scattering (especially less than three or four degrees) either within or between the tier projections is usually too difficult to observe on the 2250 display and must be estimated from the goodness of fit to the assumed straight trajectories calculated during the rigidity analysis. As shown in Section D, the aggregate effect of random small-angle scattering (rather than the intrinsic resolution of straight trajectories in the spark chamber configuration) is the practical limiting factor in the rigidity resolution of the detector below 600-800 MV.

Events with two or more apparent tracks in either tier of the spark chambers have in general been deleted, although two special classes of multiple-track events were edited and kept in the initial scanning sequence for each flight. The first class exhibited a principal track and one or more short accompanying tracks (not extending beyond the first tier) just below the Cerenkov counter bulkhead. Many of these tracks could be attributed either to incipient electron showers or nucleonic cosmic ray interactions above the upper spark chamber. These events were tentatively retained so that the shower counter pulse heights could be used to indicate those cases in which the single particle traversing both spark chambers could be identified as an electron. The second class of events displayed a principal track which appeared to produce short range

knock-on electrons (delta rays) in some tier without observable deflection.

All events in these two classes which were eventually identified as electrons within the energy range 400-800 MeV have been subjected to a second inspection. For this sample an error limit of 5 per cent has been set on the percentage of erroneously accepted or hand edited events.

Events in which multiple tracks appeared to emerge from the lower bulkhead have been rejected because of the likelihood that the tracks were due either to interacting cosmic ray nuclei or to upward-moving particles. It should be noted that backward scattering may occasionally be observed in electron showers as well as nucleonic interactions. However, the event records from available electron calibration data suggest that this is a relatively infrequent occurrence, at least for energies up to 140 MeV. In any case the number of events rejected on this basis has not exceeded 3 per cent of the inspected events.

With the set of acceptance and rejection criteria outlined above, the overall efficiency for the acceptance of spark events triggered by single electrons above about 100 MeV may reasonably be expected to exceed 90 per cent and is probably as high as 95 per cent. This large acceptance factor is principally due to the sparking efficiencies of the individual grid modules, which have all been found to range between 85-95 per cent. Between 50 and 100 MeV the probability of acceptance may drop slightly due to increased random scattering, but quantitative estimates of this effect from the available calibration data have been precluded because of unusually poor sparking efficiency (possibly resulting from air contamination) during the calibration runs. Hence in the present analysis the scanning acceptance efficiency has been assumed to be 95 ± 5

per cent at all energies.

The editing data accumulated during each scanning session were used to generate a revised copy of the event record tape. The fully edited versions of the event record tapes have been used to calculate the rigidities of accepted particles by the technique described in the following section.

D. Determination of Particle Rigidities

1. Approximation Technique

An exact expression for the rigidity ρ of a charged particle traversing a static magnetic field may be written in the form

$$\rho \equiv \frac{pc}{Ze} = \frac{\left| \int_i^f ds \, \frac{d\underline{n}}{ds} \times \underline{B} \right|}{2 \sin \frac{\theta}{2}} \qquad 6.1$$

where θ is the angle between the tangential directions (in three-dimensional space) to the particle trajectory at two conveniently chosen points labeled i and f. The field-path length integral is evaluated between these same points along the deflected trajectory.

In general, the evaluation of equation 6.1 requires a knowledge of the magnetic field vector at all points along a specified trajectory between i and f. As will be shown below, the complex fringe fields of the magnet in the present detector cannot be neglected in accurate rigidity estimates. Hence the detailed field map discussed in Section E of Chapter V has been used in numerical integrations of equation 6.1 which have provided the rigidity estimates of tracks in the spark event records.

The deflection angle θ must be estimated from the slopes of the four straight line segments fit to the set core locations in the projected views of the spark chambers. The procedure for fitting the line segments uses the standard least squares technique, following the assumptions that the z-coordinates are precisely known and that the variances in the horizontal coordinates are all equal. The average of all adjacent accepted cores on each x or y array is considered as a single core location in the fitting procedure. An iterative routine is then used to remove points which have anomalously large deviations from the fit line, and a final check is made

to insure that enough points remain in each view to process the event.

In general, θ depends on the deflections in both the x-z and y-z views, as shown by the exact expression

$$\sin\theta = \left| \left(\frac{d\underline{r}}{ds}\right)_i \times \left(\frac{d\underline{r}}{ds}\right)_f \right| , \qquad 6.2a$$

where

$$\frac{d\underline{r}}{ds} = \frac{1}{\sqrt{1+\left(\frac{dx}{dz}\right)^2+\left(\frac{dy}{dz}\right)^2}} \left(\frac{dx}{dz}\hat{x} + \frac{dy}{dz}\hat{y} + \hat{z} \right) \qquad 6.2b$$

However, since the central field lies along the positive x-axis, the relatively small deflection between the x-z views may here be neglected and θ may then be expressed as

$$\theta = \tan^{-1} \frac{\left| \left(\frac{dy}{dz}\right)_f - \left(\frac{dy}{dz}\right)_i \right|}{\sqrt{1+\left(\frac{dy}{dz}\right)_i \left(\frac{dy}{dz}\right)_f}} \qquad 6.3$$

The presence of significant fringe fields within the spark chamber volume has required that the end points i and f in equations 6.2a and 6.3 be chosen with caution. In particular, the slope of the fit line through the set core locations in each pair of tiers should be associated with the tangent to the particle trajectory at some intermediate point between the two tiers. The location of this intermediate point depends on the relative strength and extent of the fringe fields but is nearly independent of particle rigidities over the range of present interest. Numerical integrations of particle equations of motion through the field of the detector have shown that the intermediate points lie near the planes $z = \pm 20$ cm. Hence the intersections of the fit lines in each view with these planes have been used to fix the limits of integration in equation 6.1.

Since the rigidities of the particles in the spark event records are unknown beforehand, the exact trajectories through the magnetic field cannot be reconstructed by integrating the equations of motion. Hence an approximate trajectory must be assumed in the evaluation of equation 6.1.

The procedure used in the present analysis has consisted in replacing the true y-z projected trajectory by a segment of a circle which is tangent to both of the fit lines at the points i and f respectively and coincident with the upper projected segment at the starting point i. The calibrations of the instrument have indicated that this approximation technique introduces negligible errors at electron energies down to 50 MeV.

2. Resolution

The accuracy of rigidity measurements in the detector is limited both by the finite interwire spacing (.127 cm) in each spark grid plane and the random scattering of particles near the magnet gap region. Above several hundred MV the spacing determines the resolution, since the uncertainty in the straight-line slope fit through the set core locations in either pair of tiers becomes comparable to the difference in the sopes above and below the magnet gap. Slight overestimates based on flight data (which include the effects of random scattering within each spark chamber) indicate that above 600-800 MV the relative uncertainties due to line-fitting errors alone reach 30-40 per cent.

At lower rigidities, however, the random Coulomb scattering os particles near the magnet gap becomes the principal limiting factor in the rigidity resolution. The RMS (projected) scattering angle for a particle of rigidity ρ (measured in MV) which has traversed t radiation lengths of matter is given approximately by the expression (Moliere, 1948)

$$\Delta\theta \simeq \frac{15}{\rho\beta} t^{\frac{1}{2}} \qquad 6.4$$

This equation has been used to estimate the scattering in the spark grid wires, the mylar optical shielding planes, and the gas mixture throughout a central region encompassing both biers nearest the magnet. For electrons the calculation has yielded the result

$$\Delta\theta \simeq \frac{1.4}{\rho} \qquad 6.5$$

Since the field integral I discussed in Section E is about 25 kilogauss-cm, the rigidity of a particle deflected by an angle is given approximately by

$$\rho \simeq \frac{(0.3)(25)}{\theta} \qquad 6.6$$

Equations 6.5 and 6.6 then imply that

$$\frac{\Delta\theta}{\theta} \simeq \frac{\Delta\rho}{\rho} \simeq 0.2 \qquad 6.7$$

Hence the relative uncertainty due to multiple Coulomb scattering should have a roughly constant value of about 20 per cent.

However, the available calibration data for electrons between 50 and 140 MV (shown in Figure 6.2) indicates that the resolution is more nearly about 30 per cent. This value may in fact be only an upper limit, since the energy dispersion of the beam may itself approach 30 per cent (see Section B.2 of Chapter V). No more accurate determination of the beam energy dispersion is available to resolve this question. It should be noted, however, that the maximum uncertainties due to scattering are smaller than the relative width of the rigidity intervals chosen for the analysis of the flight data described in Section F.

E. Spark Chamber Alignment Corrections

The rigidity estimation technique discussed in the previous section has been used in a program which reads the set of completely edited event record tapes for each flight and produces a tape data file summarizing the results of the rigidity analysis of all acceptable events. In addition to the final (positive or negative) rigidity estimates, the summary data include the line-fitting parameters and error flags indicating large estimated errors in the fit parameters or the deletion of previously accepted core locations during the calculation. The pulse height data from the shower counter are also retained on the summary tape (both in the form of direct output channel readings and in terms of the equivalent number of minimum-ionizing particles).

The original version of the summary tape was used to search for systematic errors in the relative alignment of the upper and lower spark chambers and in the horizontal positions of the individual grid modules. The fiducial required to determine the small angle between the vertical axes of the two spark chambers was provided by the distribution of y-z deflections of particles which produced minimum-ionizing pulse heights in both shower counters. These particles (which at float depaths are mainly protons above the gas Cerenkov counter threshold rigidity of 30 GV) exhibit a well-defined peak at true angular deflections less than one milliradian. However, in the data from both flights the observed peak in the y-z deflections (accumulated from the original summary data) has been found to be displaced by a few milliradians corresponding to a slight misalignment of the spark chamber axes. As a first-order correction in repeated rigidity calculations, this observed displacement angle has been subtracted from the estimated deflection angle for each event as given by

equation 6.3. (Since the small particle deflections in the x-z plane are not considered in this expression, similar small displacement angle corrections in this projection need not be considered.)

A complicating factor discovered in the analysis of both flights was that slightly different angular deflection corrections appeared to be required for the ascent and float data. The difference was only about two milliradians but could not be satisfactorily explained in terms of the dominance of atmospheric secondary particles during the ascent (since the true average deflections of all minimum-ionizing atmospheric secondary particles and the minimum-ionizing protons able to trigger the Cerenkov counter should both be less than one milliradian). An alternative explanation, which has been assumed in the present analysis, is that a changing stress experienced by the detector pressure housing during the ascent caused a slight shift in the spark chamber alignment.

While the numbers of events in short time intervals are not adequate to trace this shift in alignment with precision, rough estimates based on two and three-hour intervals suggest that in both flights the angular displacement was nearly constant throughout most of the ascent and then shifted to a second nearly constant value during all or most of the float duration. Hence the attempt to correct for the apparent shift has consisted in dividing each flight into ascent and float portions (with an arbitrary transition at 5 g cm^{-3}) and generating two separate summary tapes with the corresponding angular deflection corrections.

It should be noted that the spectral analysis of the data on both of these summary tapes has yielded roughly identical results over corresponding time intervals, at least within the rigidity range 50-800 MV. Hence this correction has had no significant effect on the spectral measurements of positrons and negatrons in the present range of interest.

Net horizontal displacements in either the x or y directions for individual grid modules have been found by plotting histograms of the x- or y-deviations in each grid plane from the intersections with corresponding fit track segments. Non-zero average displacements found from the original summary data have also been used as additive corrections in repeated rigidity calculations.

A final rigidity analysis has employed both the angular and horizontal displacement corrections to produce the pair of revised summary tapes for each flight. These versions of the summary tapes have been used in the spectral analysis to be described in the following sections.

F. Spectral Measurements and Atmospheric Background Corrections

1. Rigidity Intervals

The final event summary data from each flight has been used to produce histograms of particle numbers (counted between specified times or atmospheric depths) within arbitrary positive and negative rigidity intervals between 50 and 800 MV. It has proved convenient to divide this range of rigidities into four equal logarithmic intervals, namely 50-100, 100-200, 200-400 and 400-800 MV. The large bin widths are principally due to the limited numbers of particles counted during the time intervals of interest (typically 15 minutes during the ascent phase, since as discussed below an attempt has been made to measure the positron and negatron intensities as functions of atmospheric depth). However, the fact that the rigidity resolution of the instrument has not been calibrated in accelerator beams above 140 MV also precludes the use of smaller rigidity intervals at least above 200 MV in the present analysis.

The low Cerenkov counter detection efficiency for electrons below 50 MV during most of flight 72L2, as well as the lack of usable float data from 72L3, have prevented measurements of electron intensities below this limit at present. The upper limit of 800 MV (corresponding to a deflection in the gap region of roughly 10 milliradians or 0.6 degrees) is a crude estimate of the maximum rigidity measurable with the present detector, since above this limit the average relative uncertainty in the deflection angle measurements has been found to exceed 30-40 per cent.

2. Search for Diurnal Intensity Variation

The raw counting rates observed for particles in the rigidity intervals 50-100 and 100-200 MV during flight 72L2 were examined in a search for the diurnal variation of the electron intensities described in the introduction to the present chapter. Particle counts in each rigidity interval were accumulated over two overlapping sequences of one-hour periods. The relative displacement of the starting times for the two sequences was 30 minutes.

In the 50-100 MV interval, an abrupt rise of roughly a factor of two was observed in the counting period which started at 10:00 CDT. A considerably less significant rise appeared in the 100-200 MV interval during the same period. However, the displaced counting period which started at 9:30 CDT displayed an increase of only 1.2-1.5 even in the 50-100 MV interval. Hence for the data from flight 72L2, the onset of the daytime intensity increase has been assumed to occur after 10:00 CDT.

Although the higher rigidity intervals show no significant intensity increases after 10:00, no particle counts in any rigidity interval have been included in the analysis of the float data. Hence the present measurements should be free of contamination by return albedo electrons at all energies.

3. Depth Dependence of Secondary Electrons

The particle counts in each of the eight positive and negative rigidity intervals include a contribution from atmospheric secondary electrons, which is significant even at residual atmospheric depths as low as 2 g cm^{-2}. The most serious contamination by atmospheric secondaries occurs in the intervals below 200 MV, where in fact they are at least comparable to the primary electron intensities at all epochs in the solar cycle. Even in the higher intervals, however, the secondary background at the float depth of the instrument must be estimated and subtracted from the total measured intensities.

Several calculations of secondary electron spectra at various atmospheric depths and geomagnetic latitudes have been published (Perola and Scarsi, 1966; Verma, 1967; Beuermann, 1971; Daniel and Stephens, 1973), but the results depend on differing approximations and are not in complete agreement. Furthermore, the calculation of the absolute secondary electron intensities requires a knowledge of the time-dependent spectra of interplanetary protons and helium nuclei. The available calculations are in fact valid only for specified epochs in the solar cycle, and must be corrected for differences in the nucleonic cosmic ray spectra at other epochs of interest.

As Beuermann (1971) has noted, however, two properties of the secondary electron intensities are not very sensitive to the temporal variations in the solar modulation of cosmic ray nuclei. These parameters are the relative intensities of the positron and negatron components as functions of energy (the charge ratio), and the atmospheric depth dependence of these intensities within fixed energy intervals.

The depth dependence of the total (positive and negative) electron component has been measured in a number of previous balloon experiments (see for example L'Heureux, 1967; Webber and Chotkowski, 1967; L'Heureux and Meyer, 1968; Simnett, 1968; Bleeker et al., 1968). Most of these observations have been compared with assumed linear or near-linear growth curves for the secondary component as a means of estimating the primary intensity. Similarly, Beuermann et al. (1970) have compared the depth dependence curves calculated by Beuermann (1971) for the separate positron and negatron intensities with magnetic spectrometer measurements between 12 and 220 MeV. The search for significant departures from predicted secondary growth curves toward low atmospheric depths has in fact been generally considered the most reliable procedure for separating primary and secondary electron intensities in balloon measurements.

However, recent calculations by Daniel and Stephens (1973) have resulted in negatron depth dependence curves which are not in agreement with the work of Beuermann (1971) at energies less than about 1 GeV. The differences are most important at depths below 100 g cm^{-2}. Compared to the positron component, for which the two calculations give roughly similar results at all depths, the negatron intensities given by Daniel and Stephens (1973) decrease more rapidly with decreasing depth. At 70 MeV, for example, their negatron growth curve may be approximated by a power law of the form $s(x) \propto x^{1.15}$ for depths x less than about 40 g cm^{-2}. At the same energy, Beuermann (1971) fits his results to the form

$$s(x) = C x^{0.95}, \quad 2 \leq x \leq 15 \text{ g cm}^{-2}$$
$$= 1.3 C x^{0.86}, \quad 15 \leq x \leq 40 \text{ g cm}^{-2}$$

These significant differences arise in part because the two calculations use entirely different methods of estimating the charge ratio $\frac{N_{\pi^+}}{N_{\pi^-}}$ of the pions created by the collisions of cosmic ray nuclei in the atmosphere. (The total charged pion production spectra given by the two calculations are also not in complete agreement, although both treatments closely follow the approach taken by Perola and Scarsi, 1966.) Daniel and Stephens (1973) infer the value of $\frac{N_{\pi^+}}{N_{\pi^-}}$ at a given energy from values estimated by Ramaty and Lingenfelter (1966) for pion production in interstellar collisions. It should be noted, however, that the work of the latter authors relies on delta-function approximations for the pion energy distributions at given incident proton energies (see Chapter II). The accuracy of this approximation may be questioned at energies near the production thresholds, where the differences in the production cross sections σ_{π^+} and σ_{π^-} are most significant. In addition, the corrections made by Daniel and Stephens (1973) to take into account the atmospheric composition are indirect and may involve large systematic errors.

Beuermann (1971) does not derive separate positron and negatron production spectra from direct estimates of $\pi^{\pm}$ production. Instead he uses measurements of the atmospheric muon flux at sea level (MacKeown and Wolfendale, 1966) to infer a positive fraction of .55 for the electrons produced by $\pi^{\pm} \rightarrow \mu^{\pm} \rightarrow e^{\pm}$ decays at energies above about 100 MeV and all atmospheric depths. (At lower energies the negatron source arising from knock-on collisions decreases the positive fraction of the electron component in both calculations.) Hence Beuermann (1971) does not investigate the possibility cited by Daniel and Stephens (1973) that the positive fraction of secondary electrons may be rather large at low

depths (where proton collisions with air nuclei are the dominant source), while tending toward the limit of .5 at depths for which collisions by fragmented nuclei and pair creation become important sources of electrons.

It is clear that estimates of the primary negatron spectrum and the positive fraction of primary electrons depend on the assumed shape of the depth dependence curve, at least at energies for which the secondary component is comparable to the primary intensity. However, in the present analysis it has been found that the primary negatron intensity abov 200 MeV is sufficiently high that the use of either set of growth curves leads to nearly identical results (within the statistical uncertainties). Between 50 and 200 MeV the larger secondary background implies that the primary negatron component obtained following Daniel and Stephens (1973) is roughly 1.4 times greater than that found using the results of Beuermann (1971), although this difference is still comparable to the statistical uncertainties in the present data at those energies.

Since the growth curves obtained by Beuermann (1971) are in general closer to the forms assumed in the analysis of other electron measurements (and because of the large theoretical uncertainties in the calculation by Daniel and Stephens, 1973), the results of Beuermann (1971) have been adopted in the present analysis. This choice has been made in part because a detailed calculation of the type attempted by Daniel and Stephens (1973) will probably require more complete data on $\pi^{\pm}$ energy distributions near the production thresholds than is presently available from accelerator experiments. However, the summary of the final results will point out the differences in the primary negatron spectrum and the positive fraction below 200 MeV which would be obtained by adopting the growth curves due to the latter authors.

4. Negatron Intensities

Unfortunately, the depth dependence measurements of the positron intensities are complicated by an additional contamination in the positive rigidity intervals by nucleonic particles (mainly protons). Because of these spurious events, the pulse heights from the shower counter analyzers must be used to select only positron-triggered events in all depth dependence measurements. The specific pulse height restrictions imposed in the present analysis will be fully described in Section G.

Estimates of the charge ratio require the use of identical pulse height criteria in corresponding negative rigidity intervals. Although the pulse height restrictions introduce no systematic bias in the selection of positrons versus negatrons, a significant fraction of the electron events are rejected in all rigidity intervals. The rejection has been nearly random (i.e., independent of rigidity) at most rigidities for the pulse height criteria which have been imposed, but the statistical reliability of the depth dependence measurements has been significantly degraded.

Although a finite measurement of the charge ratio has still proved feasible in the range below 400 MeV in the present analysis, at higher energies no reliable separation of primary and secondary positron spectra has been possible after effective pulse height criteria have been imposed. Furthermore, the lack of calibration data above 140 MeV on the percentage of electrons rejected by each set of pulse height restrictions makes it difficult to estimate directly the absolute intensities of positrons and negatrons from the depleted spectra. However, it has proved feasible to estimate the absolute spectra by relaxing the pulse height criteria and confining attention to the intensities in the negative rigidity

intervals.

It will be shown in Section G that contamination by pions or muons in the negative intervals is in fact negligible. Hence no pulse height criteria are necessary, and it has been possible to make comparatively reliable depth dependence measurements of negatrons in each interval. These measurements will be discussed here to illustrate the depth dependence analysis technique.

Figures 6.3-6.6 show the depth dependence of negatrons in the rigidity ranges 50-100, 100-200, 200-400 and 400-800 MV respectively. The estimate of the differential intensity j_i within the depth interval i has been made by dividing the observed particle count n_i by the product of the geometric factor Γ, the detection efficiency ε , the (live) counting time Δt_i , and the energy interval $\Delta T \simeq \Delta p$. Thus

$$j_i \simeq \frac{n_i}{\varepsilon \cdot \Gamma \cdot \Delta t_i \cdot \Delta T} \qquad 6.8$$

The uncertainty shown for each measurement was determined by the estimator $\sqrt{n_i}$ for the standard deviation in the count n_i as well as the uncertainties assumed for the Cerenkov counter efficiency $\left(\frac{\Delta \varepsilon_c}{\varepsilon_c} \sim 0.1\right)$ and the scanning efficiency $(\varepsilon_s \sim .95 \pm .05)$ which essentially determine the overall detection efficiency $\varepsilon \simeq \varepsilon_c \cdot \varepsilon_s$. The smaller uncertainties in the live time ($\lesssim$ 1 per cent)and the geometric factor (± 3 per cent) have here been neglected.

The observed negatron intensity at any depth is the sum of primary and atmospheric secondary contributions. Hence the measured points in Figures 6.3-6.6 have been fit to curves of the form

$$J(T,x) = \sum_{P,S} j(T,x) = a(T)p(T,x) + b(T)s(T,x) \ , \qquad 6.9$$

where $p(T,x)$ and $s(T,x)$ are specified functions which determine the depth dependence of the primary and secondary intensities respectively. In the present analysis the energy dependence of p and s has been averaged over each interval.

The depth dependence of secondary positrons and negatrons found by Beuermann (1971) may be approximated by two power law fits, valid between 2-15 and 15-40 g cm^{-2} respectively. The spectral indices in both depth intervals are determined as functions of energy. The condition that the two fit segments match at 15 g cm^{-2} leaves only a constant multiplicative factor, which may be taken as b in equation 6.9, as a free parameter in fitting the secondary curves to given data points. Thus in the energy (rigidity) interval j, $S_j(x)$ may be conveniently defined by the expressions

$$S_j(x) = x^{\alpha_j}, \quad 2 \leq x \leq 15 \text{ g cm}^{-2} \qquad 6.10a$$

$$= R x^{\beta_j}, \quad 15 < x \leq 40 \text{ g cm}^{-2} \qquad 6.10b$$

where $R = 15^{(\alpha_j - \beta_j)}$

The depth dependence of the primary intensities must in principle reflect the distortion of the interplanetary electron spectrum by bremsstrahlung and collision losses in the residual atmosphere. Hence the shape of $p(x)$ depends on that of the interplanetary spectrum, which is unknown beforehand. As a first approximation, however, these losses may be ignored and p may be given the highly convenient form $p^{(0)}(x) = 1$. The primary spectrum derived from equation 6.9 with this form for p may subsequently be traced through the residual atmosphere to obtain a better approximation for $p(x)$ (Beuermann, 1971). The method of finding the spectral shape at each atmospheric depth will be discussed in Section H.

This iterative procedure can be repeated until a self-consistent form for p is obtained. However, in the present analysis the first interation has not significantly improved the fits to the avilable data (see Section H).

A weighted least squares fit has been used to determine the coefficients a and b in each rigidity interval. The minimized quantity may be written as

$$S^2 = \sum_i \frac{[J(x_i) - y_i]^2}{\sigma_i^2} \qquad 6.11$$

The coefficients have the forms

$$a = \frac{\begin{vmatrix} d_1 & c_2 \\ d_2 & c_4 \end{vmatrix}}{\begin{vmatrix} c_1 & c_2 \\ c_3 & c_4 \end{vmatrix}}, \quad b = \frac{\begin{vmatrix} c_1 & d_1 \\ c_3 & d_2 \end{vmatrix}}{\begin{vmatrix} c_1 & c_2 \\ c_3 & c_4 \end{vmatrix}} \qquad 6.12$$

$$c_1 = \sum_i \frac{p^2(x_i)}{\sigma_i^2} \qquad d_1 = \sum_i \frac{y_i p(x_i)}{\sigma_i^2}$$

$$c_2 = c_3 = \sum_i \frac{p_i s_i}{\sigma_i^2}$$

$$c_4 = \sum_i \frac{s^2(x_i)}{\sigma_i^2} \qquad d_2 = \sum_i \frac{y_i s(x_i)}{\sigma_i^2}$$

The standard deviations are then given by

$$\sigma_a = \left[\sum_i \left(\frac{\partial a}{\partial y_i}\right)^2 \sigma_i^2 \right]^{\frac{1}{2}} \qquad 6.13a$$

$$\sigma_b = \left[\sum_i \left(\frac{\partial b}{\partial y_i}\right)^2 \sigma_i^2 \right]^{\frac{1}{2}} \qquad 6.13b$$

The quantity S_j^2 for the rigidity interval j is a good approximation to χ_j^2, which is properly defined by

$$\chi_j^2 = \sum_i \frac{(n_i - \langle n_i \rangle)^2}{\langle n_i \rangle} \qquad 6.14$$

Here $\langle n_i \rangle$ is the number of counts expected in the depth interval i on the basis of the intensity curve $J = \sum_{P,\theta} j$. The values of a_j , b_j , S_j^2 , and χ_j^2 for each of the curves shown in Figures 6.3-6.6 are presented in Table 6.2. The product $a_j p(0)$ represents the primary negatron intensity averaged over the rigidity interval j.

TABLE 6.2

FITTING PARAMETERS, NEGATRON GROWTH CURVES

Energy Range (MeV)	a^*	b^*	S_j^2	χ_j^2 ($\nu^{**} = 6$)
50-100	.11 ± .03	.057 ± .0078	3.1	5.5
100-200	.038 ± .014	.022 ± .004	4.4	7.3
200-400	.045 ± .007	.005 ± .001	5.2	8.7
400-800	.041 ± .004	.001 ± .0004	4.3	13.9

* $(m^2\text{-s-sr-MeV})^{-1}$

ν^{**} Degrees of freedom

G. Pulse Height Selection Criteria

In order to retain the maximum statistical reliability in the atmospheric depth dependence measurements for each rigidity interval, it has been necessary to impose rigidity-dependent pulse height selection criteria. In all but the highest intervals, the restrictions used in the present analysis are based on the fact that nucleonic particles and electrons of the same rigidities have different ranges in the material of the shower counter stack. Although electrons throughout the range 50-800 MV lose most of their energy by radiative collisions in the lead plates and hence penetrate varying depths in the stack, nucleonic particles with similar rigidities have considerably more well-defined ranges. Moreover, below about 500 MV the range of nucleonic particle is much shorter than the average range of an incident electron or the secondary cascade shower electrons which the initial electron may produce within the stack.

Above 500 MV the range of a proton may become comparable with that of an electron or its shower products. However, in this regime the well-defined energy losses of nuclei at specified rigidities may be used in place of the range as the basis for the pulse height selection criteria. In principle, characteristic energy losses may also be used to remove events possibly triggered by pions or muons between 50-800 MV (whose ranges are comparable to or greater than electrons with similar rigidities). However, as discussed below the number of such events has been found to be negligible. This result is to be expected, since the Cerenkov counter threshold rigidities of pions and muons are 4.6 GV and 3.5 GV respectively. Moreover, such particles can only arise from interactions of the dominant nucleonic cosmic ray component in nearby layers

of the overlying atmosphere or within the detector. Hence the pulse height criteria used in the present analysis are specifically intended to exclude protons and heavier nuclei.

A comparison of protons and electrons at several rigidities, listing their respective kinetic energies and average ranges in lead, is shown for illustration in Table 6.3. The quoted values for protons and electrons have been taken from Barkas and Berger (1964) and Berger and Seltzer (1964). The ranges of helium and all higher-Z nuclei at the same rigidities are less than the values given for protons, since $\rho = \frac{pc}{Ze}$ and the energy loss rate $\left(\frac{dE}{dt}\right)_I$ (see for example Rossi, 1952) is proportional to Z^2. It should also be evident from Table 6.3 that at these rigidities, nuclear interactions cannot produce a significant number of events resembling electron cascade showers. The threshold kinetic energies for pion production in collisions of protons and α-particles with Pb nuclei obviously exceed 140 MeV, and below about 500 MeV the corresponding cross sections may be safely neglected in either case.

A numerical calculation has been used to estimate the relative energy losses and residual ranges of protons between 50-800 MV in the layers of the shower counter sandwich. The calculation provides estimates of the energies deposited in the two scintillators (labeled D1 and D2), from which the corresponding pulse heights may be inferred. Figure 6.7 shows the estimated relative energy losses for protons in both scintillators as functions of rigidity.

The threshold rigidities for the curves in Figure 6.7 indicate that nucleonic particles below about 350 MV cannot penetrate the total amount of matter between the lower bulkhead and the first counter (D1). Hence in the rigidity intervals 50-100 and 100-200 MV, the nucleonic

TABLE 6.3

RANGES OF PROTONS AND ELECTRONS IN LEAD

Rigidity (MV)	PROTONS Kinetic Energy (MeV)	PROTONS Range (g cm^{-2})	ELECTRONS Kinetic Energy (MeV)	ELECTRONS Range* (g cm^{-2})
50	1.33	<.03	49.5	14.2
100	5.31	0.1	99.5	18.5
200	21.1	1.2	~200	22.9
300	46.8	4.7	~300	25.4
400	81.7	12.0	~400	27.2
500	125	25.5	~500	28.7
600	175	42.9	~600	29.9
800	295	101	~800	31.7

* Average range (subject to strong fluctuations, includes radiative and ionization losses)

contamination may be removed by rejecting only those events with pulse heights in the noise levels (see Section G of Chapter V) in both counters. Figure 6.8, which shows the pulse height distributions for the two counters accumulated throughout flight 72L2, confirms that these noise-level pulses are well separated from the minimum-ionizing peaks in both D1 and D2. The presence of a detectable nucleonic contamination in these rigidity intervals at float depths is indicated by the separate pulse height distributions of the positive and negative particle events within each interval (Figures 6.9-6.12).

Since the threshold rigidity for penetration into D2 is about 440 MV, the contamination in the 200-400 MV interval (shown by the pulse height distributions in Figures 6.13-6.14) may be eliminated by excluding events with noise-level pulse heights ir the second counter. The possible residual contamination due to the finite rigidity resolution of the detector (which is uncalibrated above 140 MV) is almost certainly negligible compared to the statistical uncertainties of the flight data.

The 400-800 MV interval is the only one obviously requiring more stringent restrictions, since within this range protons may penetrate both scintillators and deposit energies equivalent to several minimum-ionizing particles in each counter. However, as shown in Figure 6.7 those protons which penetrate into D2 cannot produce more than about 6.0 times minimum-ionizing pulses in D1. Hence it is possible to remove the contamination between 400-800 MV (see Figures 6.15-6.16) by selecting only events with pulse heights above this value in D1 and above noise levels in D2.

These guidelines have been used in arriving at the set of pulse height selection criteria described in Table 6.4. The fractions of events rejected in each negative rigidity interval on the basis of these criteria have been listed in Tables 6.5-6.8, which present the results of imposing these criteria over each interval.

The first two classes of events in each table demonstrate that any contamination by pions or muons may in fact be neglected. Class A events have not been subjected to any pulse height restrictions, while class B events have been obtained by rejecting only those events with minimum-ionizing pulse heights in both cojnters D1 and D2. The small percentages of events rejected on this basis (which should include a major fraction of

pions or muons in the range 50-800 MV) is consistent with the percentages of negatrons rejected by imposing the same criteria on calibration data below 140 MV, as shown in Table 6.9.

For each relevant class of events, Tables 6.5-6.8 include lists of counting rates for positive and negative particles at float altitudes. For the higher rigidities in particular, the reduction in the positive counting rate due to the pulse height restrictions is obviously more pronounced than that for the corresponding negative rates. The positive excess in the counting rates and in the pulse height distributions are roughly consistent with the chance coincidence triggering rate deduced from the observed output rates of the Cerenkov counter discriminator and the $S1 \cdot \overline{A1} \cdot \overline{A2} \cdot S2$ coincidence circuit, which is about 5×10^{-3} s^{-1}.

Tables 6.5-6.8 also indicate the estimated positive fractions for both the primary and atmospheric secondary electron intensities (the latter at a depth of 2 g cm^{-2}), derived from the intensities of each restricted class of events. The corresponding atmospheric growth curves from which these values were derived are shown in Figures 6.17-6.24.

In Figure 6.25 the present estimate for the positive fraction of secondary electrons at 2 g cm^{-2} are compared with previous observations by Beuermann et al. (1970). Note that the two sets of measurements have been derived using atmospheric growth curves of identical shape. Also shown are the nominal predicted curves for the secondary positive fraction given by Beuermann (1971) and Daniel and Stephens (1973). Here uncertainties of roughly 15 per cent have been estimated by the authors in each case. As shown in this figure, the present data has been re-analyzed using the growth curves of Daniel and Stephens (1973) and has been found on this basis to agree with their own assumed values of the positive

fraction. This result is not unexpected, since the separation of primary and secondary electrons of either charge depends on the assumed form of the depth dependence curve in each case.

The present estimates or upper limits for the positive fraction of primary electrons in each rigidity interval represent a compromise between the requirements of statistical reliability and the elimination of significant nucleonic contamination. In this context it has been noted that demanding large pulse heights in the shower counters may be expected to bias the selection of electrons toward the high end of the spectrum contained within each rigidity interval. Estimates of the positive fraction may be sensitive to such biasing effects, since the decrease of this quantity with increasing energy is apparently significant in the range of interest.

TABLE 6.4

PULSE HEIGHT SELECTION CRITERIA

EVENT CLASS	RESTRICTIONS
A	None
B	Reject if $22 \leq D1 \leq 50$ and $40 \leq D2 \leq 70$.
C	Reject if $D1 \leq 22$ and $D2 \leq 20$.
D	Reject if $D2 \leq 20$.
E	Reject if $D1 \leq 22$ or $D2 \leq 20$.
F	Reject if $D1 \leq 50$ or $D2 \lesseqgtr 70$.
G	Reject if $D1 \leq 110$ or $D2 \leq 25$.
H	Reject if $D1 \leq 120$ or $D2 \leq 25$

TABLE 6.9

FRACTION OF ACCEPTED NEGATRONS (CALIBRATION DATA)

Class	Energy (MeV) 50	Energy (MeV) 75	Energy (MeV) 100	Energy (MeV) 140
A	1.0	1.0	1.0	1.0
B	.96 ± .09	.97 .07	.92 .03	.93 .03
C	.83 .08	.94 .04	.97 .04	.97 .03
D	.47 .06	.64 .05	.74 .04	.79 .03
E	.32 .05	.54 .05	.62 .03	.70 .02
F	.0	.07 .02	.08 .01	.15 .01
G	.0	.02 .02	.03 .01	.04 .01
H	.0	.0	.0	.0

TABLE 6.5
50 - 100 MV

EVENT CLASS	FRACTION OF ACCEPTED NEG. EVENTS (FLIGHT)	NEG. COUNTING RATE (FLOAT) $\times 10^{-3}\ s^{-1}$	POS. COUNTING RATE (FLOAT) $\times 10^{-3}\ s^{-1}$	$\left(\frac{N_p^-}{N_p^- + N_s^-}\right)^*$	$\left(\frac{N_p^+}{N_p^+ + N_s^+}\right)^{**}$	$\left(\frac{N_p^+}{N_p^+ + N_p^-}\right)^\dagger$	$\left(\frac{N_s^+}{N_s^+ + N_s^-}\right)^{\dagger\dagger}$
A	1.0	4.2 ±0.5	4.7 ± 0.5	.50 ±0.8	.51 ±.12	.40 ±.14	.56 ±.05
B	.96 ±.04						
C	.86 ±.04	3.6 ± 0.4	3.7 ± 0.4	.49 ±.09	.25 ±.14	.32 ±.18	.57 ±.05

* EST. PRIMARY FRACTION AT 2 G CM^{-2} (NEG.)

** EST. PRIMARY FRACTION AT 2 G CM^{-2} (POS.)

† POS. FRACTION (PRIM)

†† POS. FRACTION (SEC), 2 G CM^{-2}

Table 6.5 -- Results of imposing pulse height selection criteria on 50 - 100 MV particles (for description of event class labels, see Table 6.4)

TABLE 6.6
100 - 200 MV

EVENT CLASS	FRACTION OF ACCEPTED NEG. EVENTS (FLIGHT)	NEG. COUNTING RATE (FLOAT) $\times 10^{-3}\ s^{-1}$	POS. COUNTING RATE (FLOAT) $\times 10^{-3}\ s^{-1}$	$\left(\frac{N_P^-}{N_P^- + N_S^-}\right)^*$	$\left(\frac{N_P^+}{N_P^+ + N_S^+}\right)^{**}$	$\left(\frac{N_P^+}{N_P^+ + N_P^-}\right)^{\dagger}$	$\left(\frac{N_S^+}{N_S^+ + N_S^-}\right)^{\dagger\dagger}$
A	1.0	4.1 ± 0.5	4.3 ± 0.5	.47 ± .10	.32 ± .12	.43 ± .16	.55 ± .05
B	.94 ± .04						
C	.96 ± .04	3.7 ± 0.4	3.3 ± 0.4	.39 ± .10	.22 ± .14	.30 ± .20	.53 ± .05

* EST. PRIMARY FRACTION AT 2 G CM^{-2} (NEG.)

** EST. PRIMARY FRACTION AT 2 G CM^{-2} (POS.)

† POS. FRACTION (PRIM)

†† POS. FRACTION (SEC), 2 G CM^{-2}

Table 6.6 -- Results of imposing pulse height selection criteria on 100 - 200 MV particles (for description of event class labels, see Table 6.4)

TABLE 6.7
200 - 400 MV

EVENT CLASS	FRACTION OF ACCEPTED NEG. EVENTS (FLIGHT)	NEG. COUNTING RATE (FLOAT) $\times 10^{-3}$ s^{-1}	POS. COUNTING RATE (FLOAT) $\times 10^{-3}$ s^{-1}	$\left(\frac{N_P^-}{N_P^- + N_S^-}\right)^*$	$\left(\frac{N_P^+}{N_P^+ + N_S^+}\right)^{**}$	$\left(\frac{N_P^+}{N_P^+ + N_P^-}\right)^\dagger$	$\left(\frac{N_S^+}{N_S^+ + N_S^-}\right)^{\dagger\dagger}$
A	1.0	6.0 ± 0.6	6.1 ± 0.6	.81 ± .04	.76 ± .07	.44 ± .06	.51 ± .10
B	.96 ± .04						
C	.97 ± .04	5.8 ± 0.6	4.4 ± 0.5	.90 ± .05	.60 ± .07	.35 ± .07	.77 ± .11
D	.86 ± .04	5.0 ± 0.5	3.4 ± 0.4	.80 ± .04	.56 ± .11	.28 ± .08	.55 ± .08
E	.80 ± .04	4.6 ± 0.5	3.2 ± 0.4	.80 ± .04	.50 ± .10	.27 ± .08	.60 ± .07
F	.45 ± .03	3.1 ± 0.4	1.6 ± 0.3	.86 ± .05	.48 ± .15	.21 ± .09	.60 ± .10

Table 6.7 -- Results of imposing pulse height selection criteria on 200 - 400 MV particles (for description of event class labels, see Table 6.4)

* EST. PRIMARY FRACTION AT 2 G CM^{-2} (NEG.)

** EST. PRIMARY FRACTION AT 2 G CM^{-2} (POS.)

† POS. FRACTION (PRIM)

†† POS. FRACTION (SEC), 2 G CM^{-2}

TABLE 6.8
400 - 800 MV

EVENT CLASS	FRACTION OF ACCEPTED NEG. EVENTS (FLIGHT)	NEG. COUNTING RATE (FLOAT) $\times 10^{-3}\ s^{-1}$	POS. COUNTING RATE (FLOAT) $\times 10^{-3}\ s^{-1}$	$\left(\frac{N_P^-}{N_P^- + N_S^-}\right)^*$	$\left(\frac{N_P^+}{N_P^+ + N_S^+}\right)^{**}$	$\left(\frac{N_P^+}{N_P^+ + N_P^-}\right)^{\dagger}$	$\left(\frac{N_S^+}{N_S^+ + N_S^-}\right)^{\dagger\dagger}$
A	1.0	11.2 ± 0.8	7.2 ± 0.6	.94 ± .02	.90 ± .03	.43 ± .04	.59 ± .11
B	.97 ± .04						
G	.30 ± .02	3.6 ± 0.4	0.5 ± 0.2	.95 ± .02	.72 ± .13	.14 ± .06	.53 ± .17
H	.06 ± .01	0.8 ± 0.2	< 0.1	———	———	———	———

* EST. PRIMARY FRACTION AT 2 G CM^{-2} (NEG.)

** EST. PRIMARY FRACTION AT 2 G CM^{-2} (POS.)

† POS. FRACTION (PRIM)

†† POS. FRACTION (SEC), 2 G CM^{-2}

Table 6.8 -- Results of imposing pulse height selection criteria on 400 - 800 MV particles (for description of event class labels, see Table 6.4)

H. Energy Losses in the Detector and the Overlying Atmosphere

Downward-moving particles incident on the detector must pass through a total of about .06 radiation lengths of material (of which .03 radiation lengths is aluminum) before entering the magnet gap region. In addition, an atmospheric float depth of 2 g cm^{-2} leaves about .05 radiation lengths of air separating the top of the detector from the interplanetary environment. The total depth of intervening matter results in a corresponding average energy degradation of the interplanetary electrons observed in the detector. Hence the spectrum measured by the instrument is in general slightly distorted from its form in the interplanetary medium.

The distortion over any small region ΔE of the electron spectrum centered on energy E is dependent both on the atmospheric depth and the shape of the interplanetary spectrum at energies $E' > E$. To evaluate these effects, let $j(E,t)$ denote the spectrum at a depth of t radiation lengths, and let $\varphi(E,E',t)dE$ give the probability that an electron with initial energy E' will have an energy in the range E to $E+dE$ at depth t. Then $j(E,t)$ is related to the interplanetary spectrum $j(E,0)$ by the expression

$$j(E,t) = \int_E^\infty dE' \varphi(E,E',t) j(E',0) \qquad 6.15$$

An expression for φ due to Bethe and Heitler (1934) may be written as

$$\varphi(E,E',t) = \frac{1}{E'} \frac{\left[\ln\left(\frac{E'}{E}\right)\right]^{\frac{t}{\ln 2}-1}}{\Gamma\left(\frac{t}{\ln 2}\right)} \qquad 6.16$$

(see also Rossi, 1952). If this value for φ is inserted into equation 6.15 and a power law form $J(E,0) = KE^{-\gamma}$ (with spectral index $\gamma > 1$) is assumed for the interplanetary spectrum, equation 6.15 may be integrated analytically (Schmidt, 1972) to give the simple result

$$J(E,t) = \gamma^{-\frac{t}{\lambda_{n2}}} J(E,0) \qquad 6.17$$

This analytic solution has proved useful in performing numerical integrations of equation 6.15 for interplanetary spectra of arbitrary shape (see Appendix B). The numerical solutions have been used to trace the distortion of specified interplanetary spectra through several atmospheric depths ranging up to 40 g cm^{-2}, as shown by the example in Figure 6.26. The additional material present in the upper half of the detector has been taken into account in each case.

The assumed interplanetary spectrum in Figure 6.26 has been drawn through the points initially obtained for the primary negatron spectrum without consideration of bremsstrahlung losses. The separation of primary and atmospheric secondary components over each energy interval of this initial spectrum was accomplished assuming a flat primary depth dependence, $p^{(o)}(x) = 1$. The series of distorted spectra obtained in Figure 6.26 have then provided first approximations for $p(x)$ in each energy interval, as shown in Figure 6.27.

Even for the 100-200 MV interval, however, these estimates for $p(x)$ have not resulted in significant revisions of the initial fits to the depth dependence curves. Furthermore, the small probably distortion of the interplanetary spectrum at a depth of 2 g cm^{-2} is insignificant compared to the uncertainties in the initial estimates of the measured

spectrum or its possible extrapolations at higher energies. Since a reliable estimate of the spectral distortion requires a more accurate knowledge of the spectrum measured at the detector, no further attempt has been made here to correct the measured negatron or positron spectra for radiative losses at this atmospheric depth.

It should also be noted that non-radiative (collision) losses in the atmosphere and the detector amount to about 8 MeV throughout the range 50-800 MeV. This loss has been taken into account by a constant 8-MeV shift of the energy intervals in the primary spectra.

CHAPTER VII

RESULTS AND INTERPRETATION

The energy dependence of the positive fraction $\frac{N_{e^+}}{N_{e^+} + N_{e^-}}$ in primary cosmic ray electrons between 50 and 800 MeV is shown in Figure 7.1. The earlier results obtained by Fanselow et al. (1969) over the same energy range have been included for comparison. The present measurements of the primary negatron intensities, which have been derived from the depth dependence curves shown in Figures 6.3-6.6, have been combined with the corresponding values of the positive fraction to infer the primary positron intensities (shown in Figure 7.2) as well as the total electron spectrum (Figure 7.3).

As discussed in Section F.3 of Chapter VI, the primary negatron and positron intensities found in this analysis have been derived using the depth dependence curves for atmospheric secondary electrons given by Beuermann (1971). It has already been noted in the same discussion that at energies below about 200 MeV, the use of recent atmospheric secondary calculations by Daniel and Stephens (1973) leads to primary negatron intensities which are about a factor of 1.4 higher than the results found in the present analysis. (For a comparison of the basic assumptions entering both of these calculations, see Section F.3 of Chapter VI.) These differences are still comparable to the statistical uncertainties in the present data, but they may prove important in future measurements. However, above 200-300 MeV the differences in the calculated depth dependence

curves become less significant (since the contamination due to secondary electrons is considerably reduced). Furthermore, both calculations lead to essentially similar results for the primary positron intensities at all energies of interest.

Independent measurements reported by Webber et al. (1973) and by Fulks et al.,(1973) for the total electron intensities in 1972 have also been included in Figure 7.3. Significant disagreements are apparent in these measurements. While the OGO-5 satellite results are lower than the other estimates below 20 MeV, the intensities found in the present experiment are nearly a factor of two higher than the other balloon measurements above 200 MeV (and apparently in the range 50-100 MeV as well). The difference does not appear to result from dissimilar solar or geomagnetic conditions, since all three balloon experiments were flown from Fort Churchill during the period July-August, 1972. Neither brief solar disturbances or significant slower variations in neutron monitor counting levels were recorded during any of these flights. It seems more likely that the disagreement arises either from the significant differences in experimental technique, or procedures followed in the analysis of flight data.

The values found for the interplanetary positron and total electron spectra in the present experiment have been consistently related to independent estimates of the corresponding intensities in interstellar space. Section A below compares the present results with numerical solutions of the spherically symmetric transport equation (4.7) describing the solar modulation of the calculated interstellar (galactic secondary) positron spectrum and the (secondary plus primary) electron spectrum inferred from observations of diffuse galactic radio emission.

The concluding section discusses the significant value in further measurements of the separate positron and negatron spectra below 1 GeV as well as at higher energies. In this context, the strong possibility of obtaining considerably more accurate results with the present detector system is emphasized.

A. Solar Modulation and Interstellar Spectra

The measurements of the separate cosmic ray positron and negatron intensities have demonstrated that, at least between a few hundred MeV and several GeV, most of the electrons reaching the earth from primary galactic sources are negatrons. Furthermore, at all energies above a few MeV the (modulated) positron intensities observed near the earth are consistently lower than the calculated interstellar spectra of galactic secondary electrons arising from $\pi \rightarrow \mu \rightarrow e$ decays (Ramaty, 1973). While these facts do not by themselves exclude the possibility that positrons may be created and accelerated by some primary sources (see for example the model of pulsars suggested by Sturrock, 1971), it is generally considered likely that the positron component above a few MeV is entirely attributable to the interstellar nuclear collisions described in Chapter II.

If this assumption is valid, comparisons of measured positron intensities with the calculated galactic secondary positron spectrum may provide the most reliable measure of the absolute modulation of interstellar cosmic rays at a given epoch in the solar cycle. Although the positron measurements are in general more difficult than the observations of nucleonic cosmic rays, at present there is no reliable way to determine the interstellar spectra of nucleonic particles at the energies susceptible to significant modulation. To a lesser extent the modulation of the total positive and negative) electron component is also subject to considerable uncertainties, since the available estimates of the interstellar electron spectrum based on nonthermal radio observations (Goldstein et al., 1970; Cummings et al., 1973b) extend only from about 200 MeV to several GeV. Even in this range the estimates are probably uncertain by at least a

factor of four (Cummings et al., 1973b). However, from current knowledge of nuclear interactions and conditions in galactic space the positron spectrum from interstellar $\pi \rightarrow \mu \rightarrow e$ decays is probably known to within a factor of two at all experimentally accessible energies above a few MeV. (It is reasonable to expect that an increasing knowledge of hadronic collisions and the galactic environment will further improve the accuracy of the calculated positron spectrum.) Hence the absolute modulation of the positron spectrum over this entire range of energies may be estimated with comparative accuracy.

It is obvious that a quantitative test of the hypothesis that the positrons throughout this range are indeed predominantly of secondary origin would be of great significance. One method of testing this assumption is that of comparing the modulation of both the positron and total electron components at given epochs in the solar cycle (Ramaty, 1973; Cummings et al., 1973a). The present measurements of positrons and negatrons between 50 and 800 MeV have provided the basis for such a comparison, which has here been made in the context of the spherically symmetric model of the solar wind (see the discussion in Chapter IV).

The complete interplanetary transport equation (4.7), including the energy loss term, has been integrated numerically by the technique due to Fisk (1971) with the aim of finding a single diffusion coefficient which can relate both the positron and total electron observations to assumed interstellar spectra of the forms given by Goldstein et al. (1970) and Ramaty (1973) respectively. It has been found that a diffusion coefficient of the form

$$K(r,\rho) = \beta K_1(r) K_2(\rho) ,$$

$$K_1(r) = \frac{1+r'}{1+r'^2}, \quad r' \equiv \frac{r}{r_0}$$

$$K_2(\rho) = \begin{cases} 100 V r_0 \rho, & \rho > .25 \text{ GV} \\ 25 V r_0, & .05 \text{ GV} < \rho < .25 \text{ GV} \end{cases}$$

(where V = 400 km s^{-1} is the assumed solar wind speed and r_0 = 1 AU) and a boundary of 10 AU for the modulating region give a consistent description of the modulation of both spectra down to 50 MeV as shown in Figures 7.2 and 7.3.

In order to match the available positron observations near 1 GeV to the spectrum calculated by Ramaty (1973), the interstellar electron spectrum assumed here (curve A in Figure 7.3) has been lowered slightly compared to the nominal values given by Goldstein et al. (1970) or Cummings et al. (1973b). However, this assumed spectrum is entirely consistent with the uncertainties estimated by these authors. In any case a comparable if somewhat smaller uncertainty exists in the calculations of the positron spectrum (Ramaty, 1973).

It should also be noted that the form of the electron spectrum adopted here obeys a simple power law with spectral index 1.8 at energies below 2 GeV. No attempt has been made to incorporate a flattening of the spectrum below about 100 MeV, as postulated by Cummings et al. (1973a) to account for the lower energy positron measurements of Beuermann et al. (1970) within the context of the spherically symmetric model of solar modulation. At present it seems likely that the relationship between the interstellar and modulated spectra may ultimately be understood in terms of models which depart from spherical symmetry and permit easy access of

low-energy particles to the inner solar system (Fisk et al., 1973b).

In the present analysis, the diffusion coefficient K has been chosen primarily to fit the shape of the modulated total electron spectrum, since the statistical uncertainties in the positron measurements are considerably greater. However, the resulting fit to the positron measurements in Figure 7.2 is obviously consistent with the assumption of a purely secondary origin for the positron component over this entire range of energies.

B. Conclusion

The present measurements of cosmic ray positrons and negatrons have confirmed the results of previous experiments by Hartman (1967) and Fanselow et al. (1969), which demonstrated the existence of a dominant primary negatron component in the interstellar electron spectrum above a few hundred MeV. In addition, finite estimates or upper limits have been established for the interplanetary positron and negatron spectra between 50 and 800 MeV.

From a comparison of the measured intensities with independent estimates of the total interstellar electron spectrum (based on radio observations) and the interstellar positron spectrum resulting from $\pi \rightarrow \mu \rightarrow e$ decays in the galaxy, consistent parameters have been found to describe the solar modulation of both the positron and total electron intensities in 1972. Hence the positron measurements have been shown to be consistent with the hypothesis of a predominantly secondary origin for the positron component at energies from 50 to 800 MeV.

Further results of great value may be expected from future observations of cosmic ray positrons and negatrons below 1 GeV, as well as at higher energies. In addition to accumulating further significant information on the origins of galactic positrons and negatrons, such experiments can provide valuable constraints on the theory of solar modulation. Measurements of improved statistical accuracy might be used to monitor temporal variations in the positive fraction $\frac{N_{e^+}}{N_{e^+} \quad N_{e^-}}$ as a function of energy. These observations may provide the most reliable measure of the adiabatic energy losses suffered by galactic cosmic rays penetrating the solar cavity. Finally, more precise estimates of the separate positron and negatron spectra may furnish new information on the interesting

behavior of the interstellar electron spectra at energies below 100 MeV.

In this context, it should be noted that the magnetic spectrometer which has obtained the measurements reported here may be expected to obtain results of considerably improved statistical accuracy in forthcoming flights. It is hoped that the significant improvements made in the detector system since the 1972 flights will ultimately permit accurate measurements of cosmic ray positron and negatron spectra over several epochs of the solar cycle.

APPENDIX A

ANALYSIS OF THE GAS CERENKOV COUNTER DETECTION EFFICIENCY

An electron traversing a length $\Delta\ell$ in the radiating medium of the Cerenkov counter emits an average number of photons between two wavelengths λ_1 and λ_2 which is given approximately by (Jelley, 1958)

$$\Delta n_\gamma = 2\pi\alpha\,\Delta\ell\left(\frac{1}{\lambda_2}-\frac{1}{\lambda_1}\right)\left(1-\frac{1}{\beta^2 n^2}\right)$$

The range of wavelengths for which equation A.1 is valid includes the entire response range of the Amperex 60DVP phototubes, which extends from about 6100 Å to about 2800 Å in the ultraviolet (see Figure A.3). For all the gases of interest here (carbon dioxide, air, and Freon-12), the refractive index n is essentially independent of wavelength in this range. Hence the spectral distribution of the photons emitted by electrons of arbitrary energy is proportional to $\frac{1}{\lambda^2}$.

An isotropic flux of electrons incident on the detector determines the distribution of path lengths traversed by those particles which satisfy the telescope coincidence criterion $S1\cdot\overline{A1}\cdot\overline{A2}\cdot S2$. An approximate form for this distribution, obtained from the Monte Carlo calculation described in Section B of Chapter V, is shown in Figure A.1. The peak is sufficiently narrow that in a first approximation it may be replaced by a delta function about the average value $\bar{\ell} = 71$ cm. The path length distribution of the electrons in an accelerator beam used for calibration of the detection efficiency is even more accurately described by

such an approximation, although the measured efficiency in a nondispersive beam at a given energy may vary by as much as 20 percent depending on the detector alignment.

The probability of reflection (or absorption) of a single photon incident on the mirror surface depends in general on its wavelength, angle of incidence, and polarization. (The polarization vector of Cerenkov light is everywhere perpendicular to the conical surface which defines the direction of the radiation from any point along the electron trajectory.) Figure A.2(a) shows that the reflectivity R_o at normal incidence on an opaque vapor-deposited aluminum film has a nearly constant value of 0.9 over the phototube response range. The changes in the reflectivity with increasing angles of incidence for photons polarized parallel and perpendicular to the plane of incidence is shown in Figure A.2(b). However, since the angles between acceptable electron trajectories and the mirror normal cannot exceed about 30 degrees (and the maximum half-angle of the cone of radiation is less than 2 degrees for carbon dioxide at 1 atm), the variation in R for photons of either polarization is less than 5 percent.

Table A.1 indicates that the absorption of emitted photons in either carbon dioxide, air, or Freon-12 is negligible over the phototube response range. The placement of the mirrors, the large photocathode surface (400 cm^2), and the high transparency of the glass tube face further insure that more than 95 percent of the reflected photons reach one of the photocathodes. Hence for each acceptable electron the average total number of photons incident on a tube cathode is approximately given by $\bar{n}_\gamma = \frac{\Delta n_\gamma}{\Delta \ell} \bar{\ell} R_o$, which for carbon dioxide at 1 atm has a maximum value of about 50 between the limiting wavelengths of 2800 Å

and 6100 Å. The fluctuations about this average number are governed by fluctuations in the photon production rate (which presumably obey Poisson statistics) as well as the electron path length and the probability of reflection for the individual photons in each pulse. However, the quantum efficiency of the phototubes (shown in Figure A.3) is sufficiently low that these fluctuations are dominated by fluctuations in the number of ejected cathode photoelectrons. Here it will be assumed that the probability of ejecting n_e photoelectrons from the cathode by a pulse of $\bar{n}_\gamma$ photons may itself be approximated by a Poisson distribution about an average number $\bar{n}_e$. This probability will be written as $P_1(\bar{n}_e, n_e)$. The values of $\bar{n}_e$ for specific choices of the electron Lorentz factor γ_e and the radiating medium, have been provided by the Monte Carlo calculation described in Section B of Chapter V. (For carbon dioxide, $\bar{n}_e \leq 7$.)

The probability that n_e cathode photoelectrons will result in a discriminator output pulse when the threshold level corresponds to an average number n_{th} will be denoted by $P_2(n_e, n_{th})$. A first approximation for P_2 (which ignores the fluctuations in the gain at each dynode) is the step function $\theta(n_e - n_{th})$, where

$$\theta(x) = 0, \quad x < 0$$
$$= 1, \quad x \geq 0$$

With these assumptions the detection efficiency ε_c of the Cerenkov counter is approximated by the expression

$$\varepsilon_c(\gamma_e) = \sum_{n_e} P_1[\bar{n}_e(\gamma_e), n_e] P_2(n_e, n_{th})$$
$$= 1 - \sum_{n_e < n_{th}} \frac{e^{-\bar{n}_e} \bar{n}_e^{n_e}}{n_e!}$$

The range $4 < n_{th} < 5$ has been found to give reasonable agreement with measured values for the detection efficiency with air as the radiating medium (see Figure 5.2). However, the corresponding values for carbon dioxide lie considerably lower than the curve predicted by the same analysis. Even if light-absorbing contaminants were present in the gas, the data could not be fit to a single curve. The discrepancy is partially attributed to an improper (and possibly varying) alignment of the detector during the measurements with carbon dioxide.

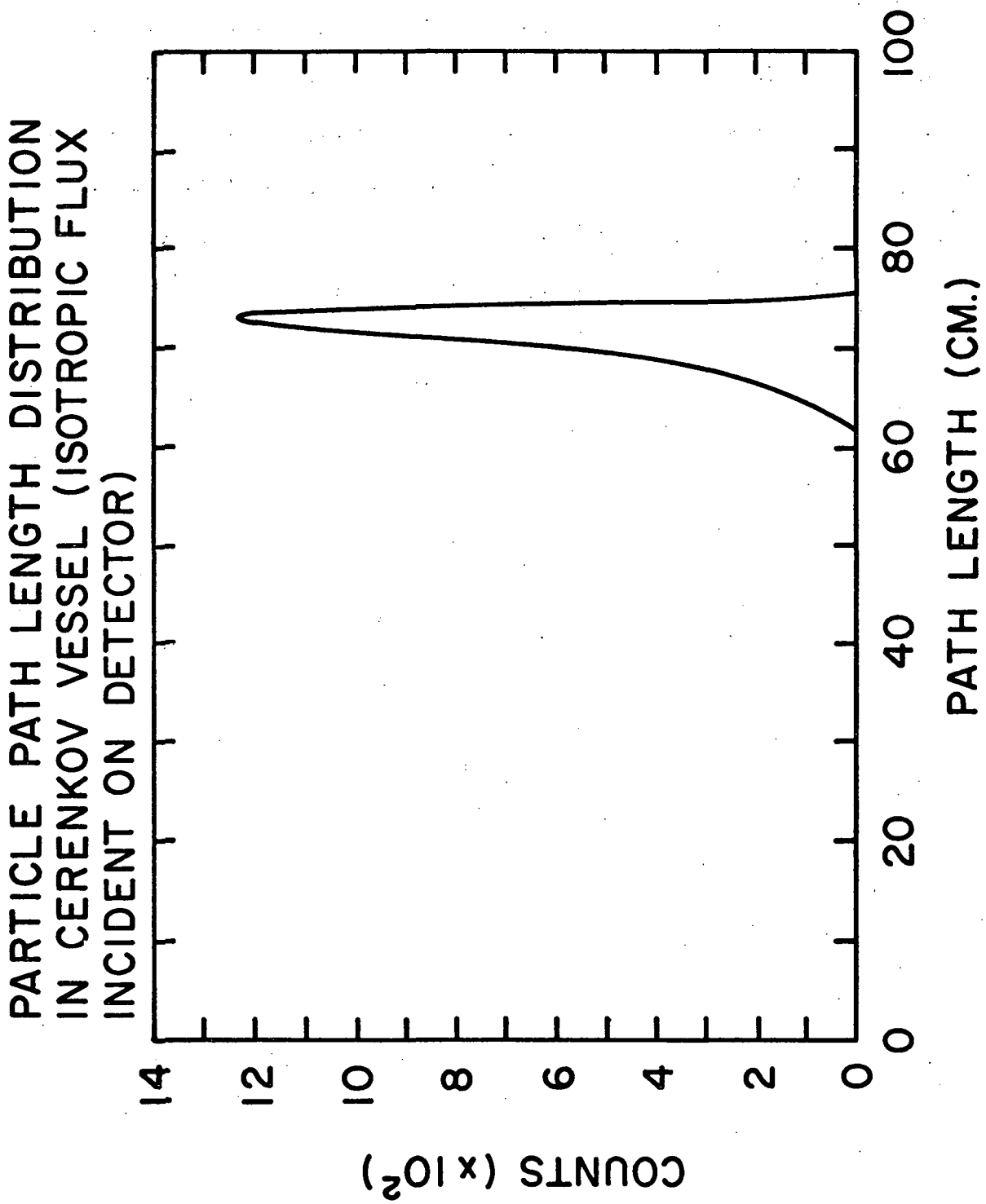

Figure A.1 -- Particle path length distribution in Cerenkov vessel for isotropic flux incident on detector.

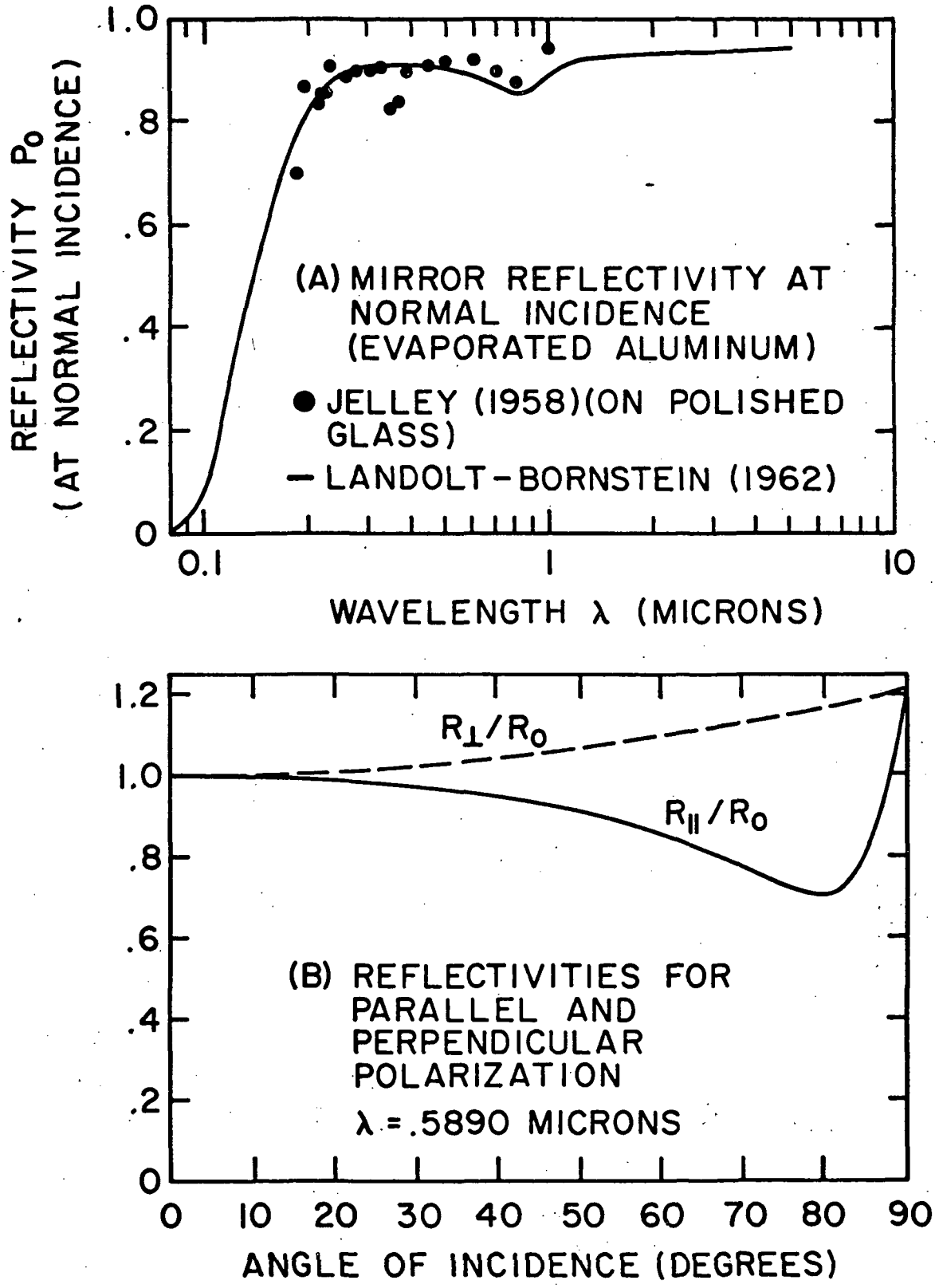

Figure A.2 -- Reflectivity of Cerenkov counter mirrors.

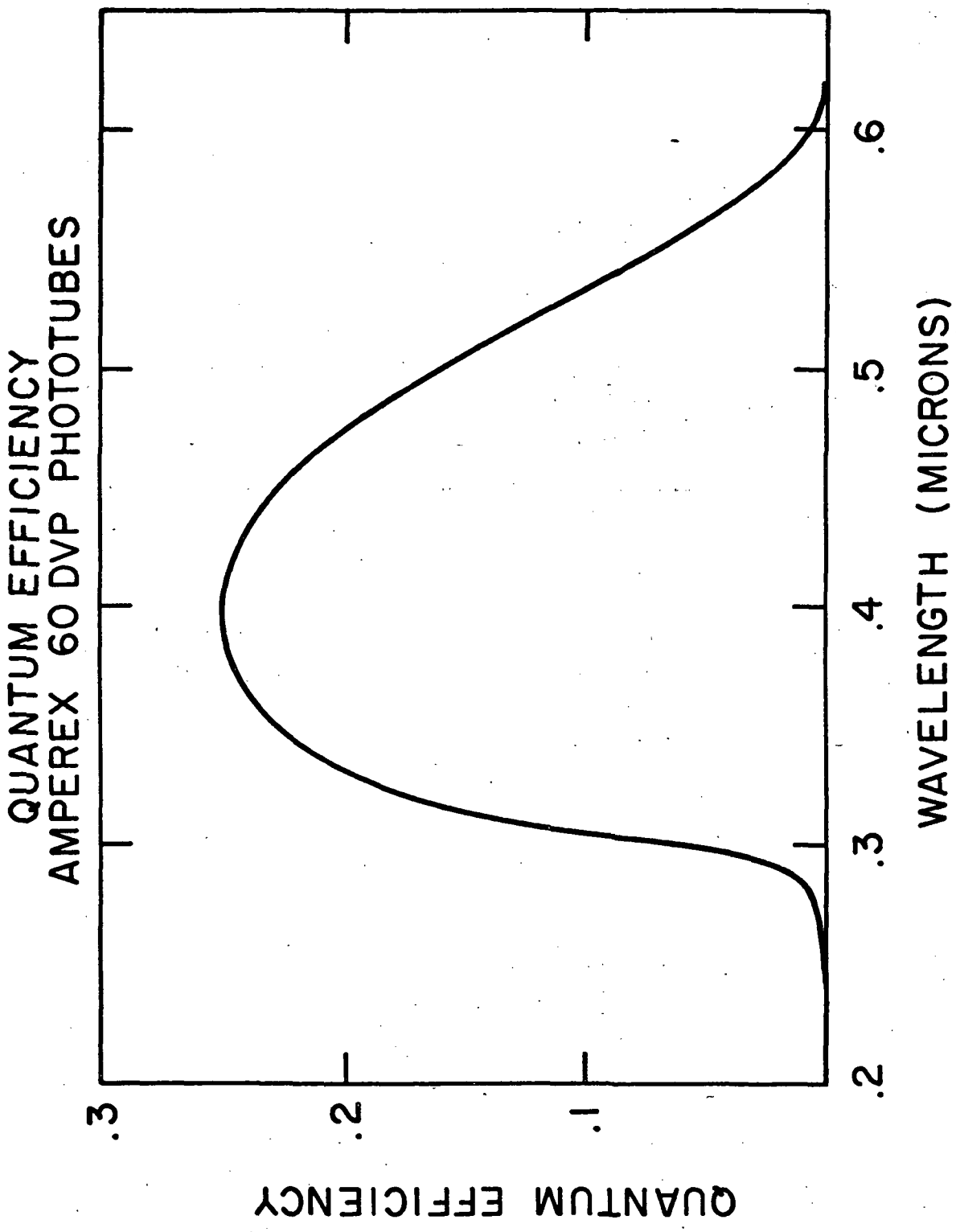

Figure A.3 -- Quantum efficiency of Amperex 60DVP phototubes.

APPENDIX B

NUMERICAL CALCULATION OF BREMSSTRAHLUNG LOSSES IN THE DETECTOR AND THE OVERLYING ATMOSPHERE

The integrand in the equation

$$\mathcal{J}(E,t) = \int_E^\infty dE' \varphi(E,E',t)\mathcal{J}(E',0) = \int_E^\infty \frac{dE'}{E'} \frac{\left[\ln\left(\frac{E'}{E}\right)\right]^{\frac{t}{\ln 2}-1}}{\Gamma\left(\frac{t}{\ln 2}\right)} \mathcal{J}(E',0) \qquad \text{C.1}$$

is singular at the lower limit of integration for penetration depths t (expressed in radiation lengths) less than ln 2. However, the singularity may be avoided in numerical integrations of equation C.1 by taking advantage of the analytic solution for the case of a power law spectrum $\mathcal{J}_{PL}(E,0) = KE^{-\gamma}$ (where $\gamma > 1$), which is given simply by

$$\mathcal{J}_{PL}(E,t) = \gamma^{-\frac{t}{\ln 2}} \mathcal{J}_{PL}(E,0) \qquad \text{(Schmidt, 1972).}$$

Let $\mathcal{J}(E',0)$ denote the assumed interplanetary spectrum to be inserted in C.1 and let $\mathcal{J}_{PL}(E,0) = KE^{-\gamma} \equiv \mathcal{J}(E,0)$, where γ is chosen so that $\mathcal{J}_{PL}(E',0) \simeq \mathcal{J}(E',0)$ for all energies E' between E and E+ΔE. Then

$$\mathcal{J}(E,t) \simeq \int_E^{E+\Delta E} dE' \varphi(E,E',t)\mathcal{J}_{PL}(E',0) + \int_{E+\Delta E}^\infty dE' \varphi(E,E',t)\mathcal{J}(E',0) \qquad \text{C.2}$$

The second terms on the right hand side of both C.2 and the equation

$$\mathcal{J}_{PL}(E,t) = \int_E^{E+\Delta E} dE' \varphi(E,E',t)\mathcal{J}_{PL}(E',0) + \int_{E+\Delta E}^\infty dE' \varphi(E,E',t)\mathcal{J}_{PL}(E',0) \qquad \text{C.3}$$

may be integrated numerically using standard techniques (for example, straightforward step-by-step integration). Since the left side of C.3 is given by the analytic solution stated above, the solution of C.2 is known to be an accuracy determined by the choices for ΔE and γ.

REFERENCES

Abraham, P. B., Brunstein, K. A., and Cline, T. L., Phys. Rev. 150, 1088, 1966.

Agrinier, B., Koechlin, Y., Parlier, B., Vasseur, J., Bland, C. J., Boella, G., Degli Antoni, G., Dilworth, C., Scarsi, L., and Sironi, G., Proc. Ninth Int. Conf. on Cosmic Rays, London, 1, 331, 1965.

Amati, D., Stanghellini, A., and Fubini, S., Nuovo Cimento 26, 896, 1962.

Ashley, G. K., Elbert, J. W., Keuffel, J. W., Larson, M. O., and Morrison, J. L., Phys. Rev. Letters 31, 1091, 1973.

Bali, N. F., Brown, L. S., Peccei, R. D., and Pignotti, A., Phys. Rev. Letters 25, 557, 1970.

Barkas, W. H., and Berger, M. J., Tables of Energy Losses and Ranges of Heavy Charged Particles, NASA Document SP-3013, 1964.

Beedle, R. E., Lezniak, J. A., Rockstroh, J., and Webber, W. R., Acta Physica Academiae Scientiarum Hungaricae 29, Suppl. 1, 131, 1970.

Berger, M. J., and Seltzer, S. M., Tables of Energy Losses and Ranges of Electrons and Positrons, NASA Document SP-3012, 1964.

Berkey, G. B., and Shen, C. S., Phys. Rev. 188, 1994, 1969.

Bethe, H. A., and Heitler, W., Proc. Roy. Soc. A146, 83, 1934.

Beuermann, K. P., J. Geophys. Res. 76, 4291, 1971.

Beuermann, K. P., Rice, C. J., Stone, E. C., and Vogt, R. E., Phys. Rev. Letters 22, 412, 1969.

Beuermann, K. P., Rice, C. J., Stone, E. C., and Vogt, R. E., Acta Physica Academiae Scientiarum Hungaricae 29, Suppl. 1, 173, 1970.

Bland, C. J., Boella, G., Degli Antoni, G., Dilworth, C., Scarsi, L., Sironi, G., Agrinier, B., Koechlin, Y., Parlier, B., and Vasseur, J., Phys. Rev. Letters 17, 813, 1966.

Bleeker, J. A. M., Burger, J. J., Deerenberg, A. J. M., Scheepmaker, A., Swanenburg, B. N., and Tanaka, Y., Can. J. Phys. 46, S522, 1968.

Buffington, A., Smoot, G. F., Smith, L. H., and Orth, C. D., Proc. Thirteenth Int. Conf. on Cosmic Rays, Denver, Colorado, U. S. A., 1, 318, 1973.

Burger, J. J. and Swanenburg, B. N., Letter submitted to J. Geophys. Res., 1972.

Chandrasekhar, S., Rev. Mod. Phys. 15, 1, 1943.

Choate, L. M., and Wayland, J. R., Astrophys. and Space Sci. 19, 195, 1972.

Cline, T. L., and Hones, E. W., Can. J. Phys. 46, S527, 1968.

Compton, A. H., and Getting, I. A., Phys. Rev. 47, 817, 1935.

Critchfield, C. L., Mey, E. P., and Oleska, S., Phys. Rev. 85, 461, 1952.

Cummings, A. C., Stone, E. C., and Vogt, R. E., Proc. Thirteenth Int. Conf. on Cosmic Rays, Denver, Colorado, U. S. A., 1, 340, 1973a.

Cummings, A. C., Stone, E. C., and Vogt, R. E., Proc. Thirteenth Int. Conf. on Cosmic Rays, Denver, Colorado, U. S. A., 1, 335, 1973b.

Daniel, R. R., and Stephens, S. A., Phys. Rev. Letters 17, 935, 1966.

Daniel, R. R., and Stephens, S. A., Proc. Indian Acad. Sci. 65, 319, 1967.

Daniel, R. R., and Stephens, S. A., Space Science Reviews 10, 599, 1970.

Daniel, R. R., and Stephens, S. A., Preprint, to be published in Reviews of Geophysics and Space Physics, 1973.

Davis, L., and Berge, G. L., Chapter 15, Nebulae and Interstellar Matter, Vol. VII of Stars and Stellar Systems, ed. B. M. Middlehurst and L. H. Aller, University of Chicago Press, 1968.

De Shong, Jr., J. A., Hildebrand, R. H., and Meyer, P., Phys. Rev. Letters 12, 3, 1964.

Dogel, V. A., and Syrovatskii, S. J., Proc. Sixth All-Union Annual Winter School on Cosmic Physics, Apatite (in Russian), 11, 49, 1969.

Dooher, J., Phys. Rev. D 7, 1406, 1973.

Earl, J. A., Phys. Rev. Letters 6, 125, 1961.

Fanselow, J. L., Hartman, R. C., Hildebrand, R. H., and Meyer, P., Ap. J. 158, 771, 1969.

Fermi, E., Phys. Rev. 75, 1169, 1949.

Feynman, R. P., Phys. Rev. Letters 23, 1415, 1969.

Fichtel, C. E., Cline, T. L., and Kniffen, D. A., Bulletin of the American Physical Society, 13, 1410, 1968.

Fisk, L. A., J. Geophys. Res. 76, 221, 1971.

Fisk, L. A., Forman, M. A., and Axford, W. I., J. Geophys. Res. 78, 995, 1973a.

Fisk, L. A., Forman, M. A., and Goldstein, M. L., Proc. Thirteenth Int. Conf. on Cosmic Rays, Denver, Colorado, U. S. A., 2, 771, 1973b.

Fulks, G., Meyer, P., and L'Heureux, J., Proc. Thirteenth Int. Conf. on Cosmic Rays, Denver, Colorado, U. S. A., 2, 753, 1973.

Ginzburg, V. L., Dokl. Akad. Nauk. SSSR 76, 377, 1951.

Ginzburg, V. L., Progress in Elementary Particle and Cosmic Ray Physics, Vol. 4, North-Holland Publishing Co., Amsterdam, 1958.

Gleeson, L. J., and Axford, W. I., Ap. J. 149, L115, 1967.

Gleeson, L. J., and Axford, W. I., Ap. J. 154, 1011, 1968.

Goldstein, M. L., Ramaty, R., and Fisk, L. A., Phys. Rev. Letters 24, 1193, 1970.

Gould, R. J., and Burbidge, G. R., Annales d'Astrophysique 28, 176, 1965.

Greville, E., Computer Sciences Corporation Document 3101-01700-02TM, 1973.

Hartman, R. C., Ap. J. 150, 371, 1967.

Hartman, R. C., Meyer, P., and Hildebrand, R. H., J. Geophys. Res. 70, 2713, 1965.

Hasselmann, K., and Wibberentz, G., Z. Geophys. 34, 353, 1968.

Hayakawa, S., Progr. Theoret. Phys. 8, 571, 1952.

Hayakawa, S., Cosmic Ray Physics, John Wiley and Sons, New York, 1969.

Hayakawa, S., Ito, K., and Terashima, Y., Progr. Theoret. Phys. Suppl. 6, 1, 1958.

Hayakawa, S., and Okuda, H., Progr. Theoret. Phys. 28, 517, 1962.

Hiltner, W. A., Ap. J. Suppl. 2, 389, 1956.

Hovestadt, D., and Meyer, P., Acta Physica Academiae Scientiarum Hungaricae 29, Suppl. 2, 525, 1970.

Hulsizer, R. I., and Rossi, B., Phys. Rev. 73, 1402, 1948.

Israel, M. H., and Vogt, R. E., J. Geophys. Res. 74, 4714, 1969.

Jelley, J. V., Cerenkov Radiation and Its Applications, Pergamon Press, New York, 1958.

Jokipii, J. R., Ap. J. 146, 480, 1966.

Jokipii, J. R., L'Heureux, J., and Meyer, P., J. Geophys. Res. 72, 4375, 1967.

Jokipii, J. R., and Meyer, P., Phys. Rev. Letters 20, 752, 1968.

Jokipii, J. R., and Lerche, I., Ap. J. 157, 1137, 1969.

Jokipii, J. R., and Parker, E. N., Ap. J. 160, 735, 1970.

Jones, F. C., J. Geophys. Res. 68, 4399, 1963.

Jones, F. C., Phys. Rev. D 2, 2787, 1970.

Jones, F. C., Kaiser, J. B., and Birmingham, T. J., Proc. Thirteenth Int. Conf. on Cosmic Rays, Denver, Colorado, U. S. A., 2, 669, 1973.

Kiepenheuer, K. O., Phys. Rev. 79, 738, 1950.

Klimas, A., and Sandri, G., Proc. Thirteenth Int. Conf. on Cosmic Rays, Denver, Colorado, U. S. A., 2, 659, 1973.

Kniffen, D. A., NASA Technical Report TR R-308, 1969.

Kniffen, D. A., Cline, T. L. and Fichtel, C. E., Acta Physica Academiae Scientiarum Hungaricae 29, Suppl. 1, 187, 1970.

Landolt-Bornstein, Zahlenwerte und Funktionen, II Band, 8. Teil, 1-19, Springer-Verlag, 1962.

L'Heureux, J., Ap. J. 148, 399, 1967.

L'Heureux, J., and Meyer, P., Can. J. Phys. 46, 892, 1968.

Longair, M. S., and Sunyaev, R. A., Astrophys. Letters 4, 191, 1969.

MacKeown, P. K., and Wolfendale, A. W., Proc. Phys. Soc. 89, 553, 1966.

Meyer, P., Proc. Twelfth Int. Conf. on Cosmic Rays, Hobart, Tasmania, Australia, Rapporteur Paper, 1971.

Meyer, P., and Vogt, R., Phys. Rev. Letters 6, 193, 1961.

Michel, L., Nature 163, 959, 1949.

Moliere, G. J., Naturforsch. 3(a), 78, 1948.

Parker, E. N., Phys. Rev. 110, 1445, 1958.

Parker, E. N., Interplanetary Dynamical Processes, Interscience, New York, 1963.

Parker, E. N., Planet. Space Sci. 13, 9, 1965.

Parker, E. N., Ap. J. 145, 811, 1966.

Parker, E. N., Proc. Twelfth Int. Conf. on Cosmic Rays, Hobart, Tasmania, Australia, Invited Paper, 1971.

Perola, G. C., and Scarsi, L., Nuovo Cimento 46, 718, 1966.

Perola, G. C., Scarsi, L., and Sironi, G., Nuovo Comento 52B, 455 and 53B, 459, 1967.

Peters, B., Proc. 1962 Conf. on High-Energy Physics at CERN, European Organization for Nuclear Research, Geneva, 623, 1962.

Pollack, J. B., and Fazio, G. G., Ap. J. 141, 730, 1965.

Purcell, E. M., and Spitzer, L., Ap. J. 167, 31, 1971.

Ramaty, R., Private communication, 1973.

Ramaty, R., and Lingenfelter, R. E., J. Geophys, Res. 71, 3687, 1966.

Ramaty, R., and Lingenfelter, R. E., Phys. Rev. Letters 20, 120, 1968.

Raven Industries, Interim Report Number R-0473002, 1973.

Rossi, B., High Energy Particles, Prentice-Hall, New Jersey, 1952.

Scanlon, J. H., and Milford, S. N., Ap. J. 141, 718, 1965.

Schmidt, P. J., J. Geophys. Res. 77, 3295, 1972.

Silverberg, R. F., and Ramaty, R., Nature 243, 134, 1973.

Simnett, G. M., Planet. Space Sci. 17, 1781, 1969.

Stephens, S. A., Ph.D. Thesis, Bombay University, 1969.

Sternheimer, R. M., and Lindenbaum, S. J., Phys. Rev. 123, 333, 1961.

Sturrock, P. A., Ap. J. 164, 529, 1971.

Thompson, D. J., NASA/GSFC Document X-662-73-179, 1973 (unpublished).

Verma, S. D., Proc. Indian Acad. Sci. 66A, 125, 1967.

Verschuur, G. L., Ap. J. 165, 651, 1971.

Webber, W. R., Aust. J. Phys. 21, 845, 1968.

Webber, W. R., and Chotkowski, C., J. Geophys. Res. 72, 2783, 1967.

Webber, W. R., Kish, J., and Rockstroh, J. M., Proc. Thirteenth Int. Conf. on Cosmic Rays, Denver, Colorado, U. S. A., 2, 760, 1973.

Wentzel, D., Ap. J. 152, 987, 1968.

Wilson, K. G., Acta Phys. Austr. 17, 37, 1963.

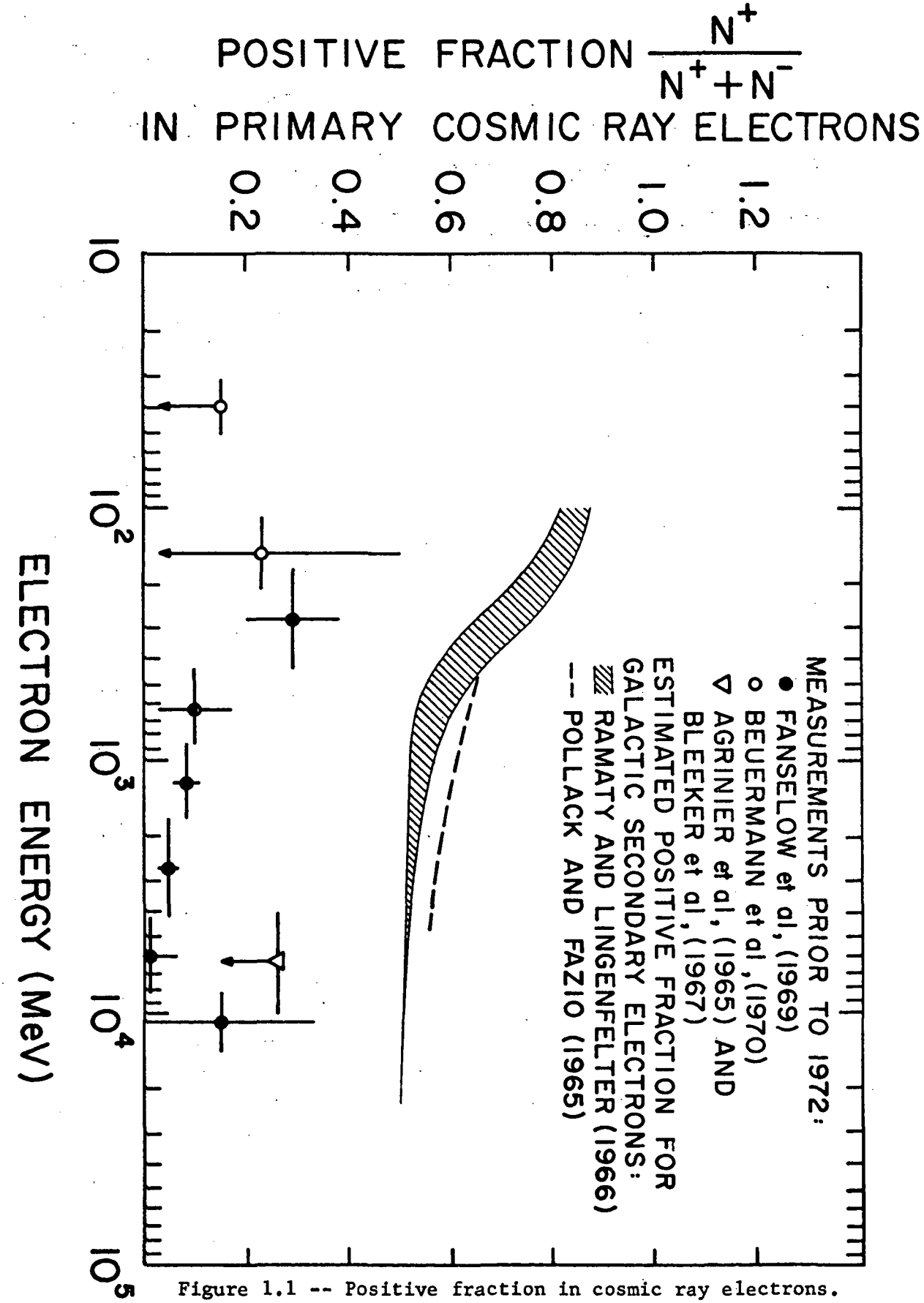

Figure 1.1 -- Positive fraction in cosmic ray electrons.

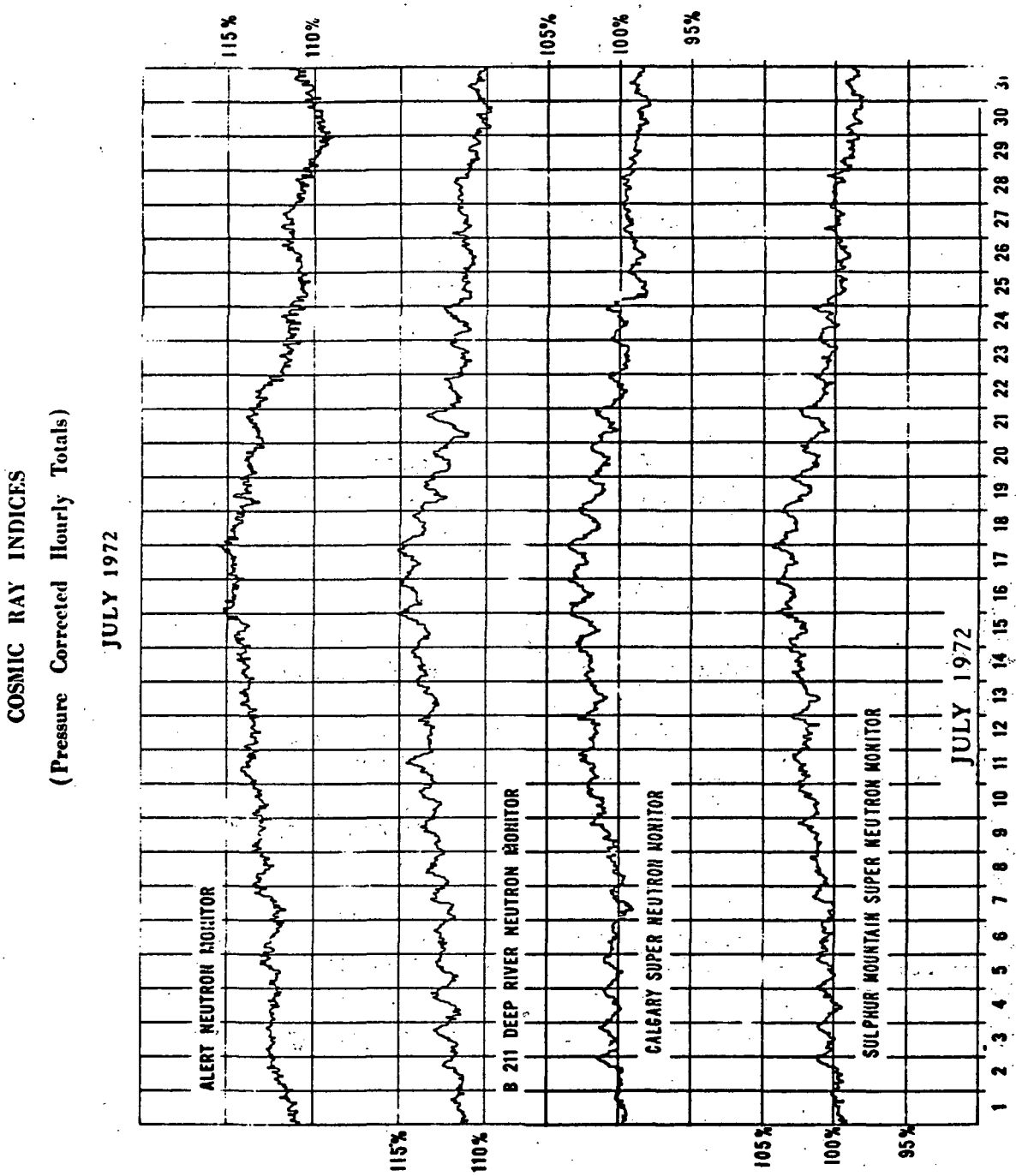

Figure 1.2 -- Neutron monitor counting rates, July 1972.

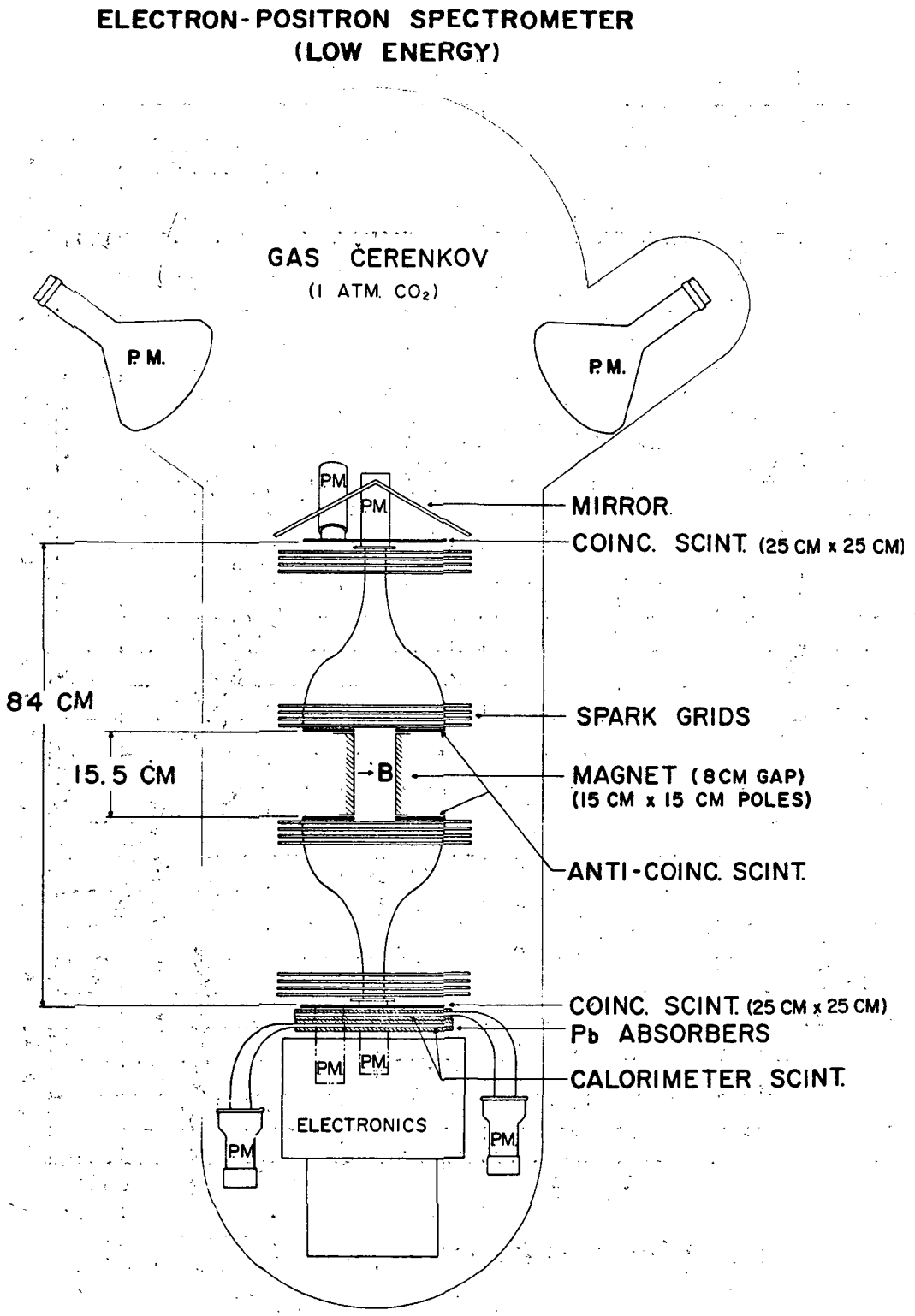

Figure 1.3 -- Schematic diagram of the detector.

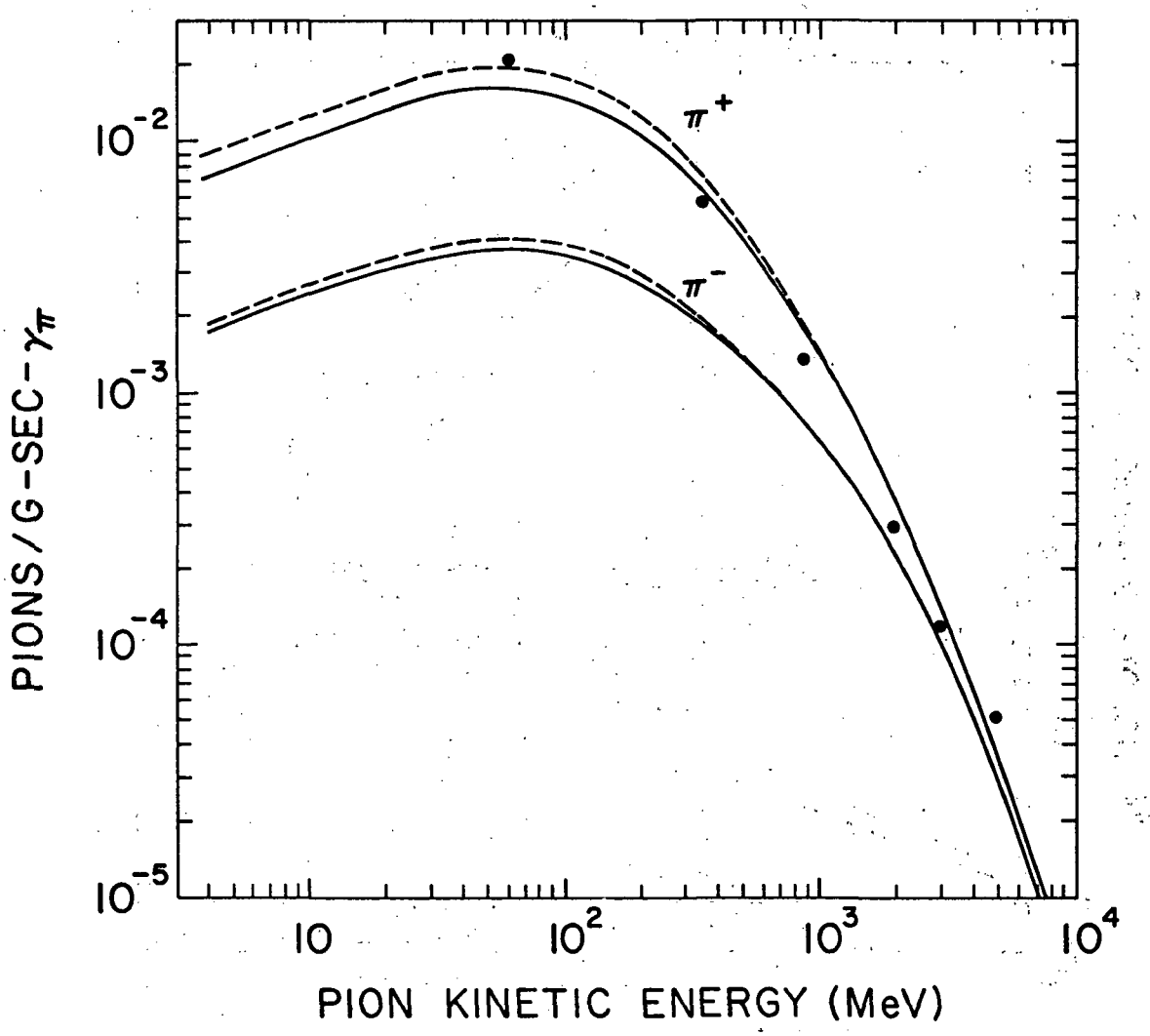

Figure 2.1 -- Charged pion source spectra in the interstellar medium (Ramaty, 1973). Solid lines are source spectra calculated from assumed interstellar proton spectrum identical to that observed near earth at solar minimum. Dashed lines are obtained by correcting proton spectrum for residual modulation at solar minimum. Also shown are points calculated by Perola et al. (1967).

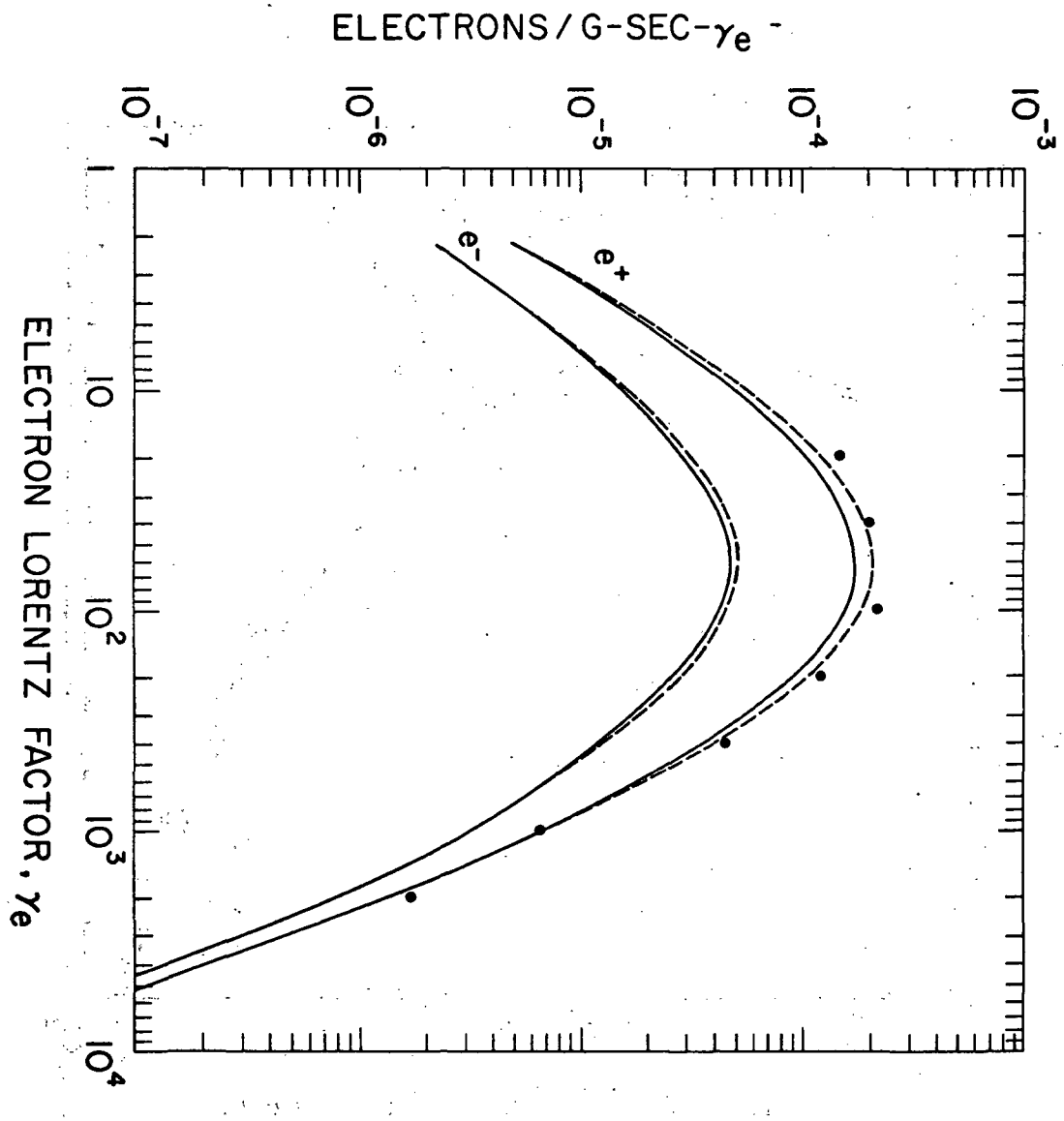

Figure 2.2 -- Positron and negatron source spectra in the interstellar medium (Ramaty, 1973). All symbols correspond to those in Figure 2.1.

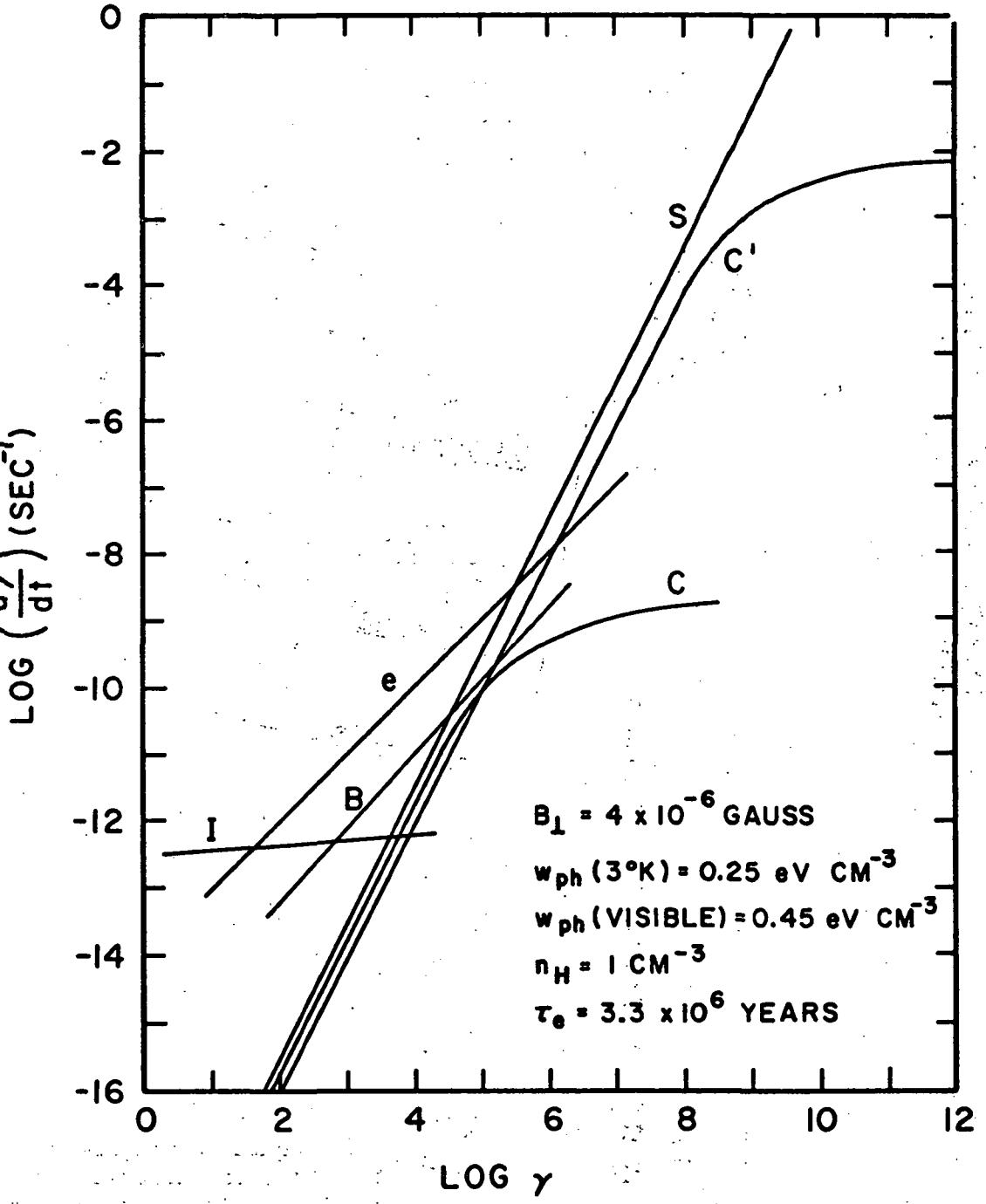

Figure 3.1 -- Energy loss rates for ionization (I), bremsstrahlung (B), Compton scattering from starlight (C) and blackbody (C') photons, and synchrotron radiation (S). Also shown is equivalent loss rate for energy-independent leakage lifetime (τ_e).

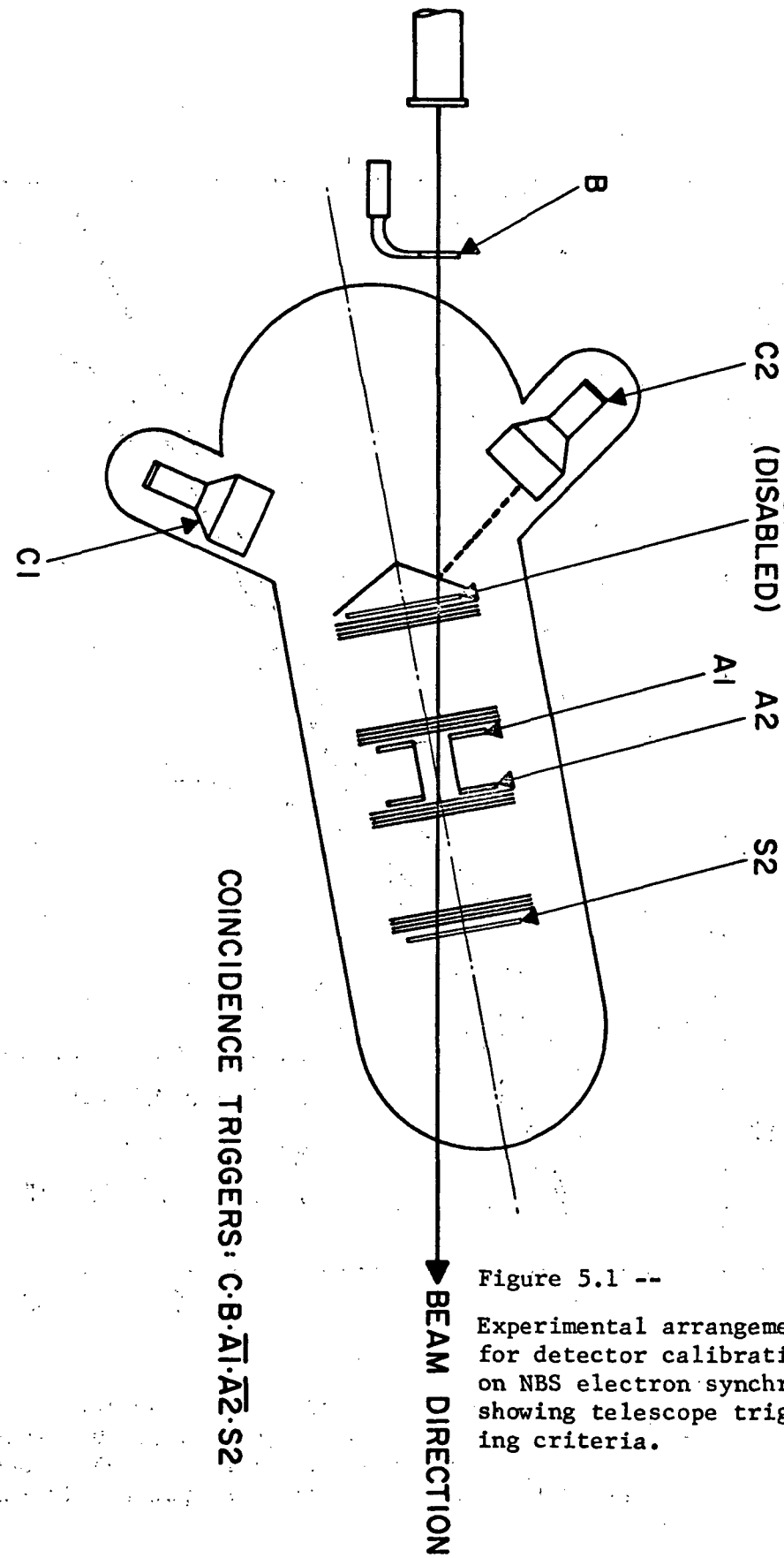

Figure 5.1 --

Experimental arrangement for detector calibration on NBS electron synchrotron, showing telescope triggering criteria.

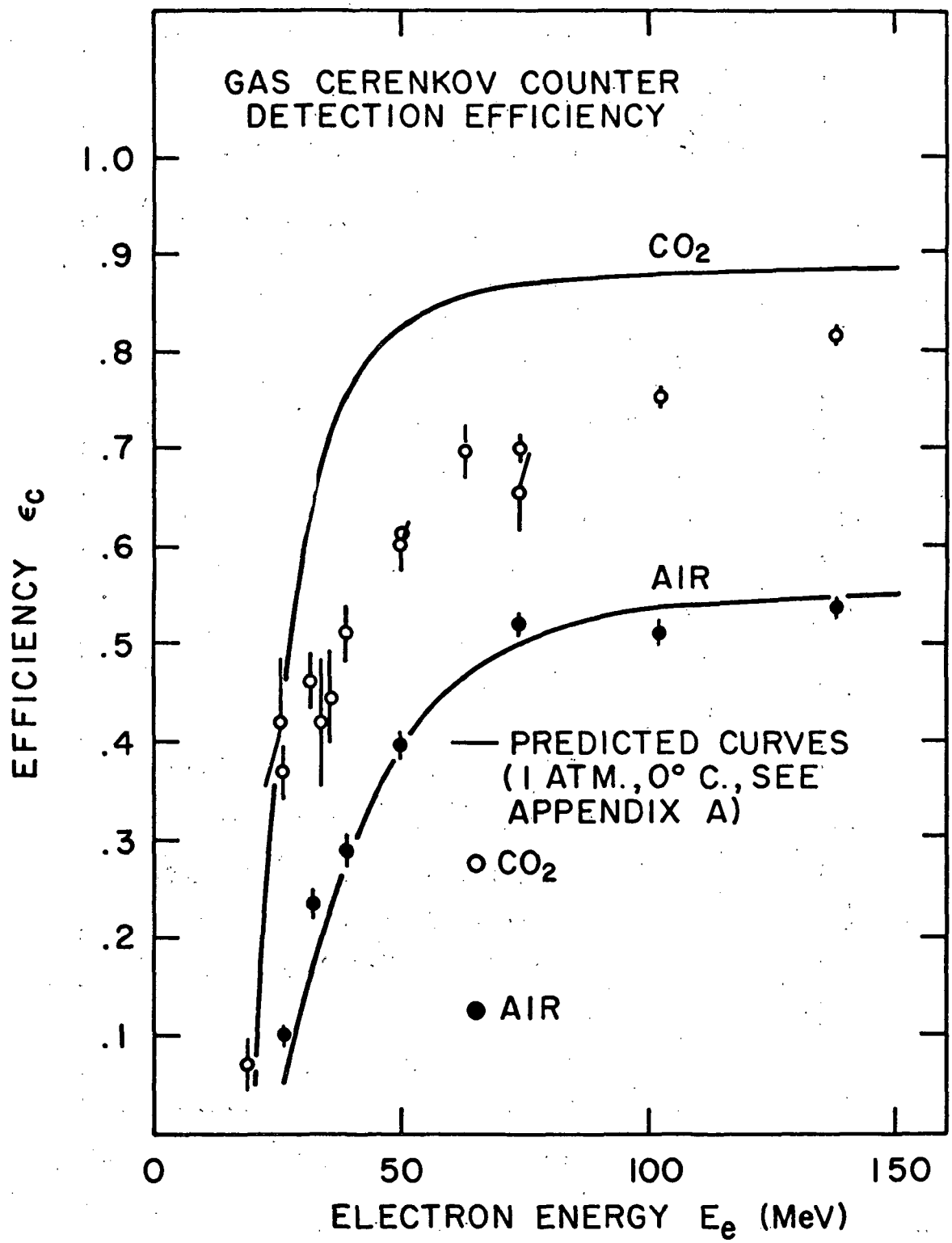

Figure 5.2 -- Cerenkov counter efficiencies for carbon dioxide (1 atm) and air (1 atm).

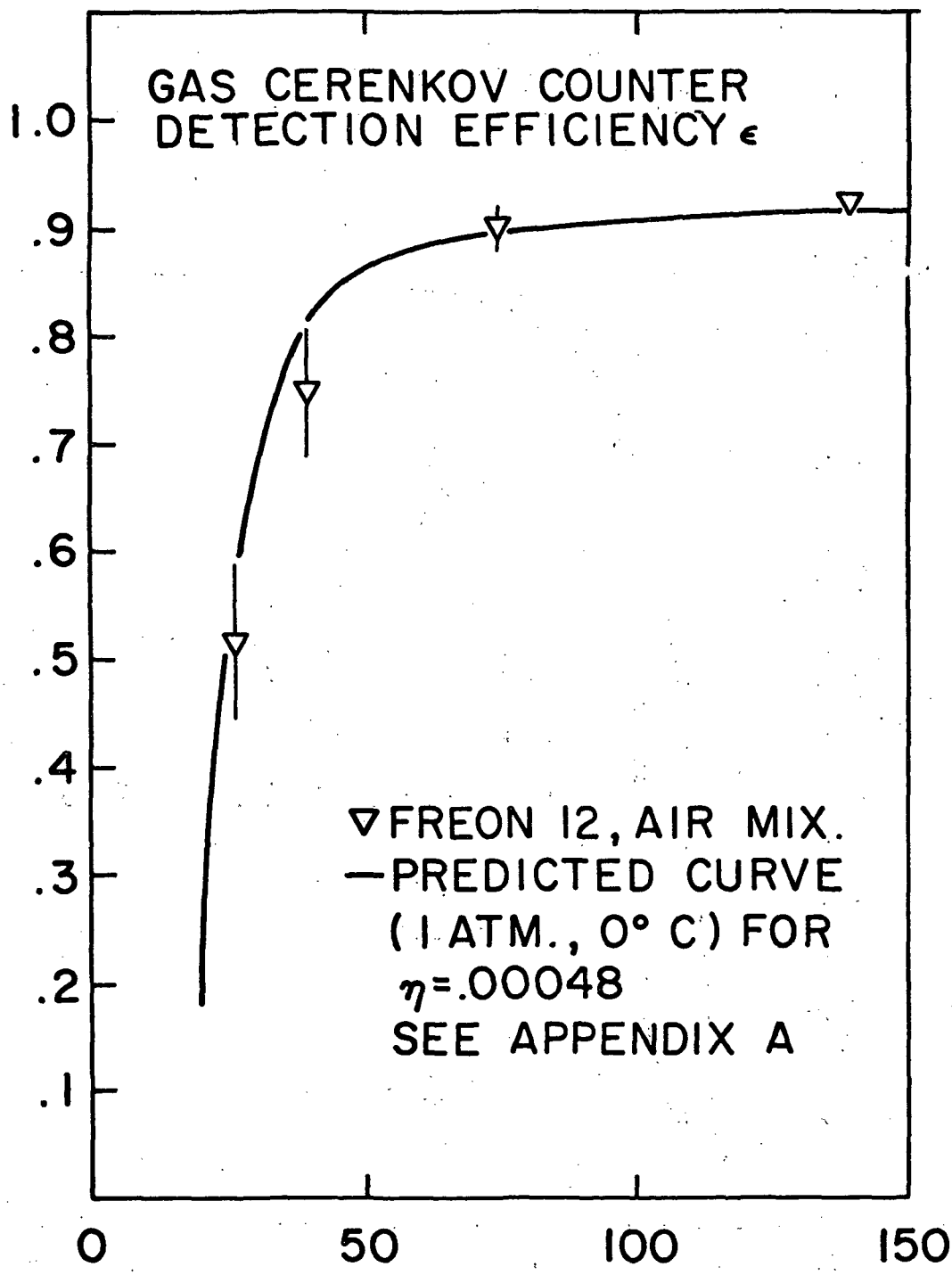

Figure 5.3 -- Cerenkov counter efficiency for 1-atm mixture of Freon-12 and air.

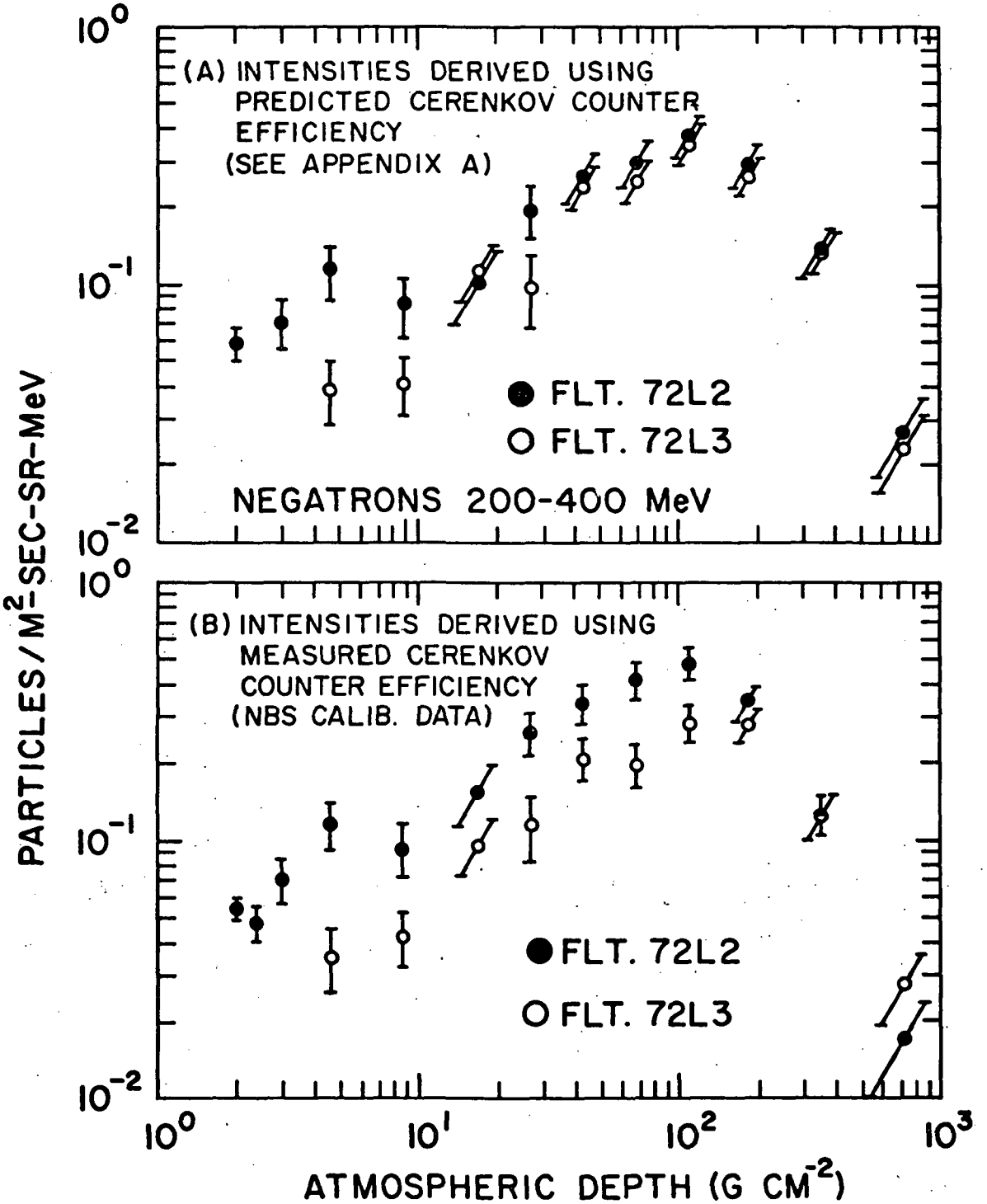

Figure 5.4 -- Atmospheric depth dependence measurements of 200-400 MeV negatron intensities for flights 72L2 and 72L3(see Chapter VI). Comparison of intensities estimated for measured and predicted values of Cerenkov counter detection efficiency.

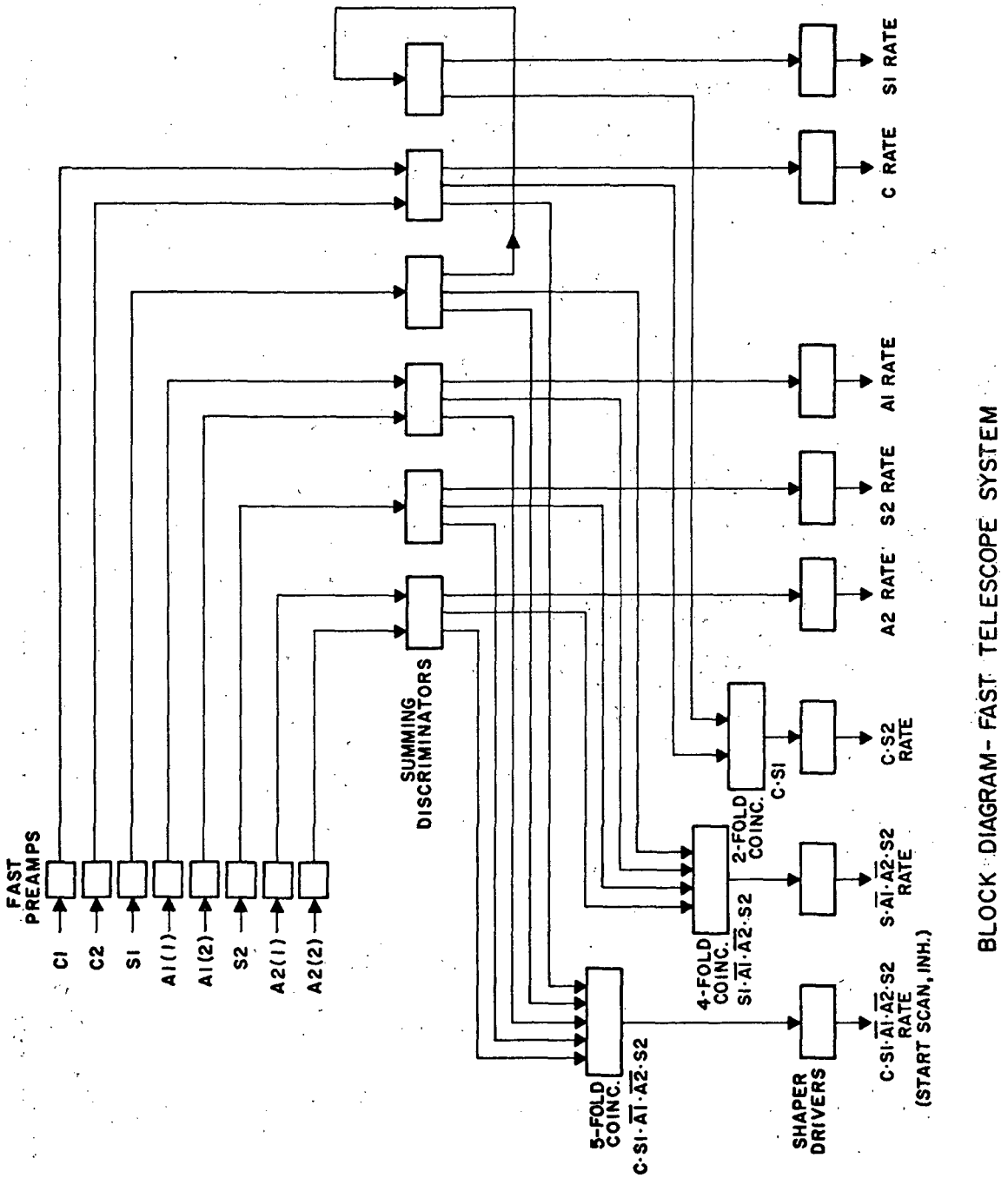

Figure 5.5 -- Block diagram of detector telescope system.

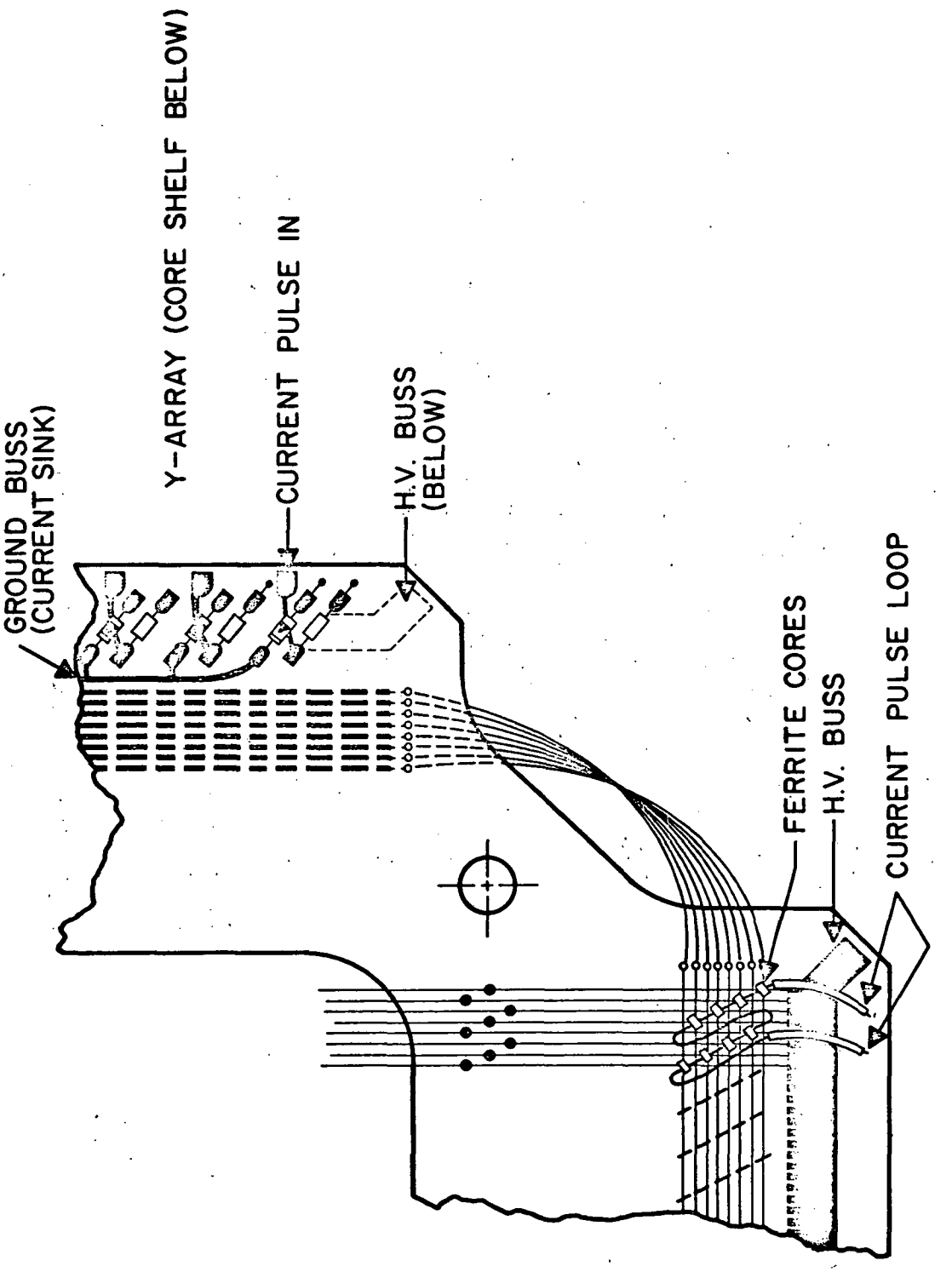

Figure 5.6 -- Grid module, core shelf layout.

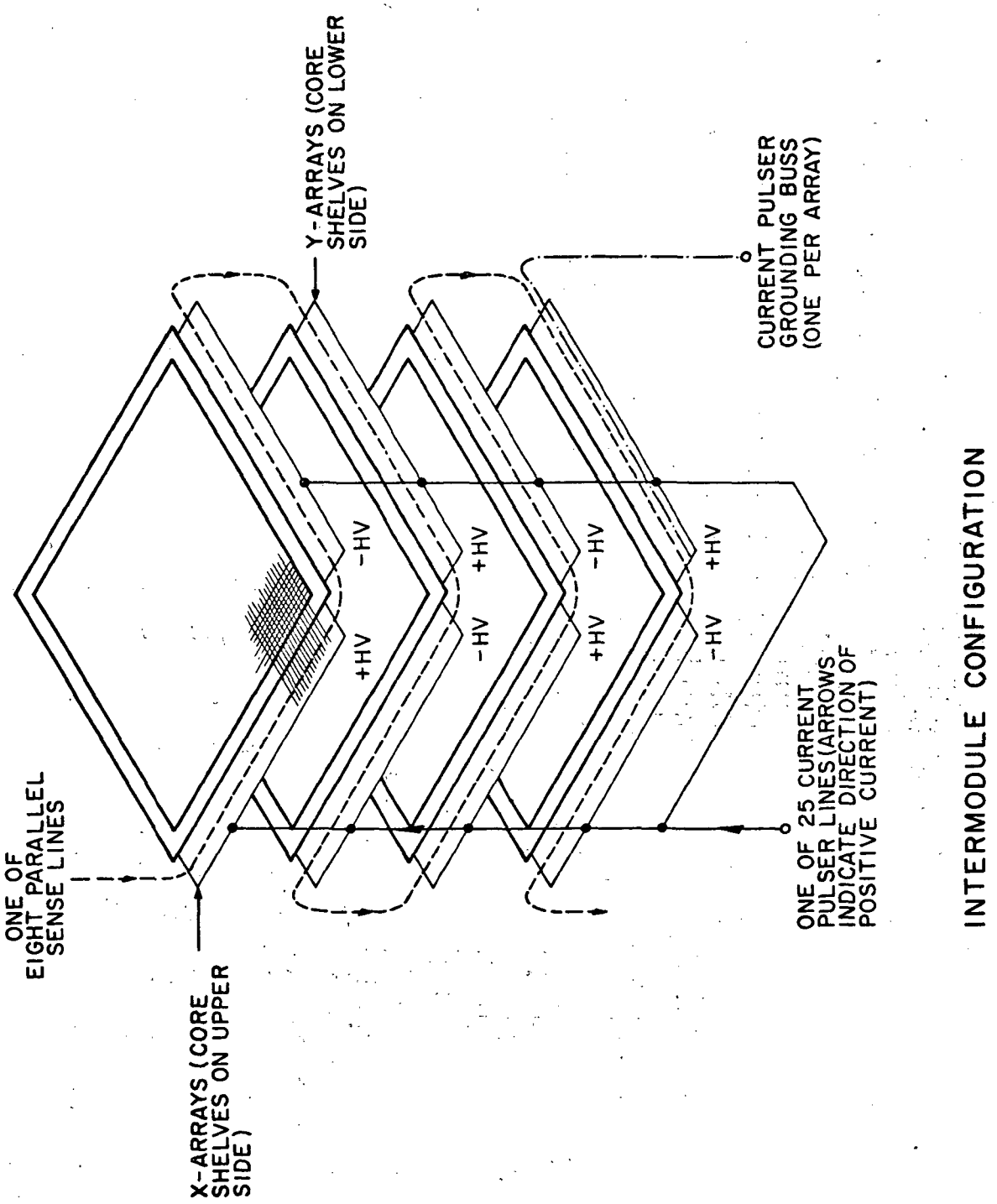

Figure 5.7 -- Grid module interconnections (one tier).

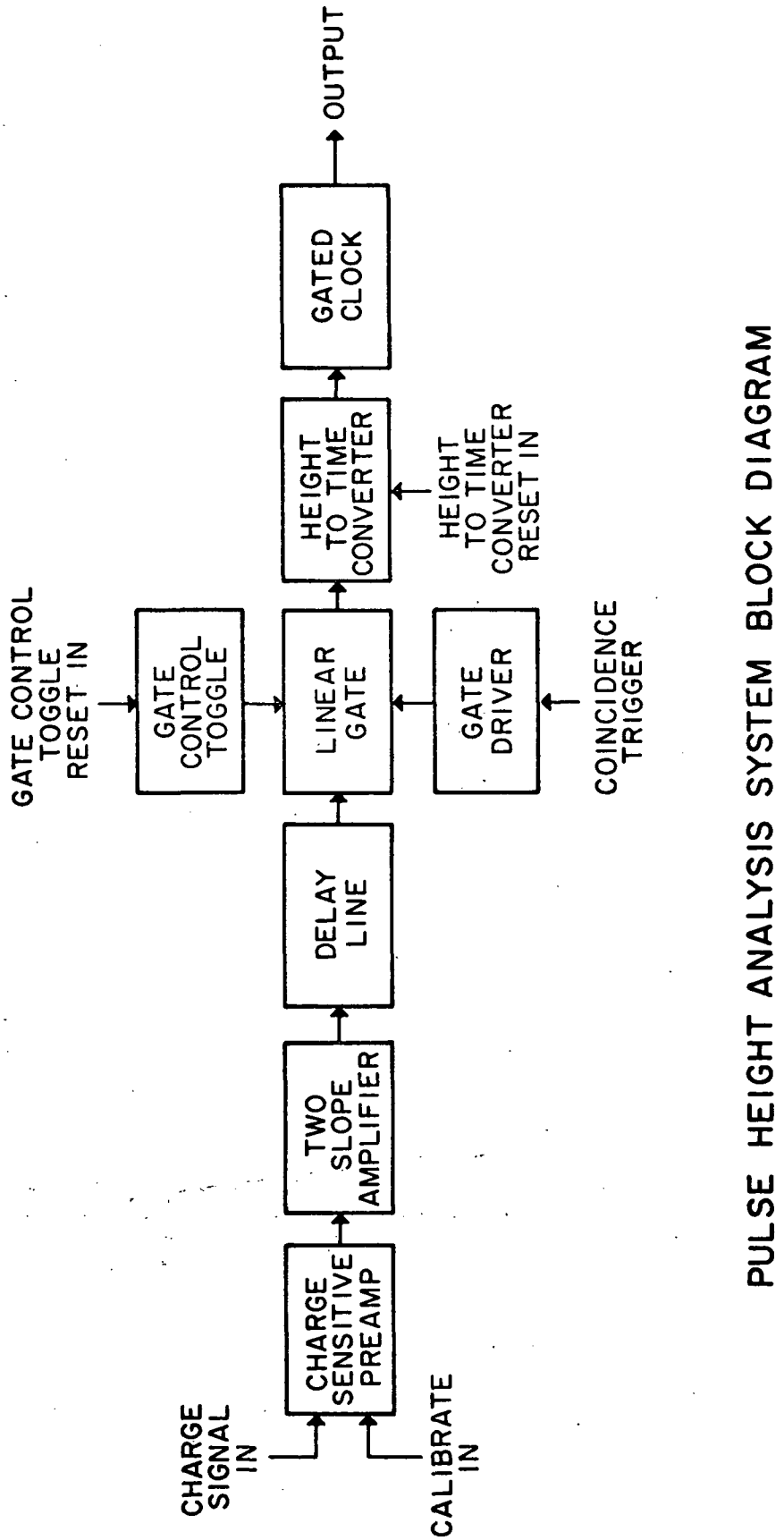

Figure 5.8 -- Block diagram of shower counter pulse height analyzer system.

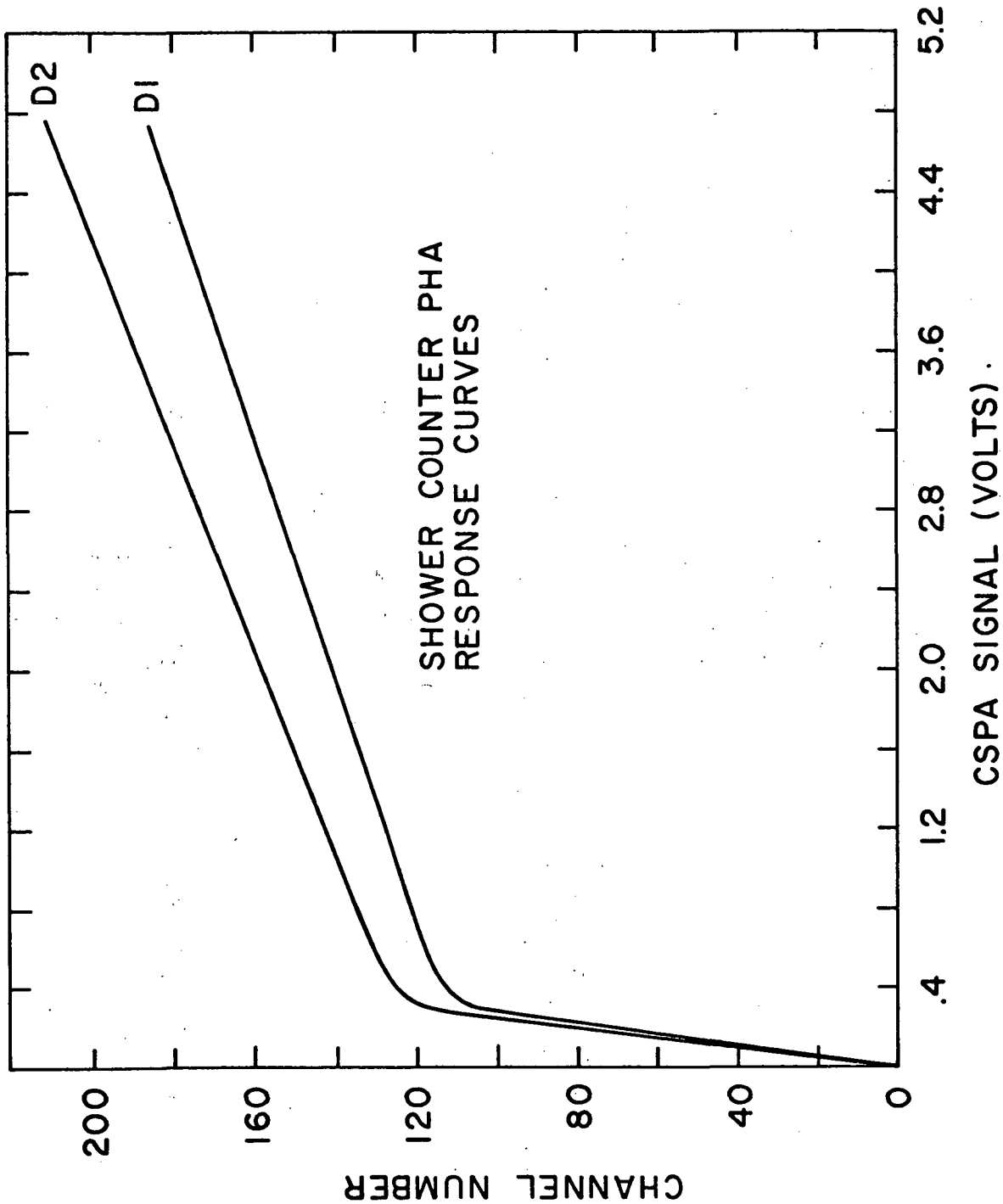

Figure 5.9 -- Response curves of shower counter pulse height analyzers D1 (upper scintillator) and D2 (lower scintillator).

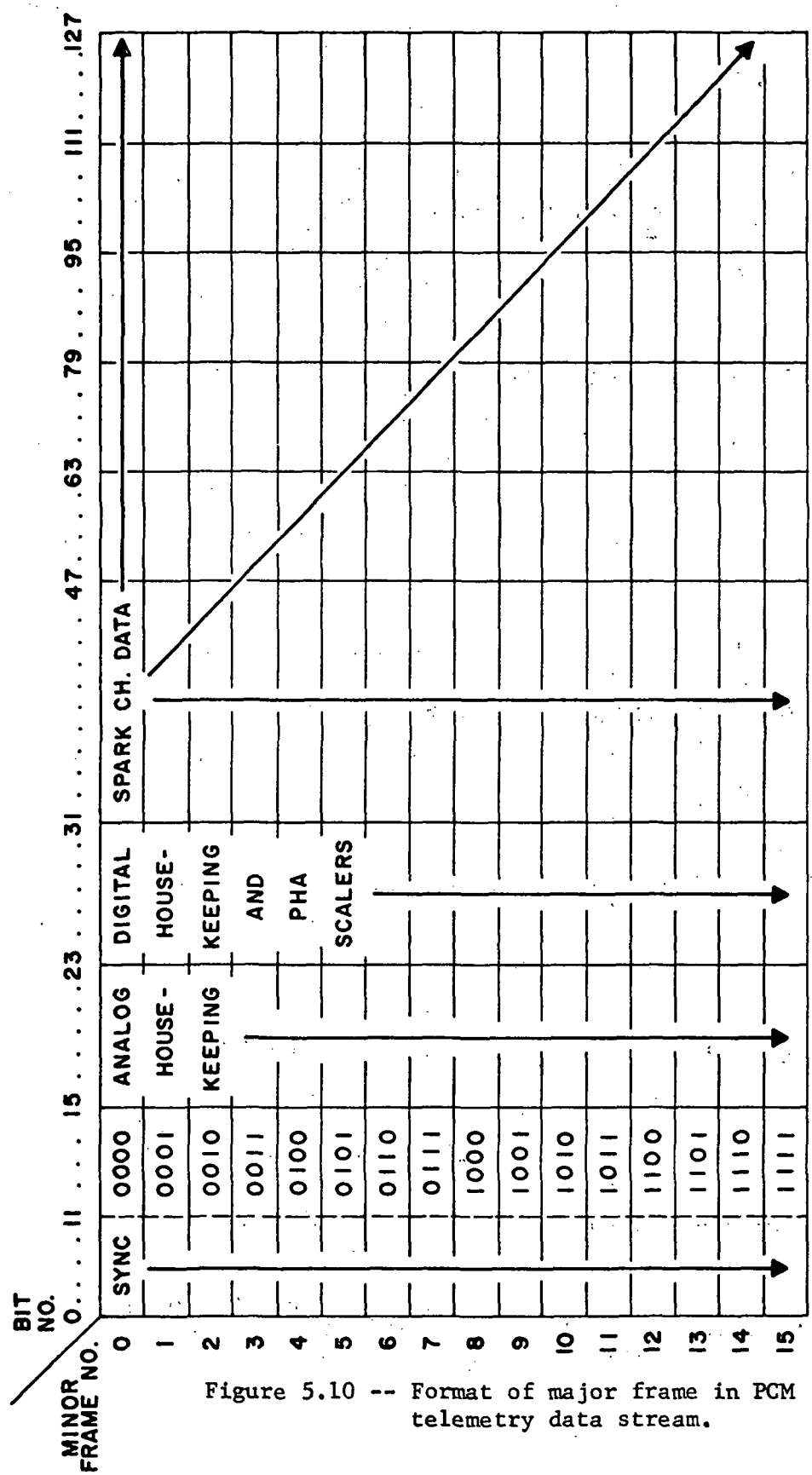

Figure 5.10 -- Format of major frame in PCM telemetry data stream.

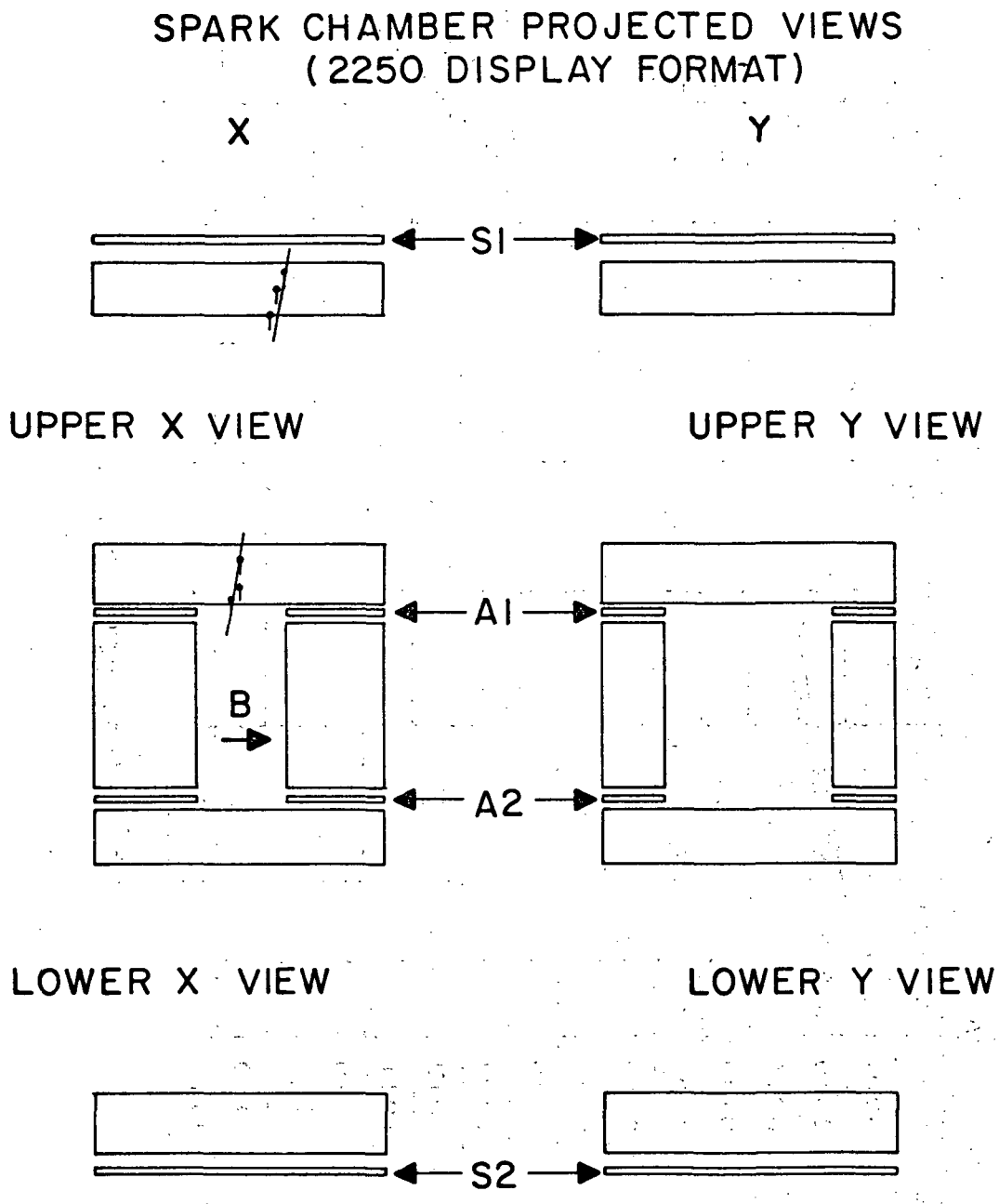

Figure 6.1 -- Format of IBM 1130/2250 Computer Graphics Display, showing x-z and y-z projections of upper and lower spark chambers and set core locations.

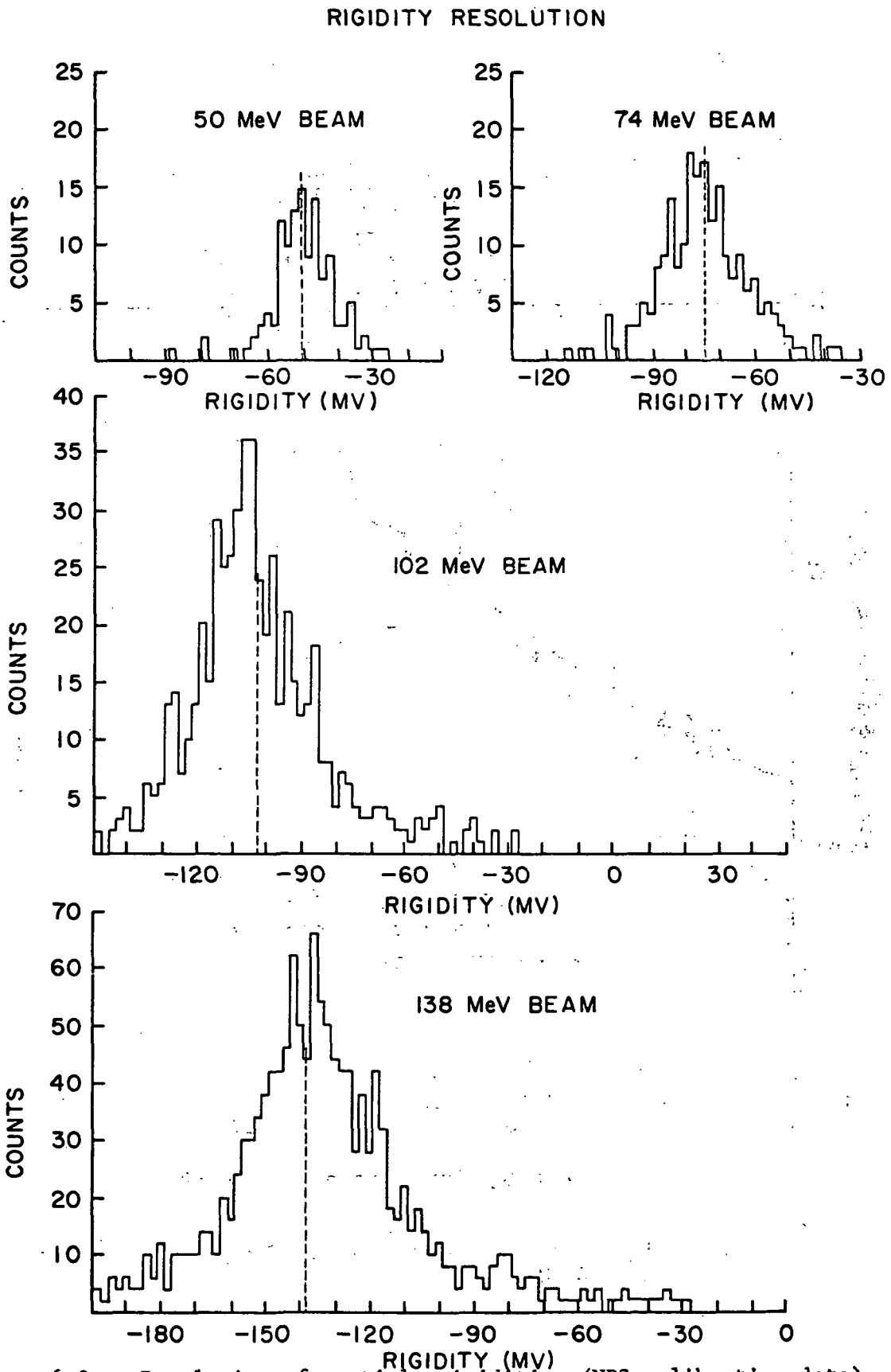

Figure 6.2 -- Resolution of particle rigidities (NBS calibration data).

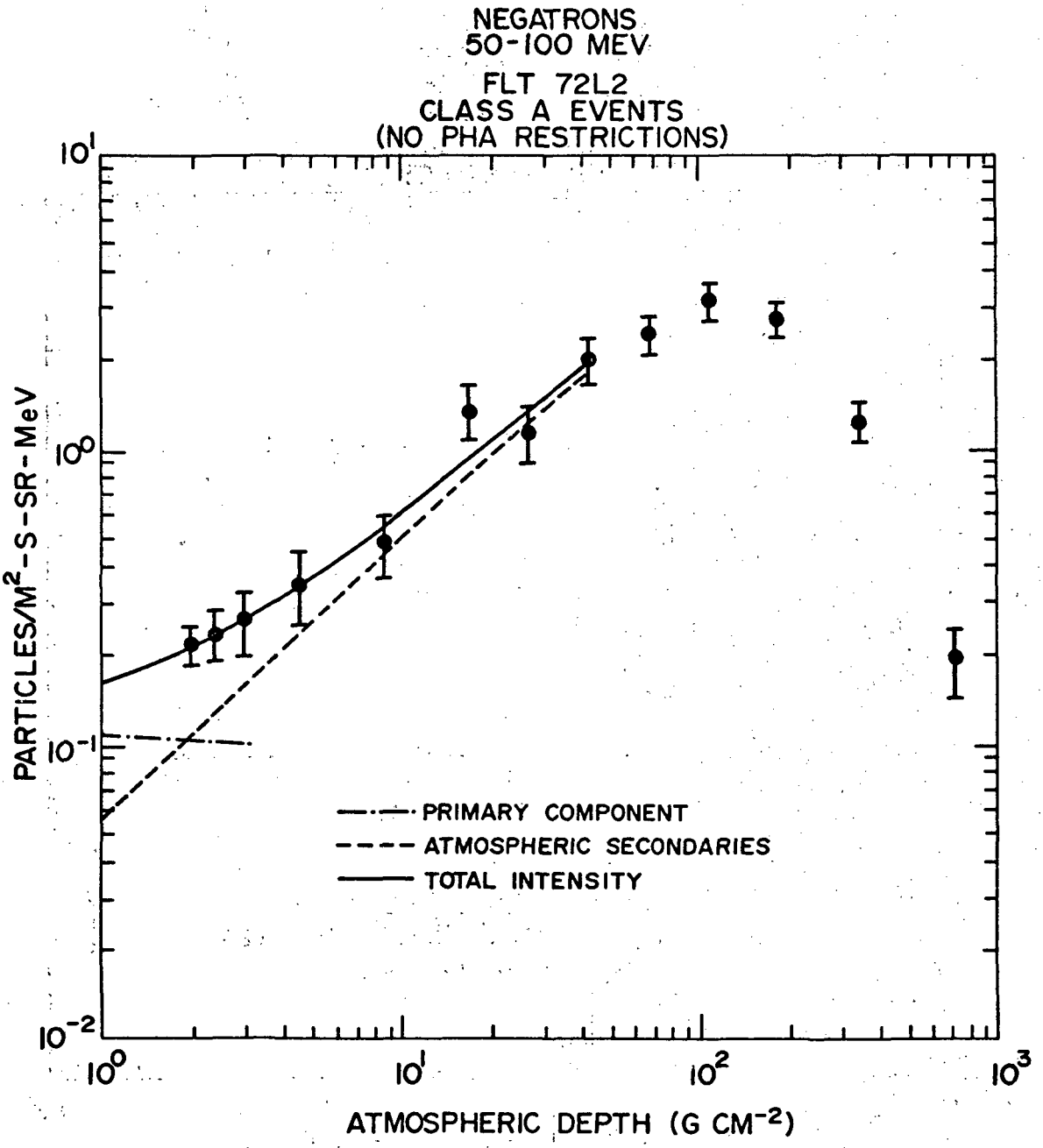

Figure 6.3 -- Atmospheric depth dependence of negatron intensity, 50 - 100 MeV.

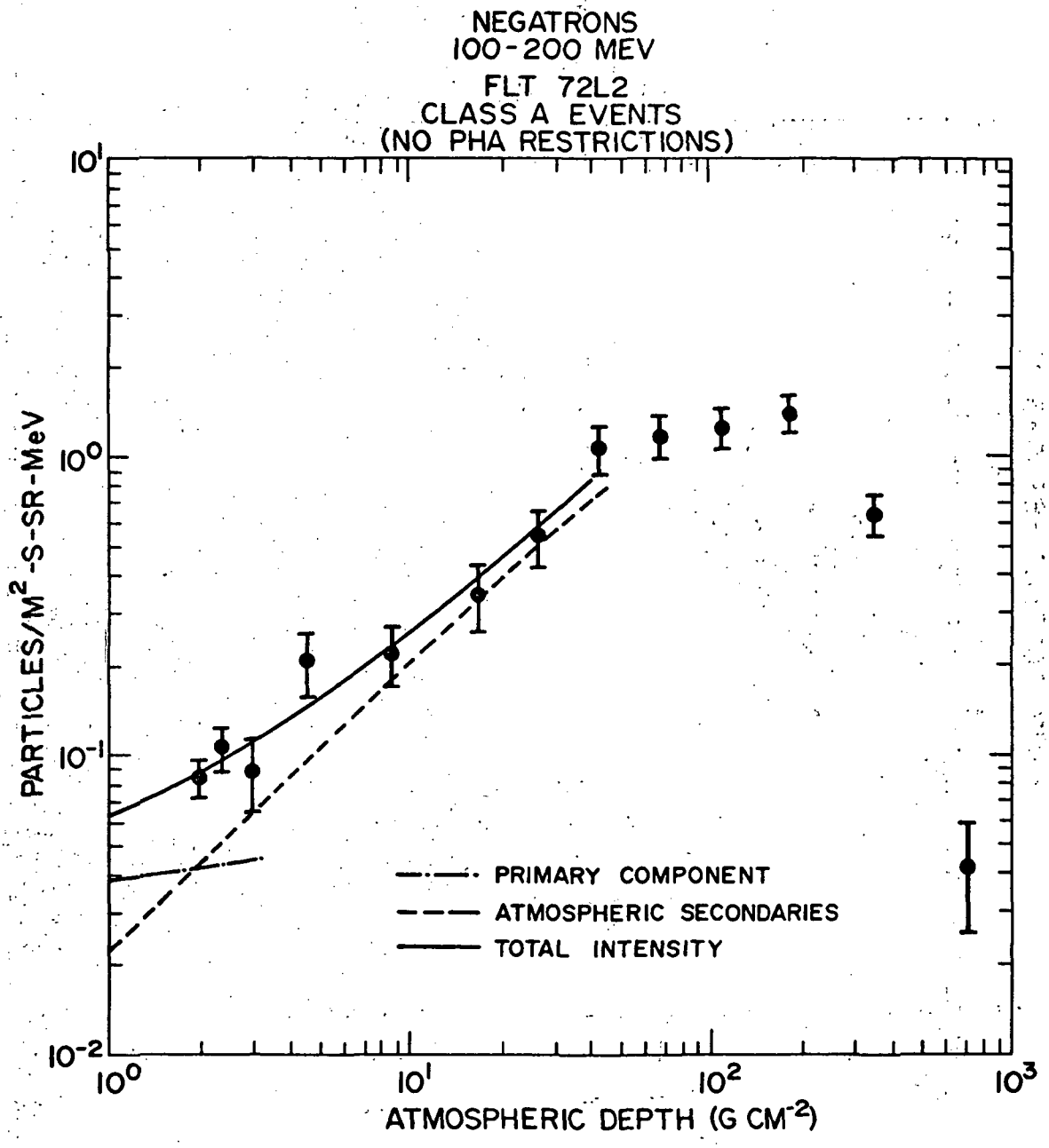

Figure 6.4 -- Atmospheric depth dependence of negatron intensity, 100 - 200 MeV.

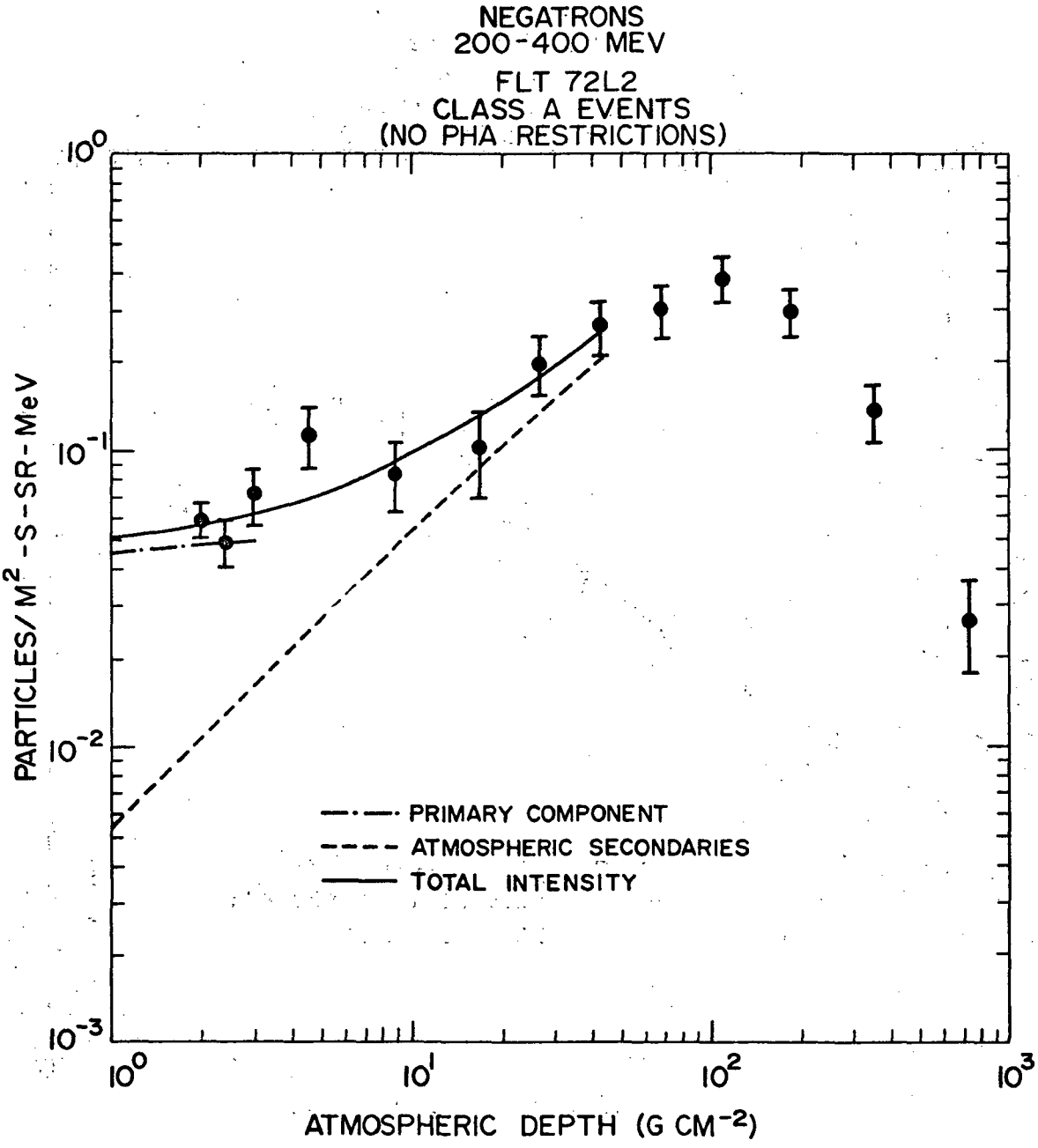

Figure 6.5 -- Atmospheric depth dependence of negatron intensity, 200 - 400 MeV.

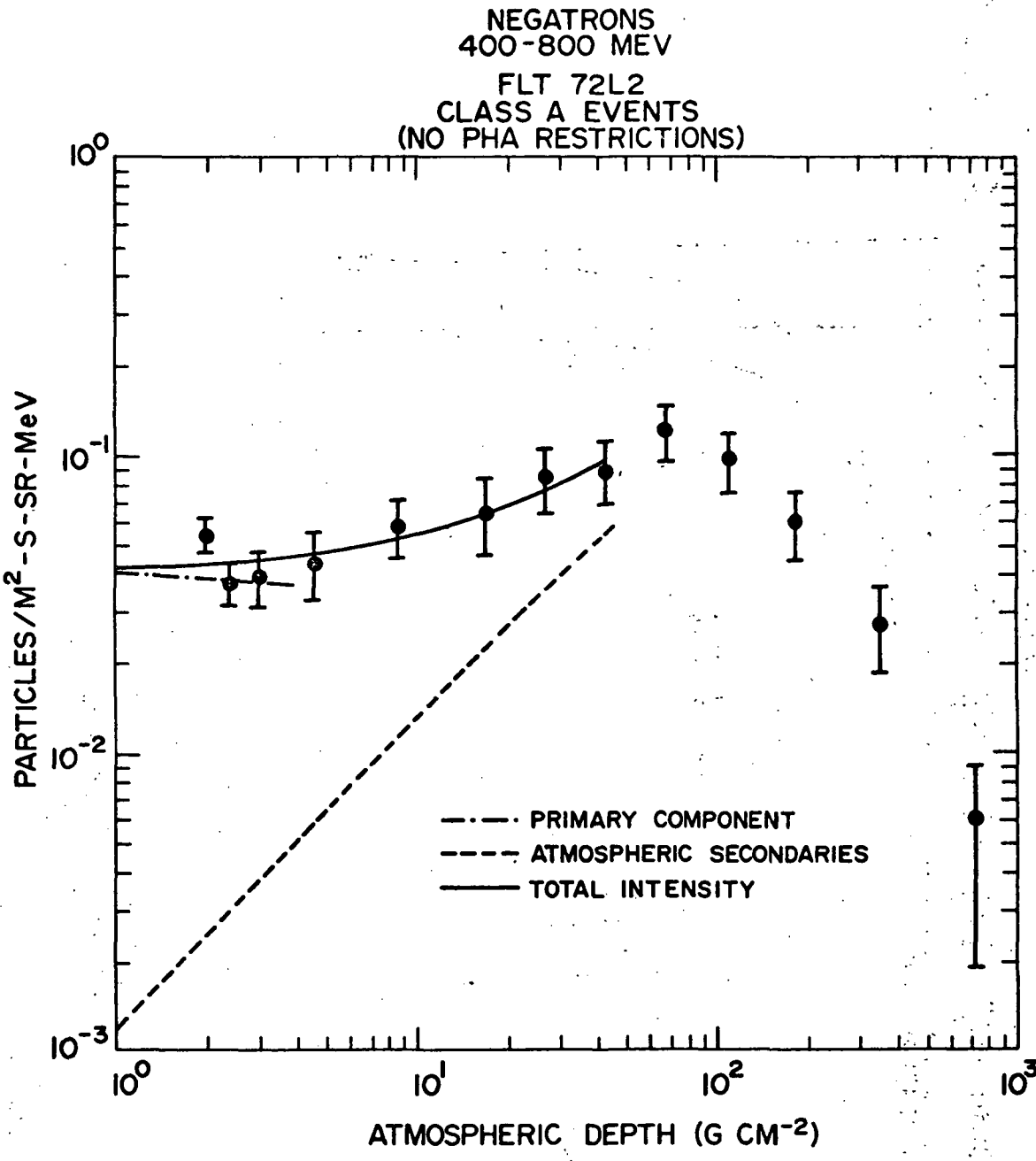

Figure 6.6 -- Atmospheric depth dependence of negatron intensity, 400 - 800 MeV.

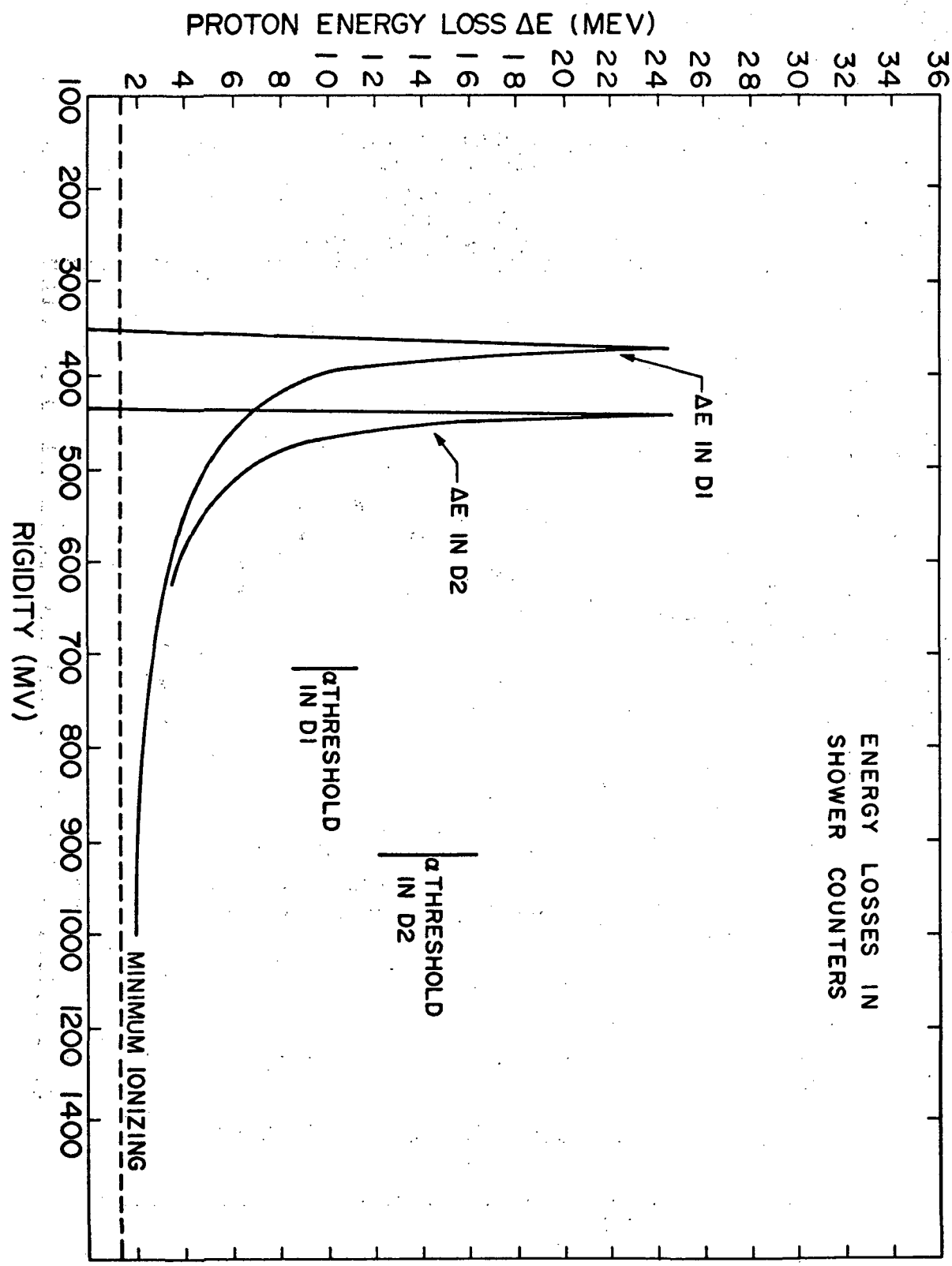

Figure 6.7 -- Calculated energy losses for protons in shower counters D1 and D2.

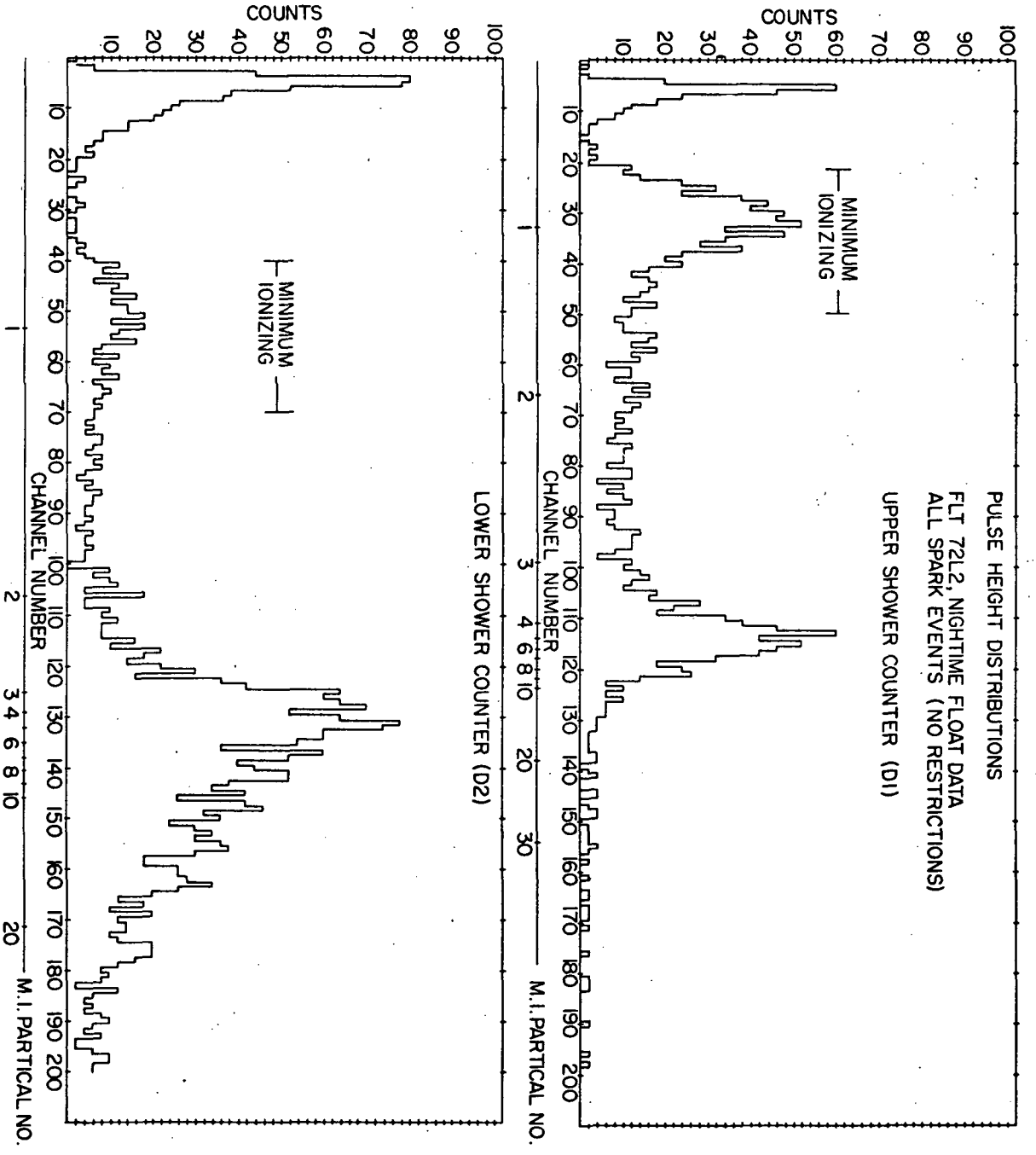

Figure 6.8 -- Pulse height distributions in shower counters D1 and D2 (float data, all spark events).

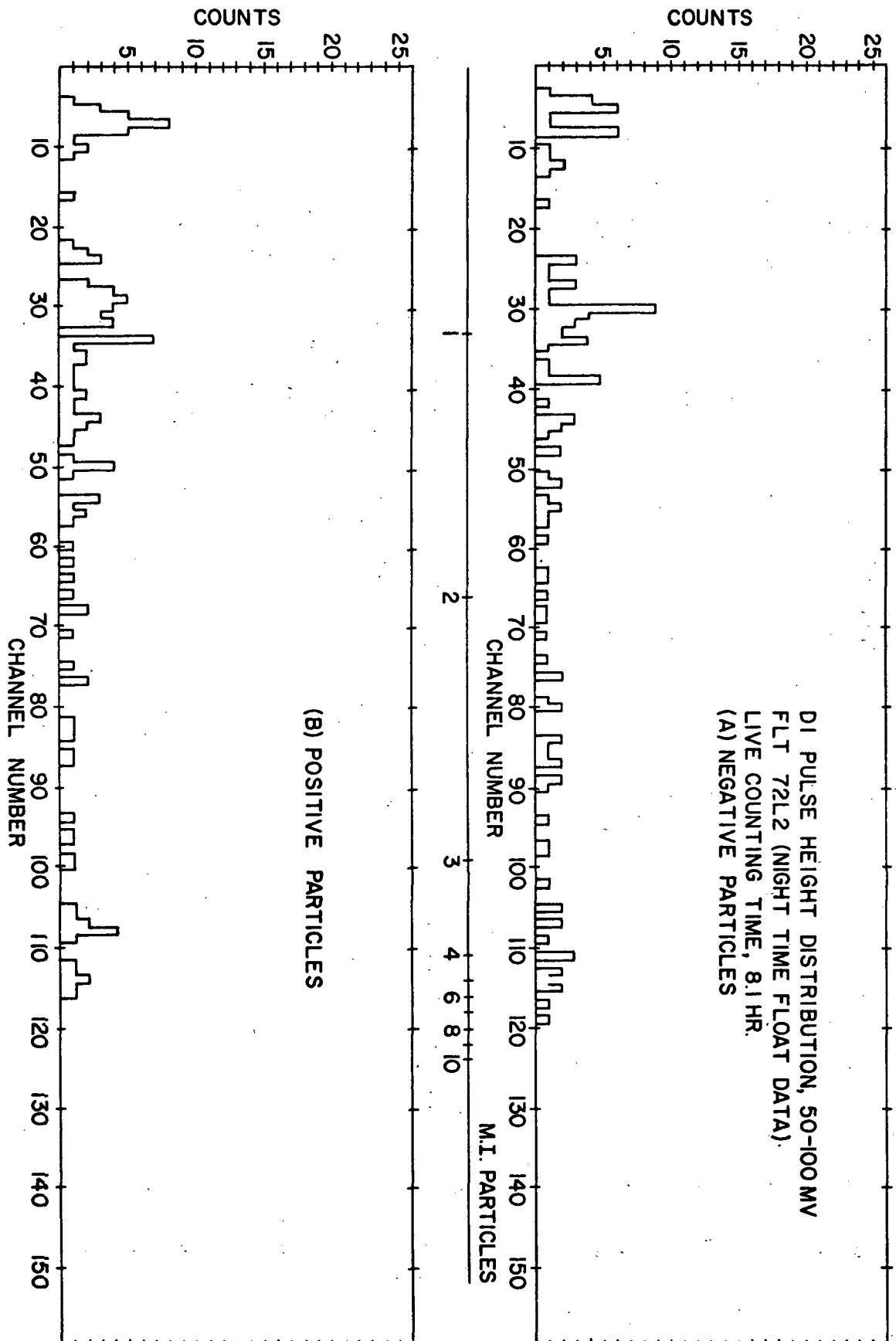

Figure 6.9 -- Pulse height distributions in D1 for 50-100 MV particles.

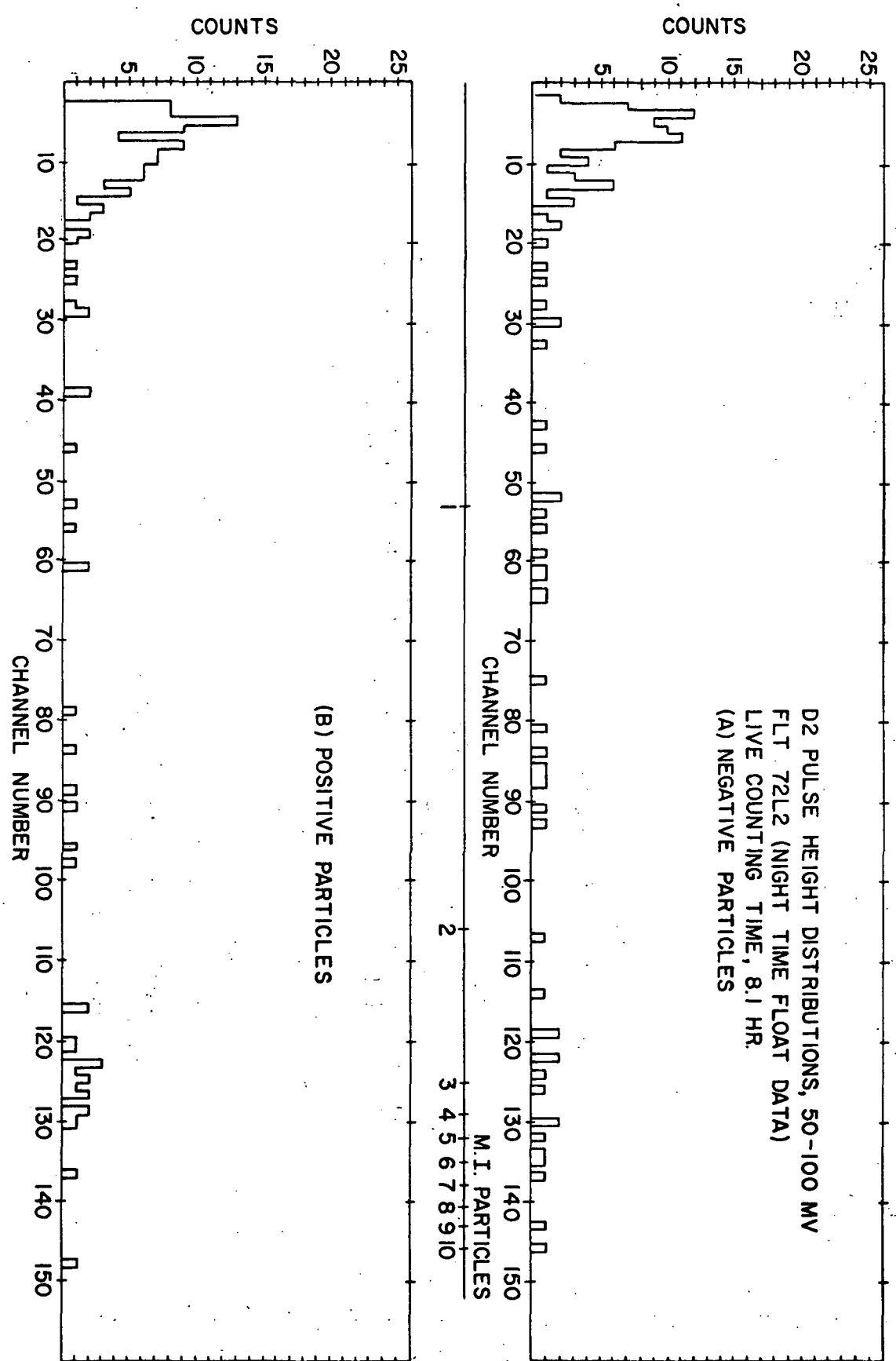

Figure 6.10 -- Pulse height distributions in D2 for 50-100 MV particles.

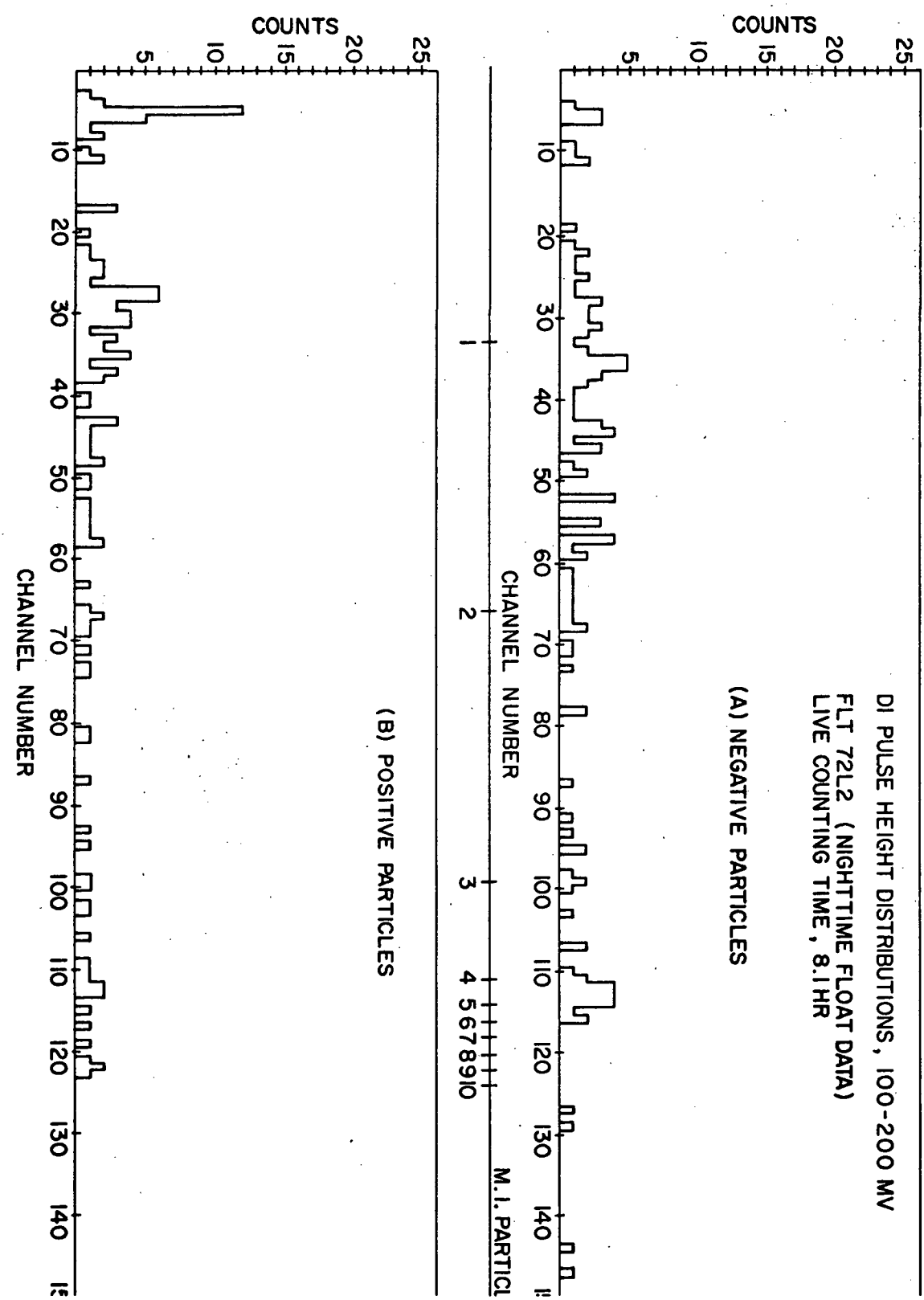

Figure 6.11 -- Pulse height distributions in D1 for 100-200 MV particles.

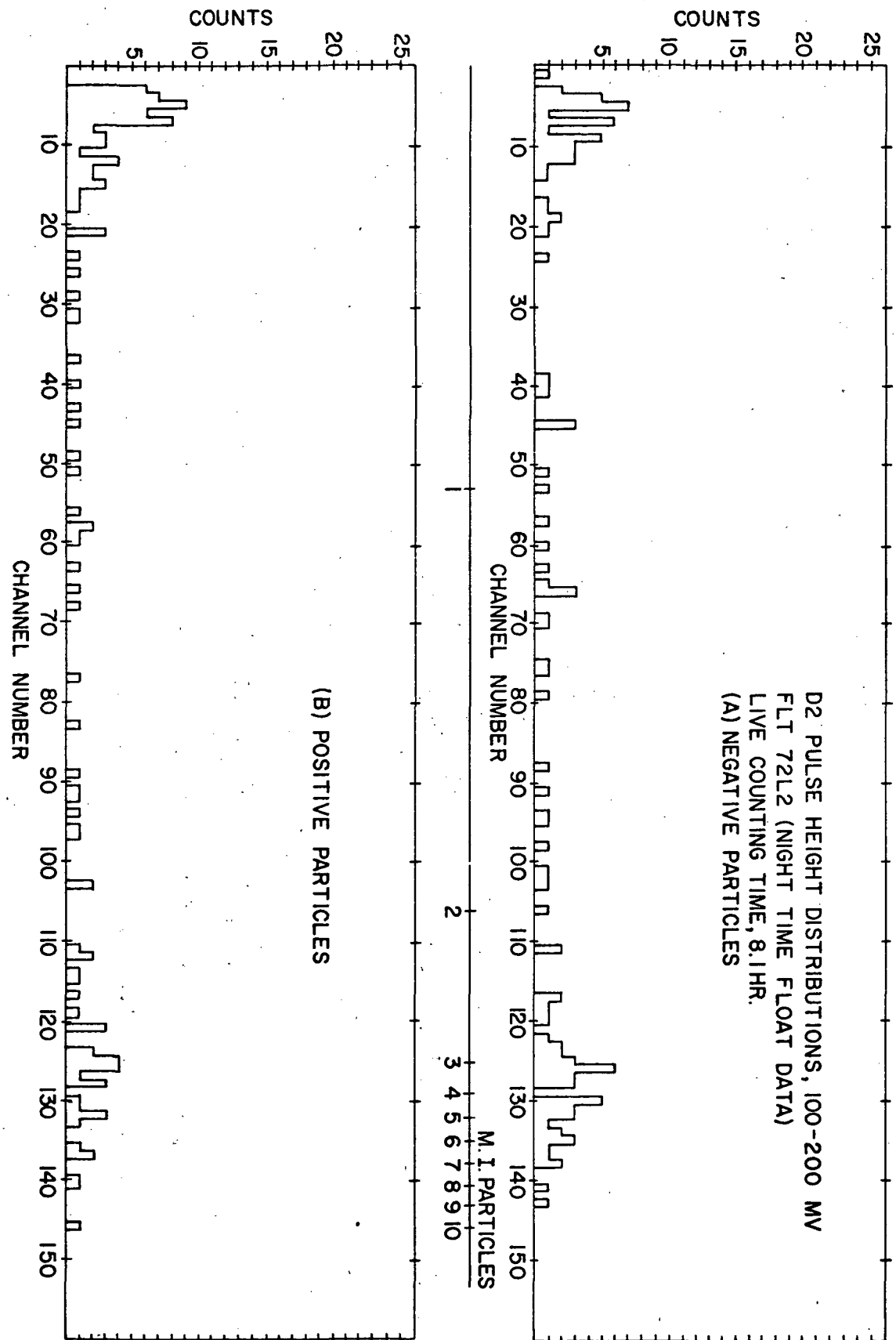

Figure 6.12 -- Pulse height distributions in D2 for 100-200 MV particles.

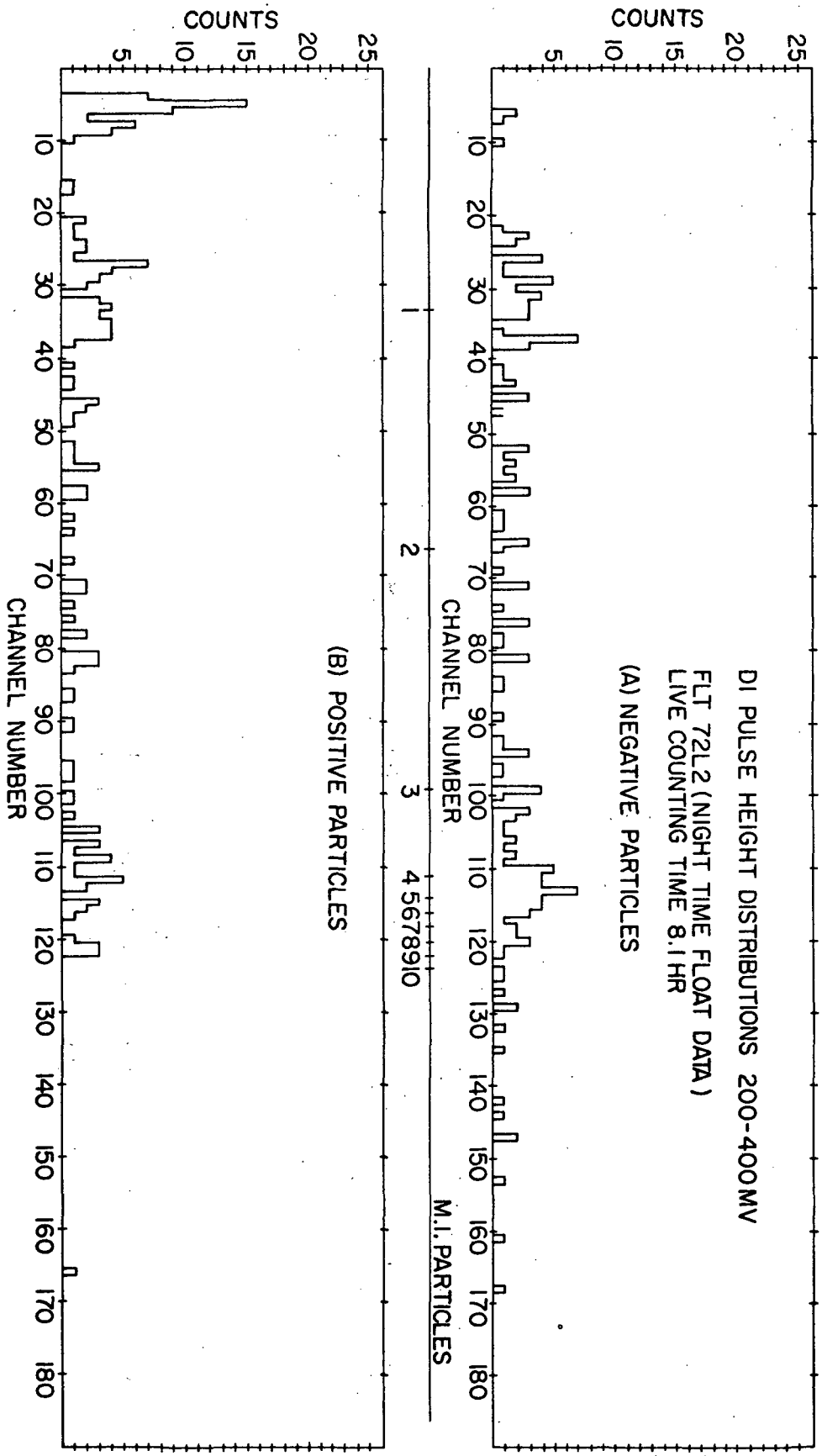

Figure 6.13 -- Pulse height distributions in D1 for 200-400 MV particles.

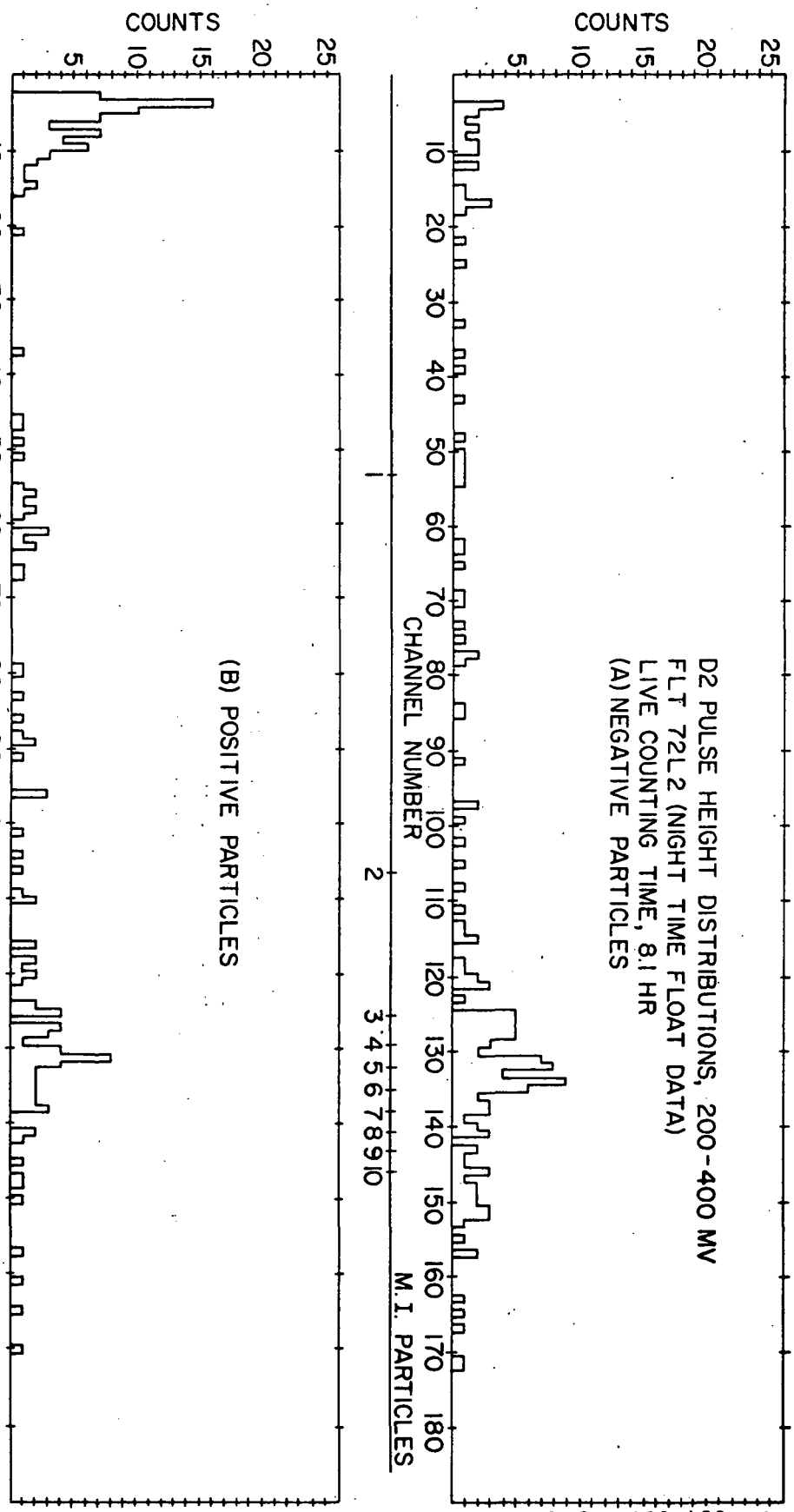

Figure 6.14 -- Pulse height distributions in D2 for 200-400 MV particles.

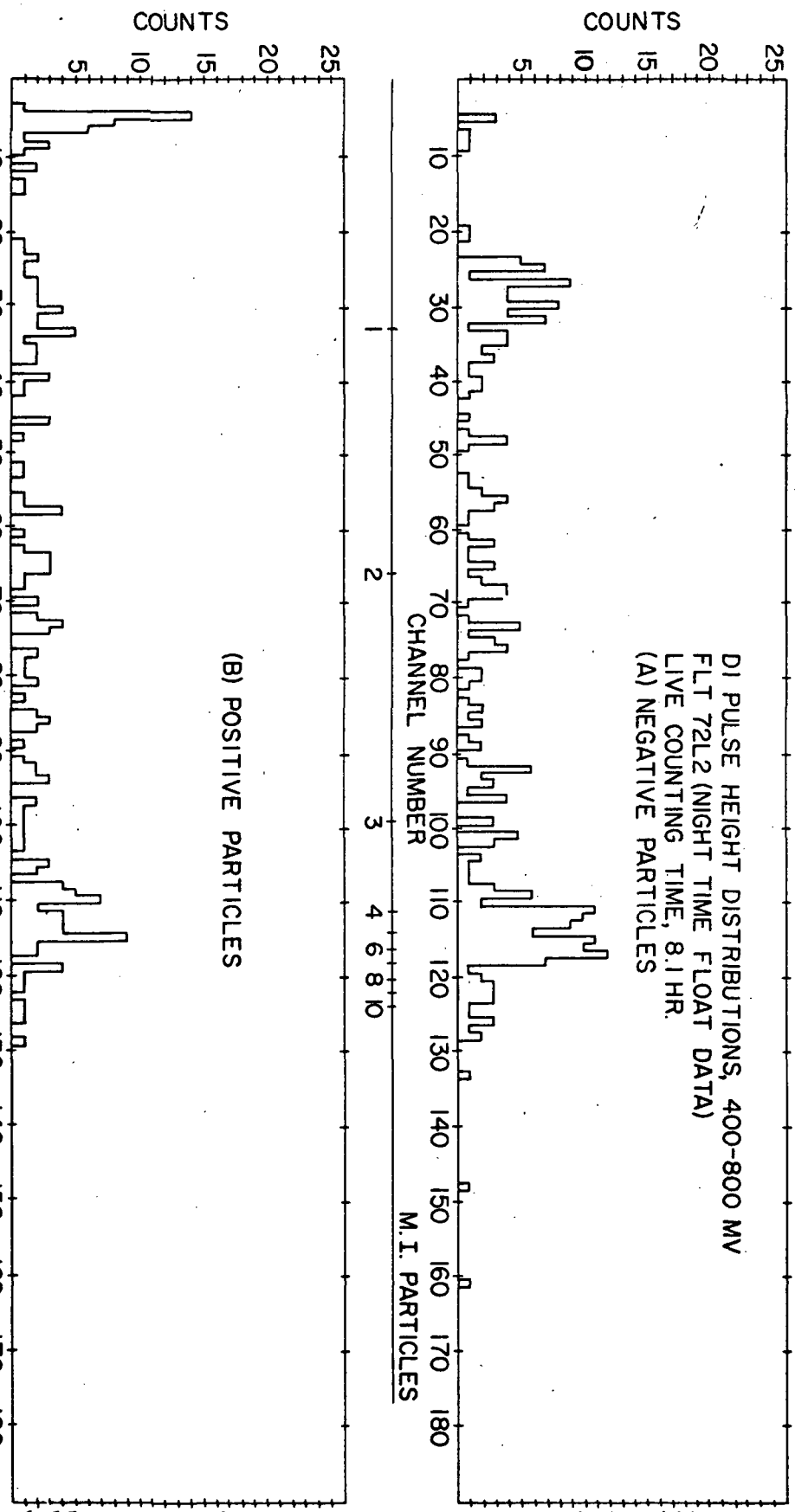

Figure 6.15 -- Pulse height distributions in D1 for 400-800 MV particles.

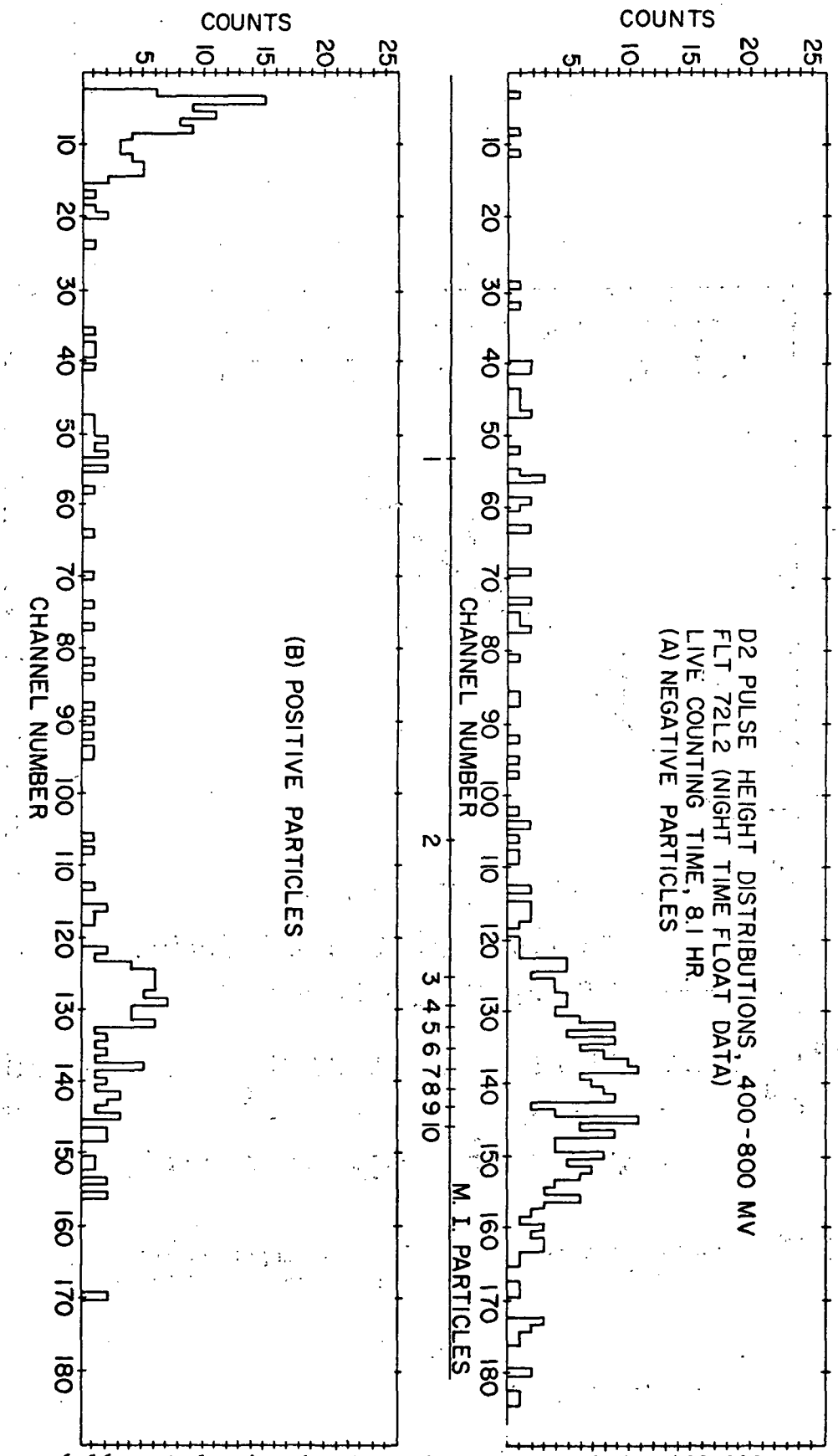

Figure 6.16 -- Pulse height distributions in D2 for 400-800 MV particles.

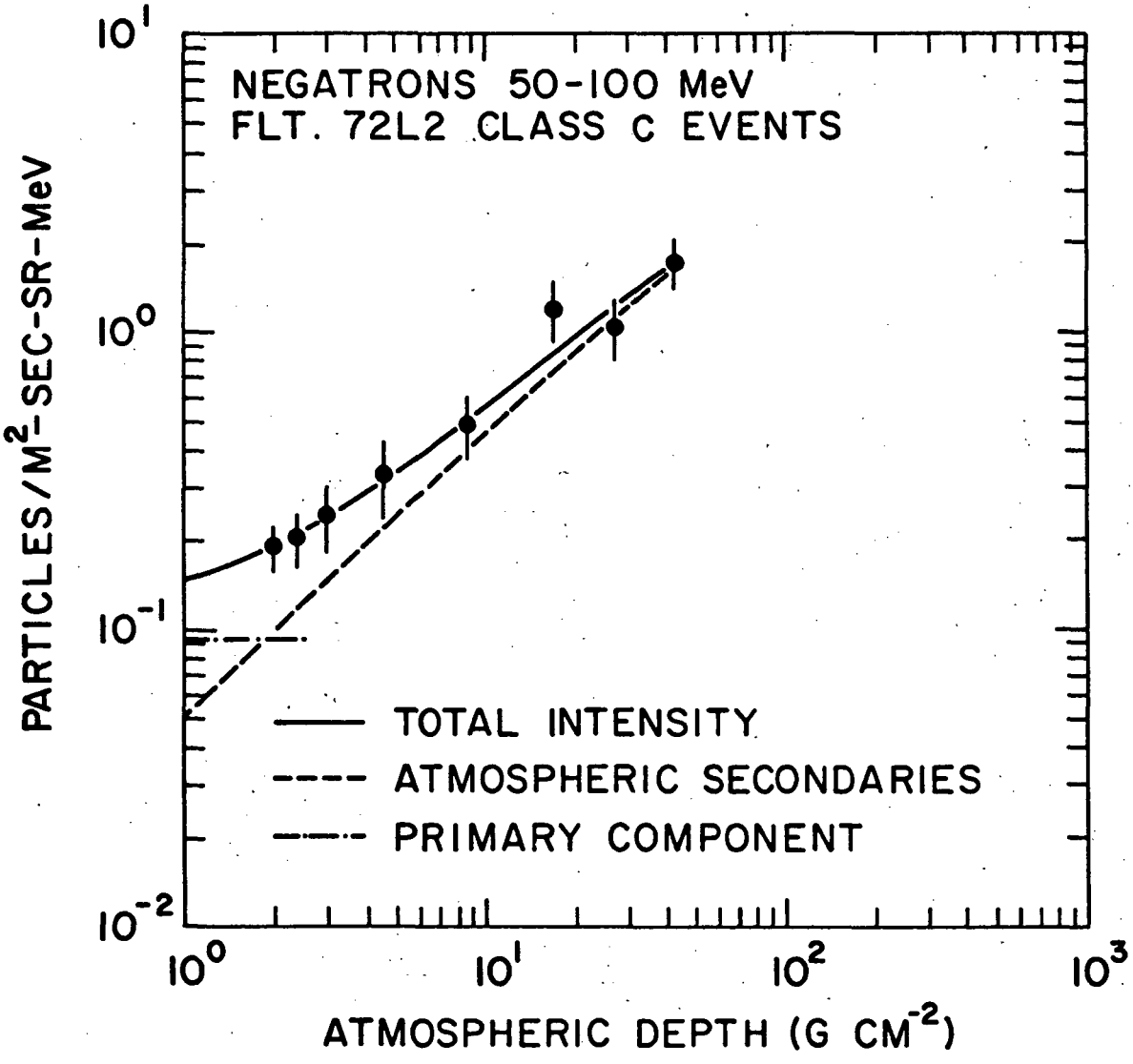

Figure 6.17 -- Atmospheric depth dependence of negatron intensity, 50-100 MeV (PHA-restricted events, see Table 6.4).

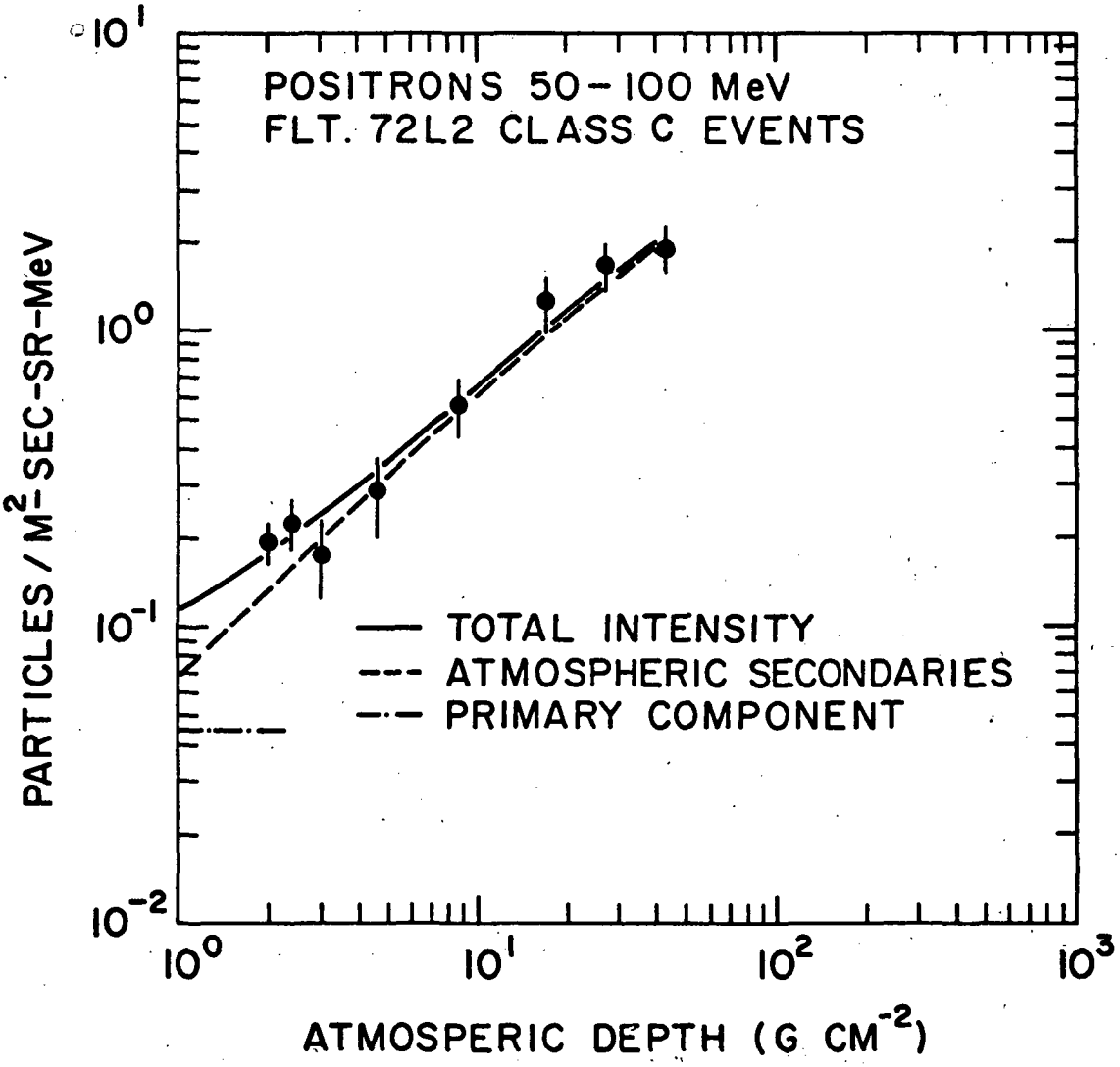

Figure 6.18 -- Atmospheric depth dependence of positron intensity, 50-100 MeV (PHA-restricted events, see Table 6.4).

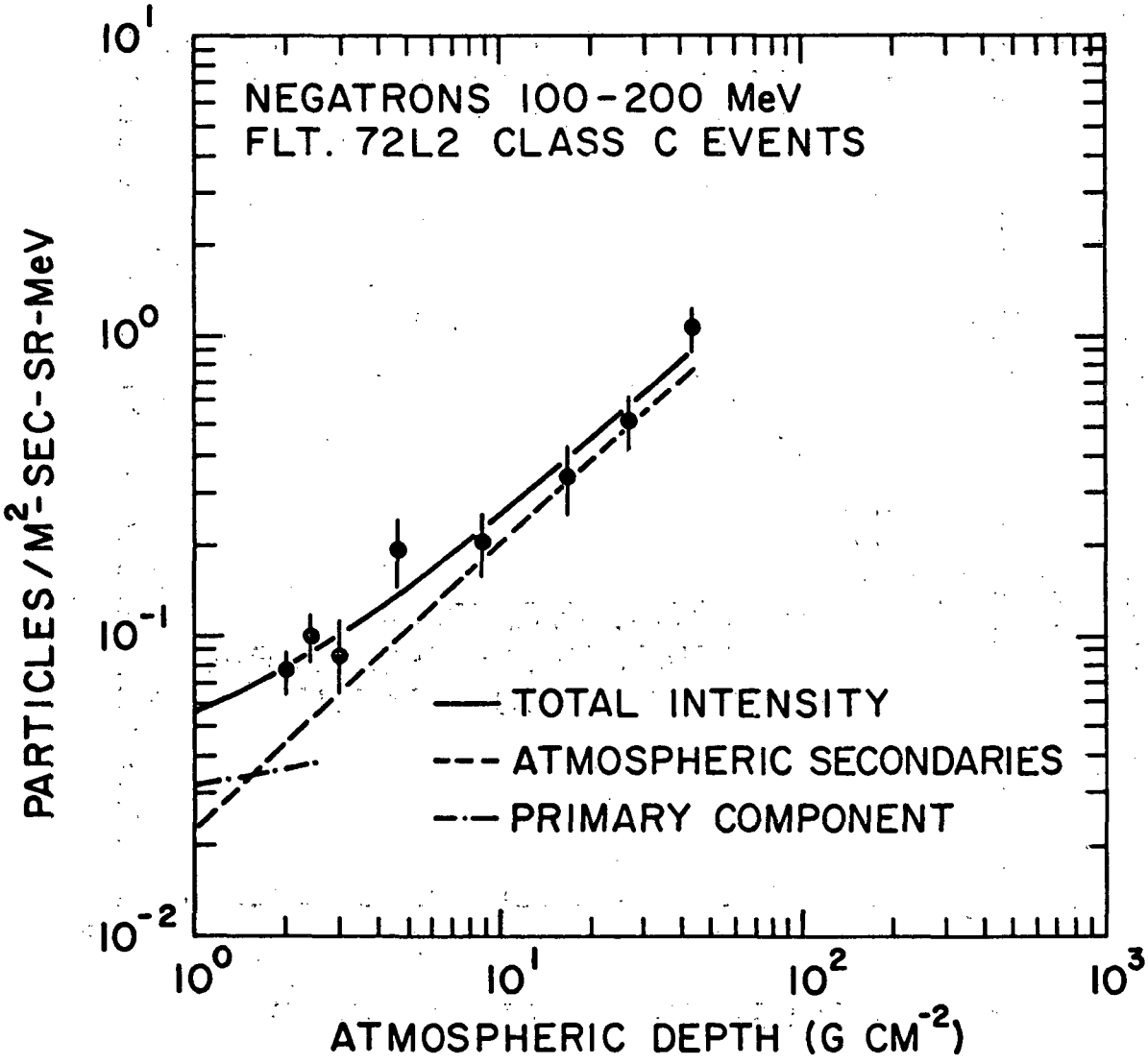

Figure 6.19 -- Atmospheric depth dependence of negatron intensity, 100-200 MeV (PHA-restricted events, see Table 6.4).

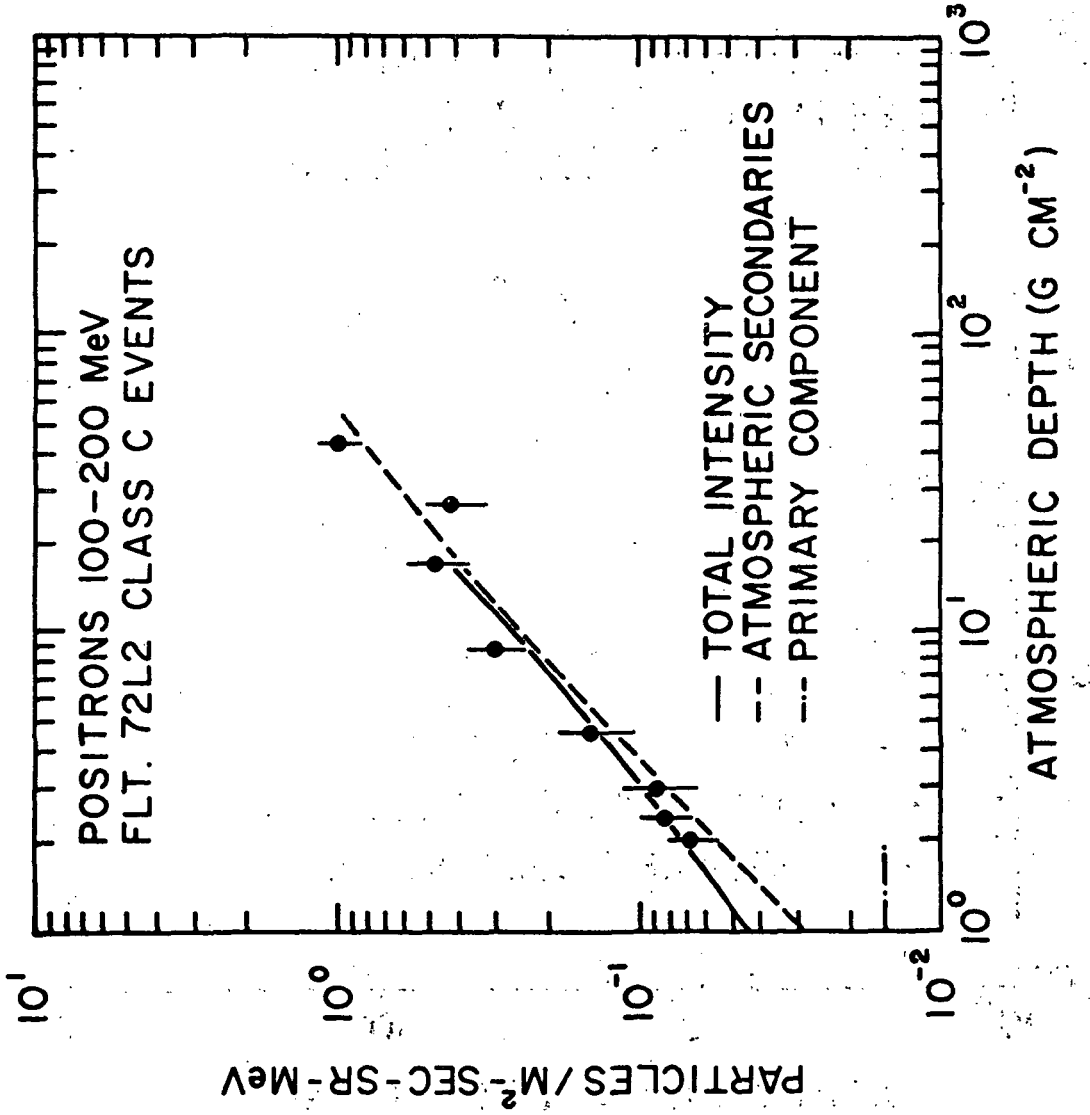

Figure 6.20 -- Atmospheric depth dependence of positron intensity, 100-200 MeV (PHA-restricted events, see Table 6.4).

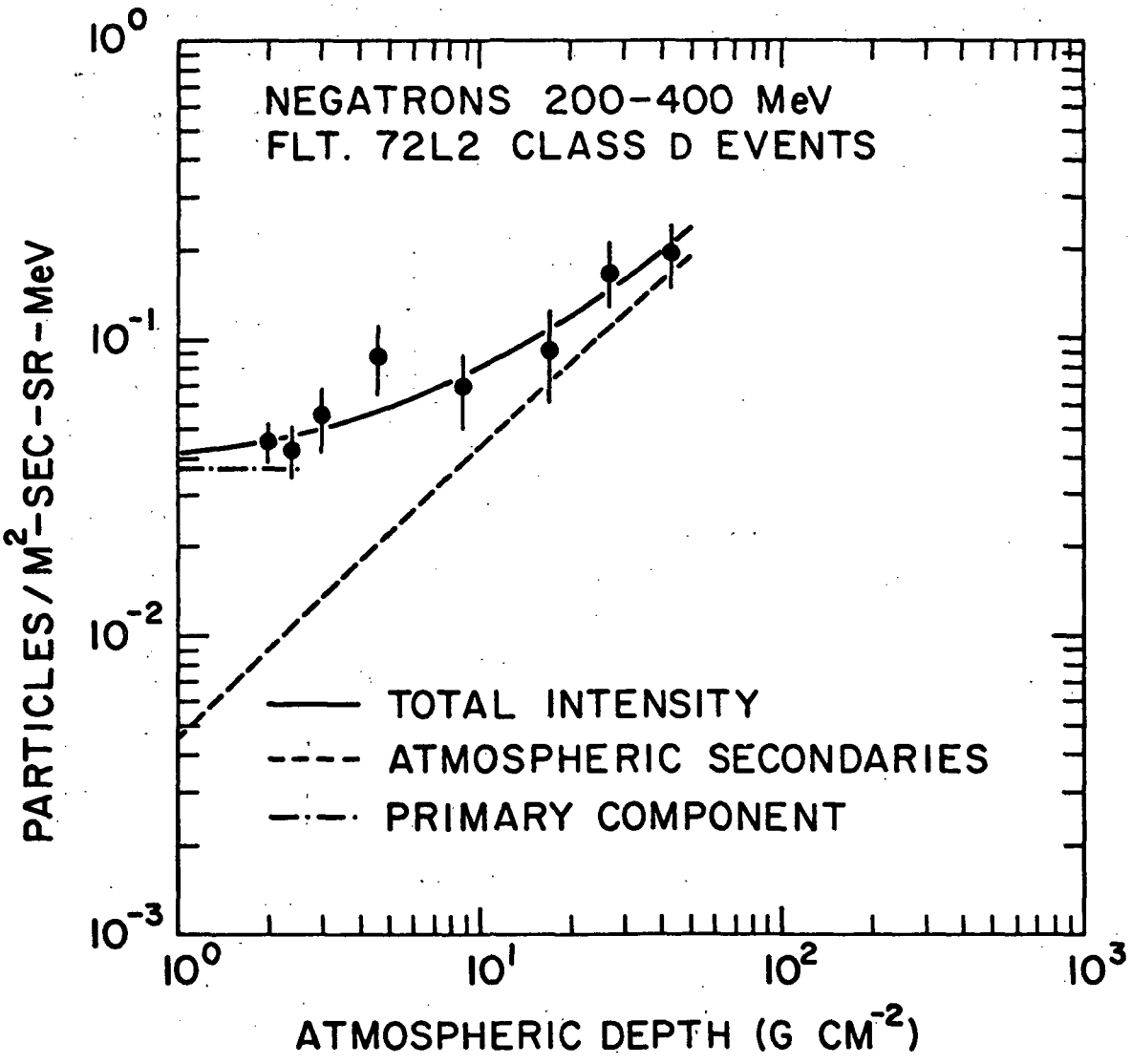

Figure 6.21 -- Atmospheric depth dependence of negatron intensity, 200-400 MeV (PHA-restricted events, see Table 6.4).

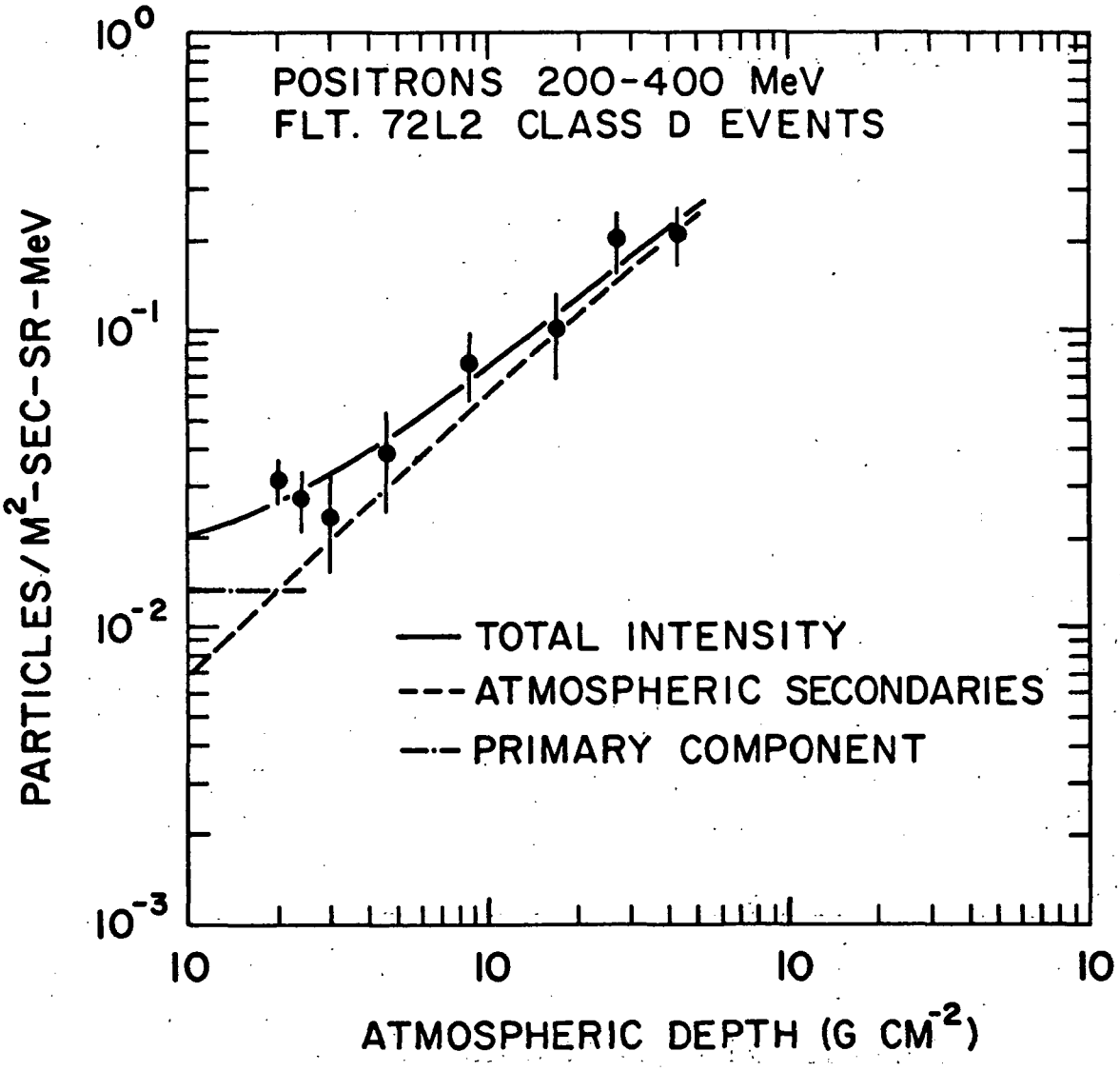

Figure 6.22 -- Atmospheric depth dependence of positron intensity, 200-400 MeV (PHA-restricted events, see Table 6.4).

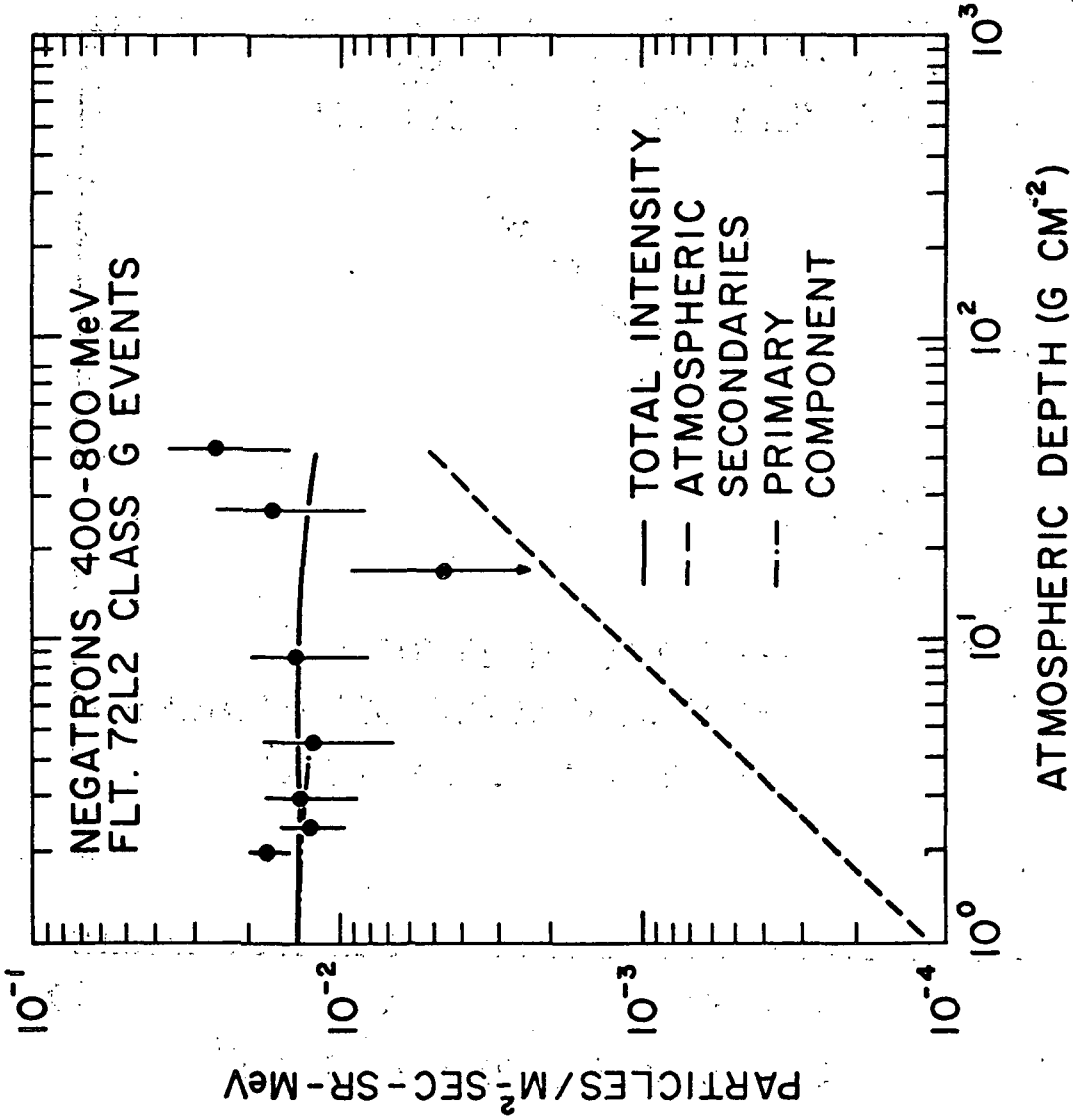

Figure 6.23 -- Atmospheric depth dependence of negatron intensity, 400-800 MeV (PHA-restricted events, see Table 6.4).

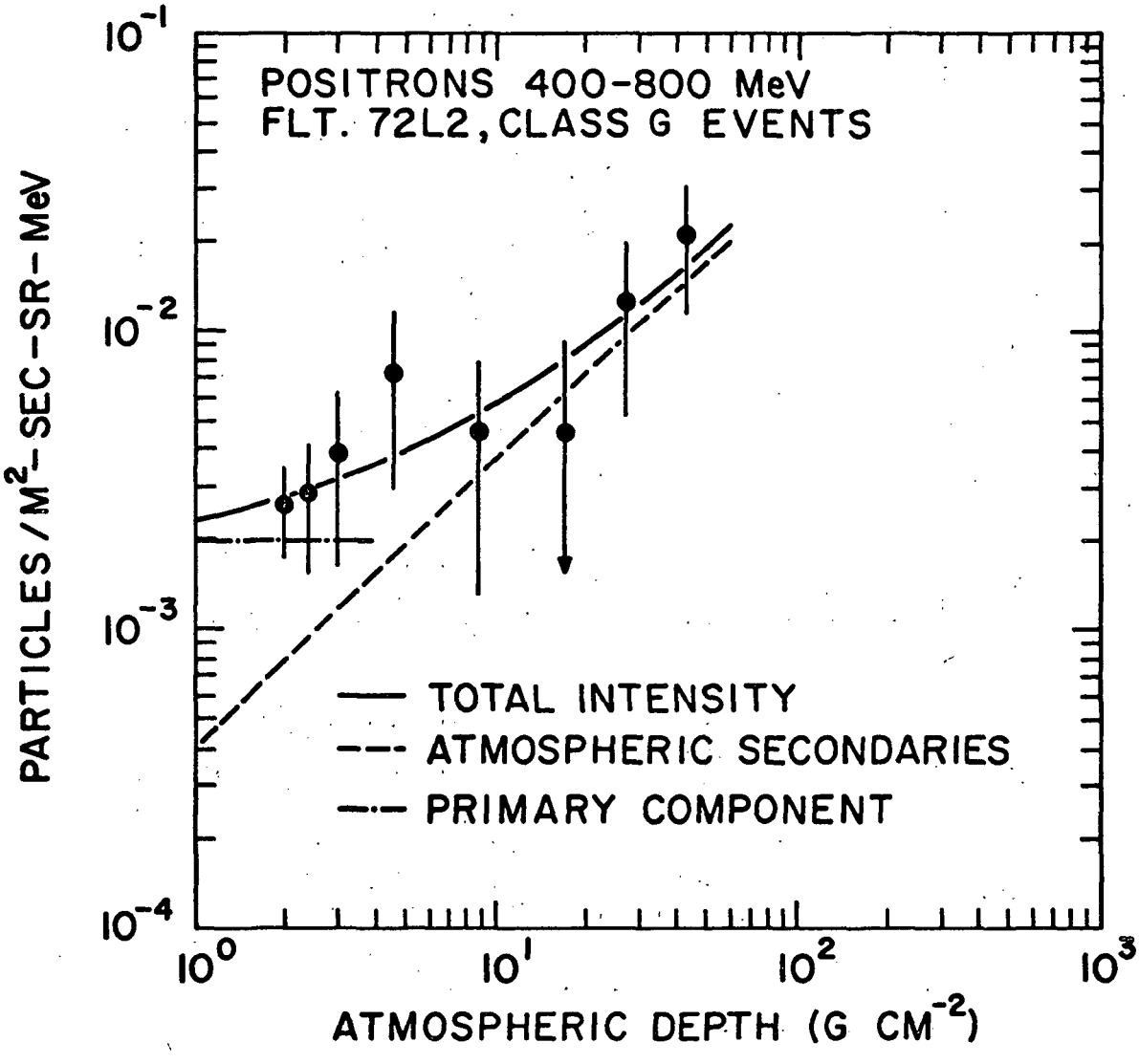

Figure 6.24 -- Atmospheric depth dependence of positron intensity, 400-800 MeV (PHA-restricted events, see Table 6.4).

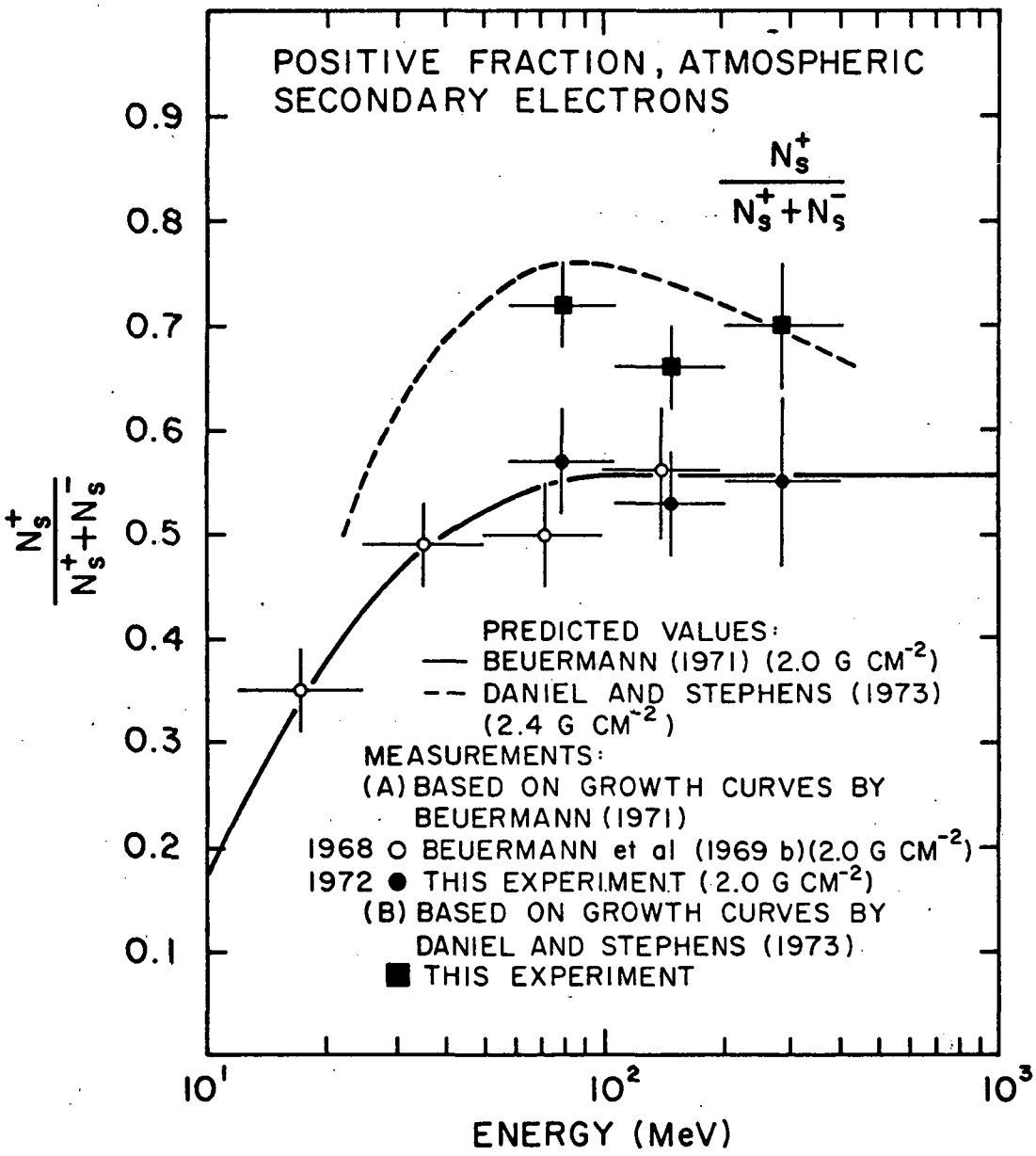

Figure 6.25 -- Positive fraction in atmospheric secondary electrons near 2 g cm^{-2} residual depth.

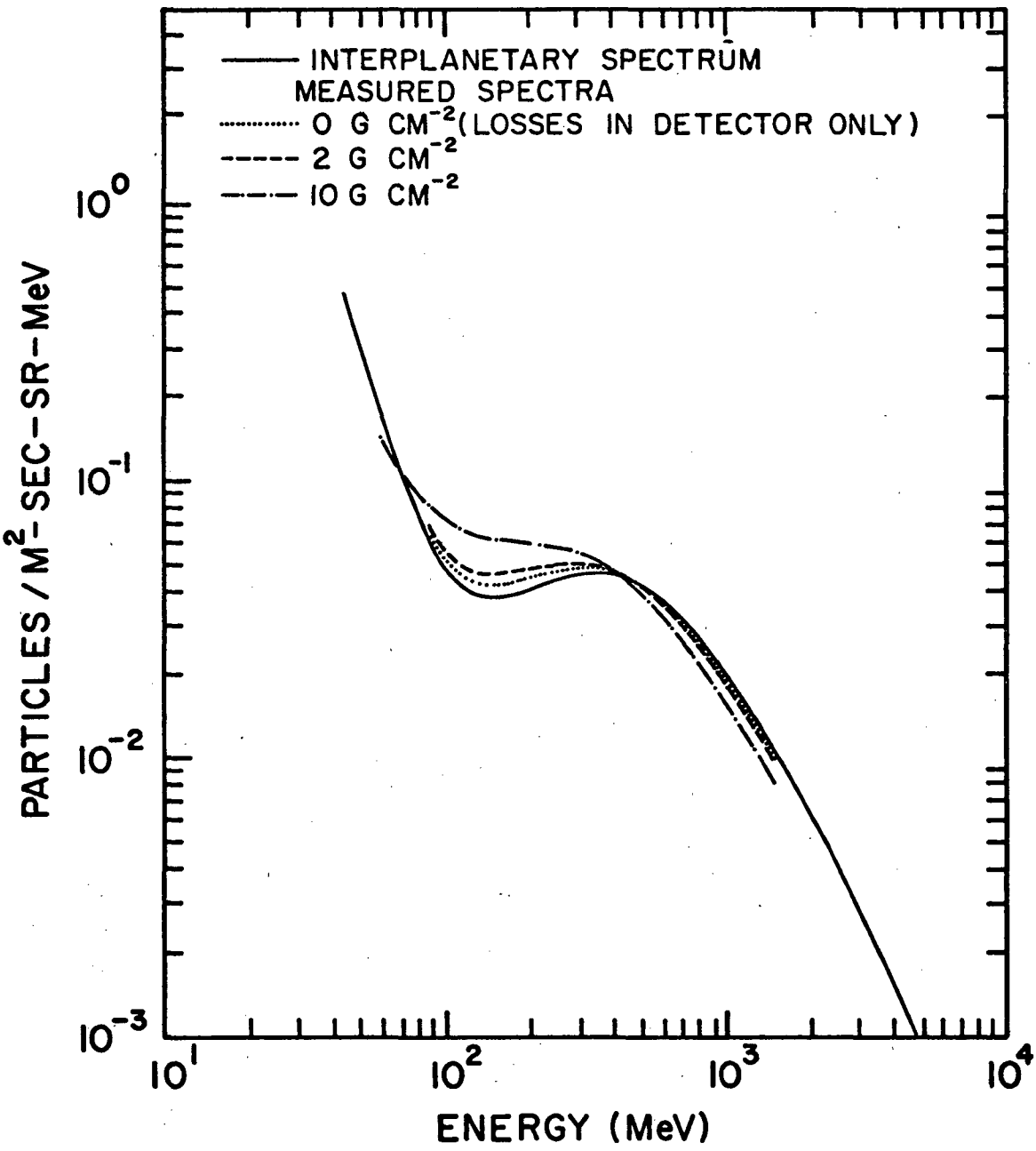

Figure 6.26 -- Distortion of interplanetary negatron spectrum by bremsstrahlung losses in the overlying atmosphere.

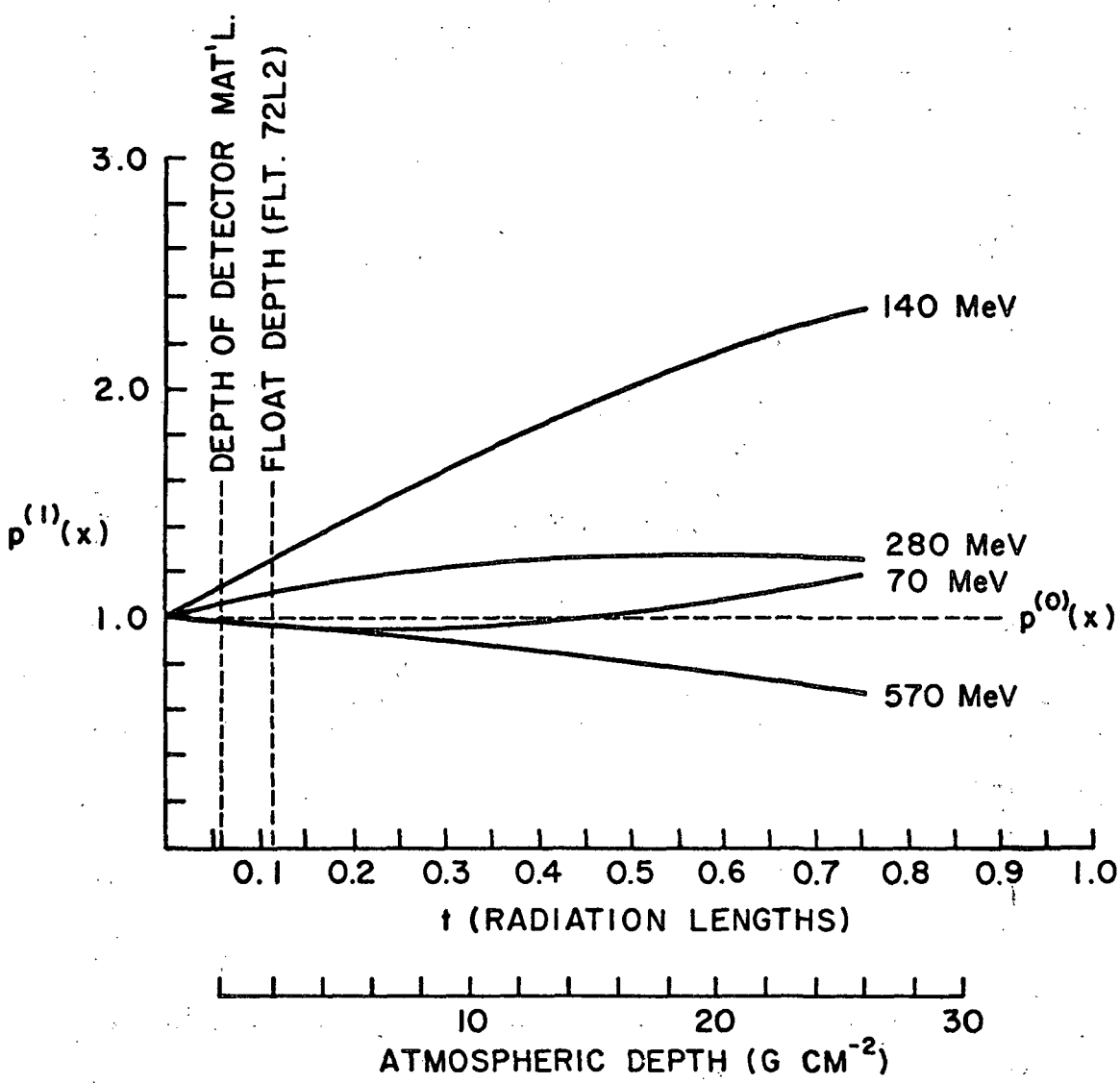

Figure 6.27 -- Depth dependence of primary negatron intensity at several energies (derived from Figure 6.26).

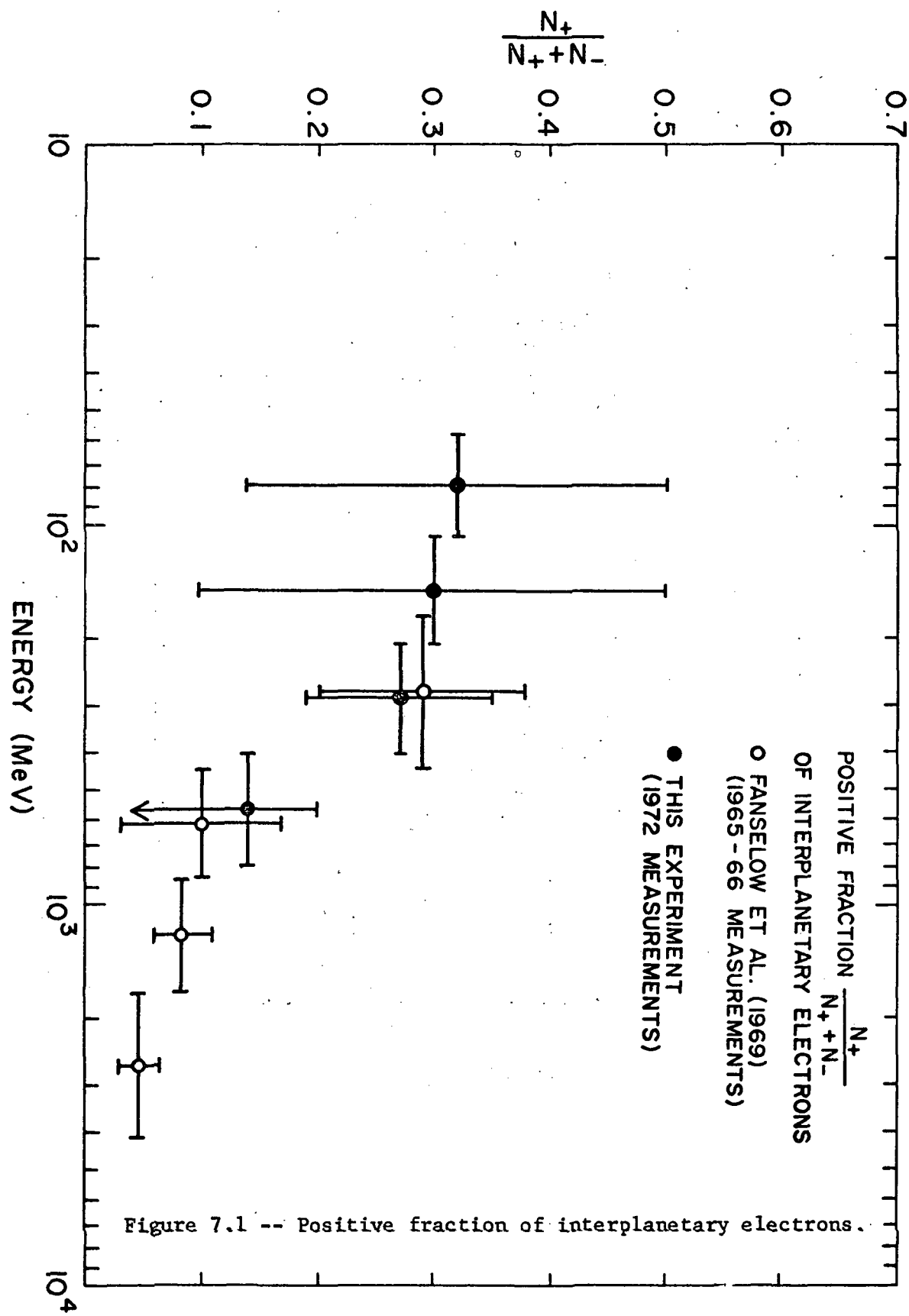

Figure 7.1 -- Positive fraction of interplanetary electrons.

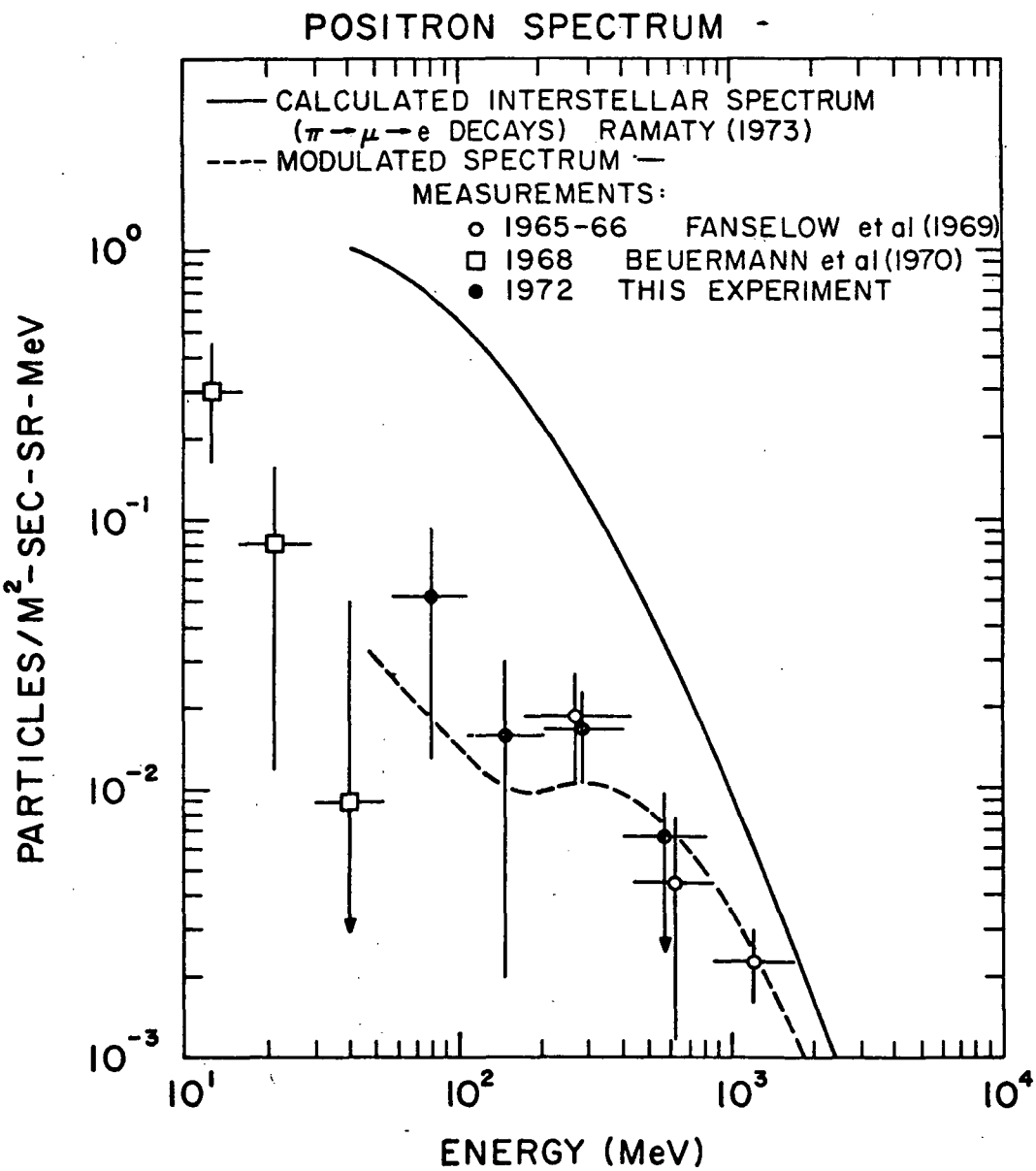

Figure 7.2 -- Positron spectrum.

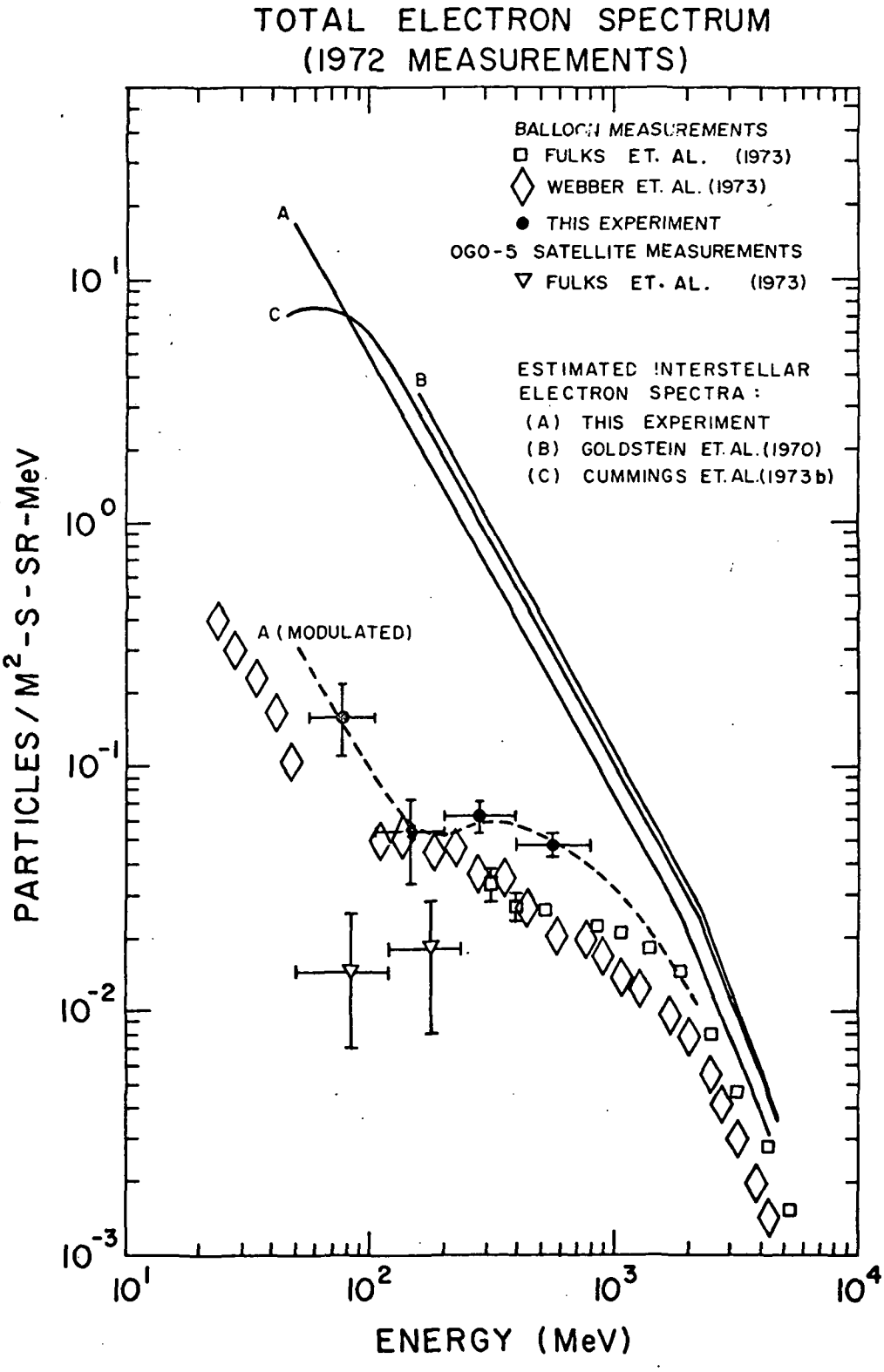

Figure 7.3 -- Total electron spectrum (1972 measurements).